UNIVERSITÀ DEGLI STUDI DI NAPOLI
FEDERICO II

DI
C
Ma
PI

Dipartimento
di Ingegneria Chimica,
dei Materiali e della
Produzione Industriale
Università degli Studi
di Napoli Federico II

Università degli Studi di Napoli Federico II

Scuola Politecnica e delle Scienze di Base

Dipartimento di Ingegneria Chimica, dei Materiali e della Produzione Industriale

Ph.D. Program in
Engineering of Industrial Products and Processes
XXXVI Cycle

Thesis for the Degree of Doctor of Philosophy

Characterization and Control of Interfacial Phenomena: Interface behavior of miscible systems and thin films in presence of complex flow conditions

by

Luigi Davide Gala

Advisor: Prof. Pier Luca Maffettone

Co-advisor: Prof. Daniele Tammaro

Co-advisor: Prof. Gerry G. Fuller

Ma nove per nove farà ottantuno?.

Massimo Troisi - Non ci resta che piangere

Characterization and Control of Interfacial Phenomena: Interface behavior of miscible systems and thin films in presence of complex flow conditions

Ph.D. Thesis presented
for the fulfillment of the Degree of Doctor of Philosophy
in Engineering of Industrial Products and Processes
by

Luigi Davide Gala

March 2024

Approved as to style and content by

Prof. Pier Luca Maffettone, Advisor

Prof. Daniele Tammaro, Scientific Committee

Prof. Gerry G. Fuller, Scientific Committee

Università degli Studi di Napoli Federico II
Ph.D. Program in Engineering of Industrial Products and Processes
XXXVI cycle - Chairman: Prof. Andrea D'Anna

Candidate's declaration

I hereby declare that this thesis submitted to obtain the academic degree of Philosophiæ Doctor (Ph.D.) in Engineering of Industrial Products and Processesis my own unaided work, that I have not used other than the sources indicated, and that all direct and indirect sources are acknowledged as references.
Parts of this dissertation have been published in international journals and/or conference articles (see list of the author's publications at the end of the thesis).

Napoli, March 7, 2024

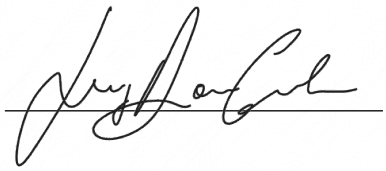

Luigi Davide Gala

Abstract

This dissertation delves into the intricate realm of interfacial phenomena, focusing on two distinct limit cases: miscible fluid dynamics and thin film drainage. Interfacial phenomena, occurring at the boundaries of different phases, present unique challenges due to the two-dimensional nature of interfaces, limiting sample sizes relative to bulk phases. The first part of the dissertation explores the ongoing debate on the existence of interfacial tension in miscible fluid systems, challenging traditional thermodynamic approaches. Miscible fluid interfaces, characterized by sharp gradients in concentration, temperature, density, or viscosity, hold significant importance in diverse fields such as geodynamics, polymer physics, and multiphase flow, with applications in oil recovery, hydrology, and filtration. The dissertation systematically investigates the interface behavior of a layered system comprising two miscible fluids subjected to sinusoidal rotational motion. A novel hydrodynamic instability, distinct from established phenomena, is identified, leading to the initiation of oscillatory Kelvin-Helmholtz instability and radial growth of fingers induced by centrifugal forces. This unprecedented destabilization scenario offers insights into potential applications, including controlled drop formation. In the context of thin film drainage, the second part of the dissertation emphasizes its crucial role in scientific and industrial processes. Thin film drainage influences coating, printing, stability of colloidal systems, lubrication, and various applications in nanotechnology and materials engineering. The study focuses on the interplay between thin film drainage and particle adsorption at the liquid/air interface. An unexplored consequence of particle adsorption is revealed, leading to a transition from immobility to mobility of the interface and an elevation in drainage velocity. This transition is attributed to the formation of a viscoelastic layer due to particle presence. The dissertation contributes to the understanding of interfacial phenomena in miscible fluid systems and thin film dynamics, addressing challenges and providing insights into potential applications. By manipulating parameters in the miscible fluid dynamics scenario, such as motion, viscosity ratio, diffusion, and interfacial tension, the dissertation demonstrates the tunability of finger characteristics. Additionally, in the thin film drainage context, the study identifies a novel effect of particle adsorption on interface mobility, opening avenues for further exploration in areas like protective coatings, biomedical applications, and nanotechnology. Overall, this dissertation highlights the significance of interfacial features across various length scales and their pivotal influence on diverse scientific and industrial phenomena.

Keywords: miscible interface, hydrodynamic instability, fluid fingers, thin film drainage, viscoelastic interface, interfacial mechanics.

Sintesi in lingua italiana

Questa tesi approfondisce l'intricato campo dei fenomeni interfacciali, concentrandosi su due distinti casi limite: la dinamica dei fluidi miscibili e il drenaggio di film sottili. I fenomeni interfacciali, che si verificano ai confini di diverse fasi, presentano sfide sperimentali a causa della natura bidimensionale delle interfacce, limitando le dimensioni del campione rispetto alle fasi bulk. La prima parte della tesi esplora il dibattito in corso sull'esistenza della tensione superficiale nei sistemi di fluidi miscibili. Le interfacce miscibili, caratterizzate da forti gradienti di concentrazione, temperatura, densità o viscosità, rivestono una notevole importanza in campi diversi come la geodinamica, la fisica dei polimeri e il flusso multifase, con applicazioni nella recupero del petrolio, nell'idrologia e nella filtrazione. La tesi indaga sistematicamente il comportamento dell'interfaccia di un sistema stratificato composto da due fluidi miscibili sottoposti a un movimento rotazionale sinusoidale. Viene identificata una nuova instabilità idrodinamica, diversa dai fenomeni consolidati, che porta all'innesco di un'instabilità oscillante di Kelvin-Helmholtz e alla crescita radiale di dita indotta dalla forza centrifuga. Questo scenario di destabilizzazione senza precedenti offre approfondimenti su possibili applicazioni, compresa la formazione controllata di gocce. Nel contesto del drenaggio di film sottili, la seconda parte della tesi enfatizza il ruolo cruciale in processi scientifici e industriali. Il drenaggio di film sottili influenza la verniciatura, la stampa, la stabilità dei sistemi colloidali, la lubrificazione e varie applicazioni in nanotecnologia e ingegneria dei materiali. Lo studio si concentra sull'interazione tra il drenaggio di film sottili formati da una bolla contro una parete orizzontale e l'adsorbimento di particelle all'interfaccia liquido/aria. Viene rivelata una conseguenza inesplorata dell'adsorbimento di particelle, che porta a una transizione da un comportamento immobile a mobile dell'interfaccia e a un aumento della velocità di drenaggio. Questa transizione è attribuita alla formazione di uno strato viscoelastico dovuto alla presenza di particelle. La tesi contribuisce alla comprensione dei fenomeni interfacciali nei sistemi di fluidi miscibili e nella dinamica dei film sottili, fornendo approfondimenti su possibili applicazioni. Manipolando i parametri nella dinamica dei fluidi miscibili, come movimento, rapporto di viscosità, diffusione e tensione superficiale, la tesi dimostra la regolabilità delle caratteristiche delle dita. Inoltre, nel contesto del drenaggio di film sottili, lo studio identifica un nuovo effetto dell'adsorbimento di particelle sulla mobilità dell'interfaccia, aprendo vie per ulteriori esplorazioni in settori come i rivestimenti protettivi, le applicazioni biomediche e la nanotecnologia. Nel complesso, questa tesi sottolinea l'importanza delle caratteristiche interfacciali su diverse scale di lunghezza e la loro influenza cruciale su diversi fenomeni scientifici e industriali.

Parole chiave: Interfacce miscibili, instabilità idrodinamiche, dita fluide, drenaggio di film sottili, interfacce viscoelastiche, meccanica interfacciale.

Contents

Acknowledgements

Stanford University and Prof. Gerry Fuller are acknowledged for hosting me during my research period abroad.

List of Figures

List of Tables

Introduction

Interfacial phenomena occur at the contact region of two distinct phases, such as a solid meeting a liquid or a liquid meeting a gas. The boundary, or interface, between these phases, exhibits markedly different properties compared to the bulk phase. The spectrum of challenges within the realm of interfacial phenomena is vast, encompassing wetting, spreading, foaming, flow through porous media, lung mechanics, cell membrane structure, adhesion, lubrication, bubble and drop mechanics, surface rheology, and more, spanning various application fields. The complexity of studying interfacial phenomena experimentally arises from the two-dimensional nature of the interface, limiting the sample size relative to the bulk.

This dissertation explores the importance of interfacial phenomena in two distinct limit cases. The first case involves thin films, where well-established interfacial features are known to predominate, and the second case, miscible systems, where the significance of interface behavior is still a subject of debate.

The existence of interfacial tension in miscible systems remains a highly debated topic. Traditionally, physicists classified fluids as miscible or immiscible, with no consideration of interfacial stresses in miscible systems within a thermodynamic approach. Interfacial tension, an intriguing phenomenon arising from molecular forces within liquids, is closely tied to compositional changes at interfaces and the resulting stress anisotropy near a liquid's boundary. In the context of immiscible fluids, the concept is well-established, where work must be done to bring a molecule from one liquid's bulk to the interface. Interfacial tension influences diverse phenomena, from supporting the weight of small objects on liquid surfaces to determining the spherical shape of liquid drops. It plays a crucial role in understanding hydrology, microbiology, petroleum hydrogeology, hemodynamics, and multiphase transport through porous media. Traditional scientific assumptions about immiscible fluids, such as equilibrium, mutual saturation, infinite boundary lifetime, and no net interdiffusion, have provided a self-consistent framework. The historical context reveals that van der Waals recognized the unphysical nature of an infinitely sharp interface, proposing a description suitable for both immiscible and miscible fluids. Theoretical studies on interfacial tension between miscible fluids date back to 1901, with D. Korteweg suggesting that stresses caused by density gradients could act as an effective interfacial tension.

However, the extension of these ideas to miscible fluids is currently under lively debate. Systematic experimental investigations in recent years have employed various strategies, from probing capillary waves to studying hydrodynamic instabilities. The relevance of interfacial tension in miscible systems has implications in fields ranging from geodynamics to polymer physics and multiphase flow, with practical applications in oil recovery, hydrology, and filtration. Understanding the sources of instability in miscible systems is crucial for designing fluids for extracting substances from porous media or piping systems. This knowledge is applicable in diverse scenarios, including soil decontamination, cleaning liquids for fabric, and processes analogous to oil extraction. At a fundamental level, effective surface tension plays a role in processes across different length scales, from chromatography column dynamics to geological phenomena. The transient nature of the surface tension between miscible phases becomes a necessary consideration in numerical simulations of miscible fluids, especially when modeling Kelvin-Helmholtz instabilities or Hele-Shaw flows.

The concept of instability is fundamental to the understanding of several physical phenomena. Generally, a system is unstable whenever a reaction to an external perturbation definitely modifies its structure through energy transfer. Hydrodynamic instabilities hold a special significance in fluid mechanics, playing a crucial role in comprehending various natural phenomena and serving diverse practical purposes. The stability of the boundary between miscible or immiscible fluids, when subjected to random disturbances, influences phenomena such as the dendritic shapes of snowflakes, premature failure in zinc alkaline batteries, breath sounds resulting from surfactant deficiencies in lungs, and the protection of the stomach from its acidic environment. The formation of morphological patterns and periodic structures often arises from interfacial instabilities. These instabilities can have positive impacts, as seen in chromatographic separation where viscous fingering enhances mixing in non-turbulent systems and small-scale devices. Conversely, they can be detrimental in applications like oil recovery and pipe cleaning, where maintaining stable interfaces between cleaning and waste fluids is crucial for optimizing removal efficiency. Consequently, the ability to control interfacial instabilities becomes essential in various technological applications, depending on whether a stable or unstable interface is desired. The issue of stability in miscible two-fluid systems holds significant importance due to the widespread occurrence of miscible interfaces in both natural and industrial settings. Boundaries delineated by sharp gradients in concentration, temperature, density, or viscosity characterize the interfaces between miscible fluids. Examples include ocean currents, silicate fluids in the Earth's mantle, and the spontaneous formation of a cell-free layer in blood microcirculation. In turbulent flows with high Reynolds numbers, effective mixing is facilitated by the chaotic nature of the velocity field and the energy cascade that spans a broad range of length scales. In contrast, at low Reynolds numbers, where inertial effects are negligible and turbulence is absent, hydrodynamic instabilities play a crucial role in enhancing mixing. This underscores the significance of comprehending stability in miscible fluids.

This dissertation delves into a fundamental exploration within the intricate realm of miscible

fluid dynamics. The primary objective is to assess the interface behavior of a layered system comprising two miscible fluids subjected to sinusoidal rotational motion. A novel hydrodynamic instability is identified, distinct from established phenomena in literature. Perturbing the interface leads to the initiation of wave patterns as shear stresses act on it, triggering an oscillatory Kelvin-Helmholtz instability—a phenomenon documented in similar systems. As the waves attain a critical height, centrifugal forces come into play, inducing the radial growth of fingers. This destabilization scenario is unprecedented, differing significantly from finger onset patterns documented in existing literature. Notably, the fingers in this scenario are formed by the more viscous fluid, ruling out a Saffman-Taylor-like instability. This phenomenon further distinguishes itself from finger formation during spin-coating processes, where centrifugal forces act on drops formed at the contact line due to a loss of axisymmetry. This dissertation aims to provide a comprehensive understanding of the dynamics underlying the new hydrodynamic finger instability, spanning from its foundational principles to potential control mechanisms. By manipulating parameters such as the imposed motion, fluid viscosity ratio, diffusion, and interfacial tension, one can tune the number of fingers, their length, and thickness. Furthermore, at the conclusion of the destabilization process, the formation of small drops at the tips of the fingers suggests potential applications in devices requiring controlled drop formation.

In the context of miscible systems, the significance of interfacial phenomena remains a subject of ongoing debate. This dissertation seeks to contribute new evidence supporting the importance of interfacial phenomena in this domain. On the other hand, it is widely acknowledged that these phenomena play a crucial role during thin films drainage.

Thin film drainage is a crucial phenomenon with significant applications in scientific and industrial domains. It plays a pivotal role in processes such as coating and printing, where it ensures uniform film thickness, contributing to high-quality product outcomes. In colloid and interface science, thin film drainage is vital for understanding the stability and interactions of dispersed particles, impacting the stability of colloidal systems like foams and emulsions. Moreover, thin film lubrication relies on the principles of thin film drainage to minimize friction and wear in mechanical systems. This knowledge is essential for designing effective lubricants. In devices like microelectromechanical systems and magnetic storage devices, as well as in biomedical applications like contact lenses, understanding and controlling thin film dynamics are crucial. Thin film drainage also influences the application of protective coatings on surfaces, affecting corrosion protection and durability. In nanotechnology and materials engineering, precise control over thin film drainage is necessary for the fabrication of materials and devices at the nanoscale, influencing their properties and performance. Extensive research has been conducted on fluid flow in thin films, beginning with the establishment of lubrication theory. In contemporary times, techniques like interferometry enable the direct measurement of thin film thickness and its spatio-temporal evolution.

This dissertation seeks to investigate the intricate interplay between the drainage process of a thin film between a bubble and a surface and the adsorption of particles at the interface of the bubble. The main objective is to evaluate the behavior of the liquid/air interface. A notably impactful consequence of particle adsorption, not previously documented in existing literature, has been recognized. In the presence of particles, the interface undergoes a transition from immobility to mobility, leading to an elevation in drainage velocity. This transition is correlated with the formation of a viscoelastic layer at the interface due to particle presence.

Interfacial features, irrespective of the characteristic length scale inherent to the system under investigation, are asserted to exert a pivotal influence across a diverse spectrum of phenomena.

State of Art

Fluids, in the realm of classical physics, have been traditionally categorized as either miscible or immiscible, with clear distinctions in their behavior and properties. Miscible fluids are typically described as those that, at thermodynamic equilibrium, blend together to form a uniform and homogeneous mixture, leaving no discernible interface. In contrast, immiscible fluids are known to exhibit well-defined interfaces due to their inability to fully mix at the molecular level. However, a realm of complexity exists beyond these conventional classifications, arising when miscible fluids, although expected to homogenize over time, temporarily exhibit distinct interfaces that defy traditional categorization. Surprisingly, miscible transient interfaces can be quantitatively characterized using theoretical frameworks introduced more than a century ago to describe the behavior of immiscible fluids. One of the pioneers in this field, Van der Waals, recognized that an infinitely sharp interface is unrealistic. Instead, a continuous region of transition in concentration, occurring over a molecular-scale thickness, was proposed as the appropriate description of the interface between immiscible fluids. Remarkably, Van der Waals' concept is not limited to immiscible systems and can be extended to interfaces in miscible fluids, provided the temporary nature is considered. The existence of transient interfaces in miscible fluids has significant implications. They can lead to the emergence of what appears to be an interfacial tension, even in situations where the fluids are entirely miscible. It is dynamic and decays over time as the liquids mix. The tension in miscible systems can be calculated by considering the unbalanced tangential stresses over the interface thickness, assuming temporal and local equilibrium. The concept was first introduced by Korteweg, who attributed these tensions to concentration inhomogeneities. The Cahn-Hilliard-Navier-Stokes equations provide a theoretical framework to model miscible interfaces, treating them as diffuse interfaces with dynamic surface tension.

The fascinating world of hydrodynamic instabilities in miscible fluids, with a focus on the unique consequences arising from the existence of transient interfaces, will be reported. Parallels and distinctions will be drawn between miscible and immiscible interfaces, examining the theoretical challenges of fluid mixing and shedding light on the controversial stabilizing phenomena in such systems. The instabilities that will be reported are categorized into three distinct families: those arising when a less viscous fluid displaces a more viscous one, known as Saffman–Taylor in-

stabilities, those occurring in stratified configurations due to various factors like tangential motion, gravitational instability, density and viscosity stratification, or oscillatory forcing, which include Kelvin–Helmholtz, Rayleigh–Taylor, shear flow, Faraday, and Oscillatory Kelvin–Helmholtz instabilities, and those occurring when a spreading process is accelerated by an external force, as fingers formation. These instabilities hinge on the balance between mechanisms that amplify disturbances and those that tend to stabilize the interface. Notably, capillary forces often play a pivotal role in stabilizing these transient interfaces, challenging the common assumption of zero surface tension for miscible systems.

2.1 Immiscible Interface

2.1.1 Historical Perspective

In the early 1800s, many works by Young, Laplace, and Gauss attempted to explain the nature of the interface between two fluids. Their works led to a correct estimate of the intermolecular energy of liquids based on a mechanical or static view of the matter. Herein, a fluid-fluid interface was supposed to be a step function in the density, representing an interface of zero thickness.

Poisson (1831), Maxwell (1876), and Gibbs (1876) noticed that the interface actually shows a rapid but smooth transition of physical properties from one phase to another. Van der Waals, in his *"The Thermodynamic Theory of Capillarity under the Hypothesis of a Continuous Variation of Density"* [1], supposed density was a continuous function of spatial coordinates, using thermodynamic arguments, based on his equation of state. The main postulate defines a free-energy density (at fixed temperature) as a function of the local density ρ and of the density of neighboring points for both homogeneous and nonuniform systems. The local free energies differ for an extra term in nonuniform systems arising from energy, not entropy. Using this result, he showed how density changes smoothly, moving from one phase to the other, leading to stable free energy and predicting the thickness of the interface. He wrote:

"...has shown theoretically that it is very probable that the discontinuity at the surface of a liquid and its vapor is only apparent and that there is a layer of transition, very thin to be sure, but of a thickness much larger under ordinary conditions than the radius of the sphere of action of the molecules, and which can even grow indefinitely as one approaches the critical temperature."

The same arguments were proposed by Lord Rayleigh [2]. Later, in 1958, Cahn and Hilliard re-derived the same results in a more modern appearance [3].

2.1.2 The Thermodynamic Theory of Capillarity

Herein, Cahn and Hilliard's derivation of the general equation of the free energy of a 'nonuniform' system having a spatial variation of its intensive scalar properties [3], such as density or composition, is reported. They used this equation to determine the free energy of a flat interface between two phases.

Considering a binary solution formed by two components A and B, and c is the nonuniform property, the mole fraction of the B component, the local free energy per molecule, f, in a region of nonuniform composition, depends on the local composition and the composition of the close environment so that it can be expressed as the sum of local composition and local composition derivatives. Assuming a small composition gradient compared with the reciprocal of the intermolecular distance and taking c and its derivatives as independent variables, f is a continuous function of these variables, and it can be expanded in a Taylor series

$$f(c, \nabla c, \nabla^2 c, ...) = \\ f_0 + \sum_i L_i(\partial c/\partial x_i) + \sum_{ij} k_{ij}^{(1)}(\partial c/\partial x_i \partial x_j) + (1/2)\sum_{ij} k_{ij}^{(2)}[(\partial c/\partial x_i)(\partial c/\partial x_i)] + ... \quad (2.1)$$

where

$$\begin{aligned} L_i &= [\partial f/\partial(\partial x/\partial x_i)]_0 \\ k_{ij}^{(1)} &= [\partial f/\partial(\partial^2 c/\partial x_i \partial x_j]_0 \\ k_{ij}^{(2)} &= [\partial^2 f/\partial(\partial c/\partial x_i)\partial(\partial c/\partial x_j)]_0 \end{aligned} \quad (2.2)$$

For an isotropic medium, the free energy is invariant to the symmetry operations of reflection and rotation about a fourfold axis, so

$$\begin{aligned} L_i &= 0, \\ k_{ij}^{(1)} &= k_1 = [\partial f/\partial \nabla^2 c]_0 \text{ for } i = j \\ k_{ij}^{(1)} &= 0 \text{ for } i \neq j \\ k_{ij}^{(2)} &= k_2 = [\partial^2 f/(\partial\,|\nabla c|)^2]_0 \text{ for } i = j \\ k_{ij}^{(2)} &= 0 \text{ for } i \neq j \end{aligned} \quad (2.3)$$

Hence, the 2.1 becomes

$$f(c, \nabla c, \nabla^2 c, ...) = f_0(c) + k_1 \nabla c + k_2(\nabla c)^2 + ... \quad (2.4)$$

Integrating over the volume V, the total free energy F is

$$F = N_v \int_V f dV = N_v \int_V [f_0(c) + k_1 \nabla c + k_2(\nabla c)^2 + ...] dV \quad (2.5)$$

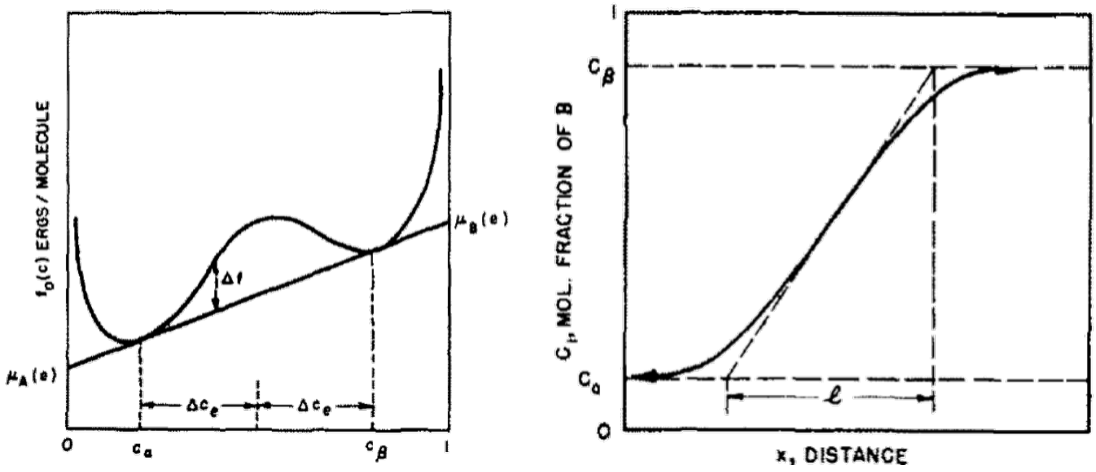

(a) (b)

Figure 2.1. Nonuniform systems functions. a) f_0 for $T < T_c$ **b)** Interface profile. Reproduced with permission from [3]. ©*AIP Publishing, 1958.*

where N_v is the number of molecules per unit volume. Applying the divergence theorem

$$\int_V (k_1 \nabla^2 c) dV = -\int_V (dk_1/dc)(\nabla c)^2 dV + \int_S (k_1 \nabla c \cdot n) dS \tag{2.6}$$

The chosen integration boundary in 2.5 makes $\nabla c \cdot n$ is zero and, replacing the 2.6 in 2.5

$$F = N_v \int_V [f_0 + k(\nabla c)^2 + ...] dV \tag{2.7}$$

where

$$k = -dk_1/dc + k_2 = -[\partial^2 f/\partial c \partial \nabla^2 c]_0 + [\partial^2 f/(\partial |\nabla c|)^2]_0 \tag{2.8}$$

The equation 2.7 defines the free energy of a small volume as the sum of free energy in homogeneous conditions and of a 'gradient energy' that is a function of local composition. It can be used to evaluate the free energy of a flat interface.

Considering a flat interface, whose area is A, between two isotropic phases α and β, whose compositions are c_α and c_β respectively, the free energy of the volume with composition intermediate between c_α and c_β is represented by $f_0(c)$, reported in Fig. 2.1a. For a one-dimensional composition change through the interface, the equation 2.7 becomes

$$F = AN_v \int_{-\infty}^{+\infty} [f_0(c) + k(dc/dx)^2] dx \tag{2.9}$$

and because of the interfacial free energy, σ, is the difference between the actual and homogeneous free energies

$$\sigma = N_v \int_{-\infty}^{+\infty} [f_0(c) + k(dc/dx)^2 - c\mu_b(e) - (1-c)\mu_a(e)] dx \tag{2.10}$$

where $\mu_a(e)$ and $\mu_b(e)$ are the chemical potentials that must be the same for each species in each phase (equilibrium condition). Rewriting the 2.10

$$\sigma = N_v \int_{-\infty}^{+\infty} [\nabla f(c) + k(dc/dx)^2] dx \tag{2.11}$$

where $\nabla f(c)$ is the free energy referred to a standard state of a mixture of α and β in equilibrium

$$\nabla f(c) = f_0(c) - [c\mu_b(e) - (1-c)\mu_a(e)] \tag{2.12}$$

the term $k(dc/dx)^2$ decreases the more diffuse the interface is. At equilibrium, the equation 2.11 is a minimum. Such a condition derives from the consistency of chemical potentials throughout the system. Replacing the integrated I of 2.11 in the Euler equation

$$I - (dc/dc)[\partial I/\partial(dc/dc)] = 0 \tag{2.13}$$

The condition for a stationary value is

$$\nabla f(c) + k(dc/dx)^2 = const = 0 \tag{2.14}$$

because both terms tend to zero as $x \to \pm\infty$, so

$$f(c) = k(dc/dx)^2 \tag{2.15}$$

replacing in the 2.11

$$\sigma = 2N_v \int_{-\infty}^{+\infty} \nabla f(c) dx \tag{2.16}$$

and changing the variable of integration from x to c

$$\sigma = 2N_v \int_{c_\alpha}^{c_\beta} [k\nabla f(c)]^{1/2} dc \tag{2.17}$$

In the special case of approaching the critical point, the surface region became large enough and the latter was used for determining the dependence of σ on temperature and, from 2.15, the relationship between the thickness of the interface and temperature was obtained.

Deriving the expression of ∇f when f_0 is expanded in a Taylor series about T_c and c_c, the critical temperature and concentration respectively, the following relationships are obtained

$$(\nabla c_c)_{(T\sim T_c)} = \beta(T_c - T)/2\gamma \tag{2.18}$$

$$(\nabla f)_{(T\sim T_c)} = \gamma[(\nabla c_c)^2 - (\nabla c)^2]^2 \tag{2.19}$$

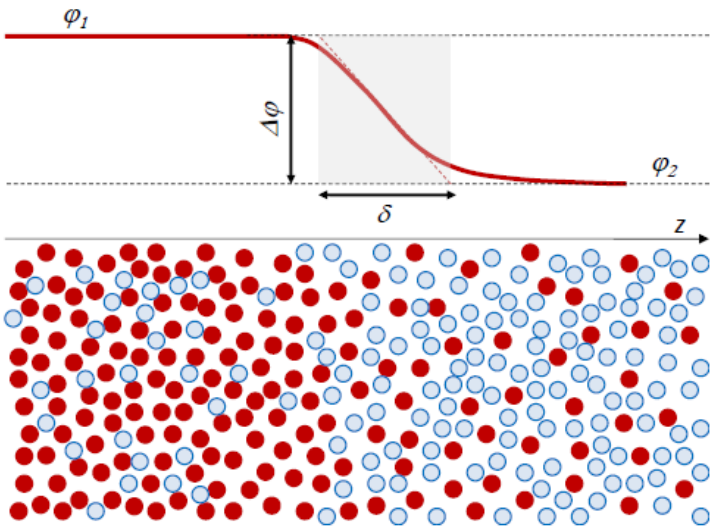

Figure 2.2. Interfacial transition. The volume fraction ϕ of fluid A (red particles) is a continuous spatial function. δ is the interface thickness. Reproduced with permission from [4]. ©*Royal Society of Chemistry. 2017.*

where $\nabla c = (c - c_c)$, $\nabla c_c = (c_\beta - c_c) = (c_c - c_\alpha)$, $\beta = (\partial^3 f_0/\partial T \partial c^2)/2!$ and $\gamma = (\partial^4 f_0/\partial c^4)/4!$ with the derivatives of f_0 evaluated at $c = c_c$ and $T = T_c$.

The composition variation throughout the interface (Eq. 2.15), is such that

$$dc/dx = (\nabla f/k)^{(1/2)} \tag{2.20}$$

To satisfy the latter, the composition profile must be the one reported in Fig. 2.1b. Integrating the 2.20 with 2.18 and 2.19, expressing the thickness l of the interface in terms of the gradient of c_c and being k constant

$$l = (c_\alpha - c_\beta)/(dc/dc)_{c_c} = 2\nabla c_c (k/\nabla f_{max})^{(1/2)} \tag{2.21}$$

thus, the interface thickness increases with increasing temperature and, approaching the critical temperature, it tends to infinity [1, 5].

The main property of the interface predicted by this treatment is that the interface between two phases is diffuse and its thickness depends on temperature, showing that an infinitely sharp interface is unphysical [4]. Here, the interface between two immiscible fluids is a continuous region in which there is a smooth transition in concentration over a thickness δ of molecular size (Fig. 2.2).

2.1.3 Surface Tension, Contact Angle and Young-Laplace Pressure

An imaginary plane known as the interface separates the atoms or molecules of two solid or liquid phases in contact, with particles present on both sides of this boundary. Surface tension is a

concept that emerges from the cohesive forces between the molecules of a substance. Considering a system as in Fig. 2.3a formed by two phases, liquid, and gas, in contact throughout an interface, these cohesive forces act on molecules in the bulk symmetrically, pulling them toward each other. Each molecule experiences on average, isotropic interactions, resulting in an equilibrium condition. However, ascending to the liquid's surface, molecules find themselves at an energy disadvantage. They face the other phase, devoid of neighboring molecules on one side, leading to an asymmetry of forces. Those at the surface experience an inward pull due to the attractive forces with their immediate neighbors. This imbalance of forces compels surface molecules to act as if they are being drawn into the liquid, creating a resilient and continuous film at the liquid's interface, the foundation of what we know as surface tension [6]. The same concept is also valid for a fluid-fluid interface (interfacial tension).

The following are the mechanical and thermodynamic definitions of surface tension, the definition of contact angle and the derivation of the general form of the Young-Laplace equation, which gives the pressure difference between two fluid phases, as described in [6, 7, 8, 9].

To increase the surface area of a liquid by a small amount, dA, work is required to overcome the cohesive forces holding the liquid molecules together. This work is proportional to the number of molecules that must be brought up to the surface to create this increase in surface area. The relationship between the work done dW and the change in surface area dA , can be expressed as:

$$dW = \gamma dA \tag{2.22}$$

This equation shows the surface tension γ as the required energy for increasing the surface area by unit amount. The greater the surface tension of the liquid, the more work is needed to increase its surface area. Surface tension can also be defined as a force for unit length. The apparatus, reported in Fig. 2.3b, is a frame formed by the three fixed glass sides and one, with length l, that can roll on the two parallel sides of the rectangle. If a soap film is stretched over such a frame, the mobile rod moves spontaneously in the direction of the arrow(Fig.2.3b) to decrease the surface

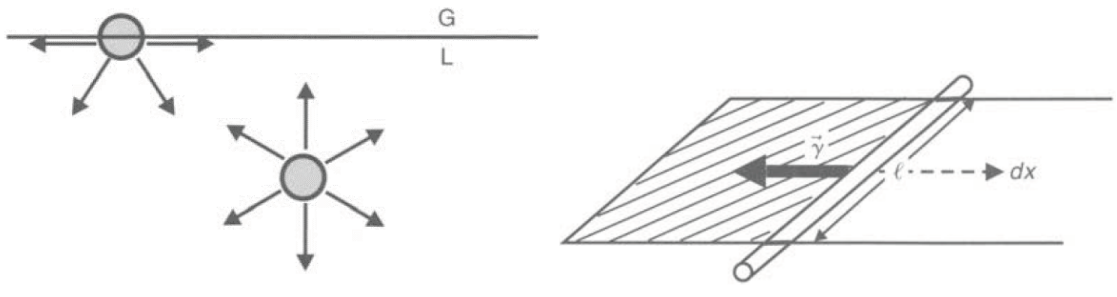

(a) (b)

Figure 2.3. Interfaces physical origin and effects. a) An illustration of the attractive force acting on a molecule in fluid bulk and at the interface. **b)** Effect of capillary force when a movable rod is held by a thin film. Reproduced with permission from [6]. ©*Springer, 2004.*

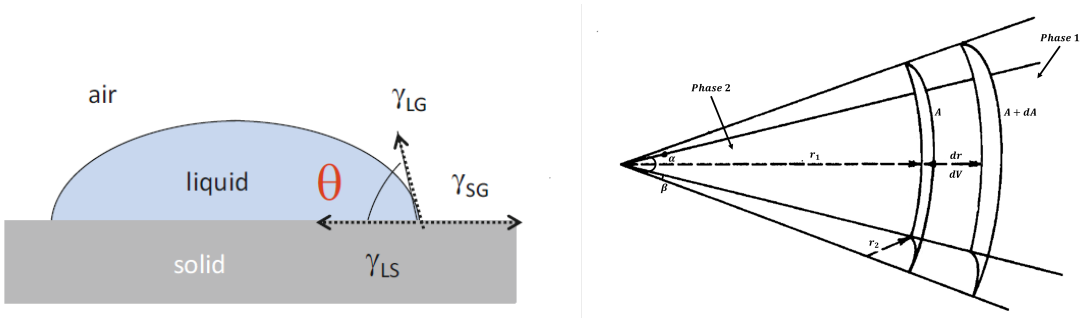

(a) (b)

Figure 2.4. General interface sketch and sessile drop. a) Liquid drop on a substrate. γ_{ij} is the interfacial tension between the phases i and j and θ is the contact angle. Reproduced with permission from [8]. ©Springer, 2021. **b)** Sketch of an interface with two radii of curvature. Reproduced with permission from [9]. © *Wiley, 1997.*

area of the liquid. If dx is the distance traveled by the mobile rod, the work done

$$\partial W = Fdx = 2\gamma l dx \tag{2.23}$$

demonstrates that the surface tension is also a force exerted per unit length.

Using thermodynamics, from the Eq. 2.22, the variation of total free energy F during surface area increasing is

$$dF = \gamma dA - PdV - SdT \tag{2.24}$$

where P, V, and S are the pressure, the volume, and the entropy, respectively. At constant temperature, the surface tension

$$\gamma = \left(\frac{\partial F}{\partial A}\right)_{T,V} \tag{2.25}$$

At equilibrium, systems minimize surface area; thus, the surface of liquids in containers appears flat, while single bubbles or drops typically assume a spherical shape.

The equation 2.25 is not useful when one of the phases is a solid, that is submitted to a mechanical strain, whose stresses must be included in the free energy variation. In this case, the concept of equilibrium contact angle is introduced. Considering a sessile drop, as reported in Fig. 2.4a, the three phases, gas, liquid, and solid, are in contact at the so-called "three-phase contact line". The contact angle is defined as the angle with which the liquid and gas phases hit the solid and the equilibrium balance of interfacial energy at the surface between liquid and gas

$$\gamma_{SG} = \gamma_{LS} + \gamma_{LG} cos(\theta) \tag{2.26}$$

where γ_{SG}, γ_{LS}, and γ_{LG} are the interfacial tension between solid-gas,liquid-solid, and liquid-gas phases, respectively, leads to the definition of contact angle. The Young equation can be derived through consideration of Gibbs free energy [10]. When a liquid droplet forms a meniscus and

attains equilibrium, the change in Gibbs free energy is zero, and neglecting the gravitational force

$$dG = \gamma_{LG}\ dA_{LG} + \gamma_{SG}\ dA_{SG} + \gamma_{LS}\ dA_{LS} = 0 \tag{2.27}$$

where dA represents small variations in surface area. The changes in the interfacial area are

$$dA_{LS} = -dA_{SG} \tag{2.28}$$

and

$$dA_{LG} = cos\ \theta\ dA_{LS} + \gamma_{LG}(cos\ \theta\ dA_{LG} + \gamma_{SG}(-dA_{SG}) + \gamma_{LS}\ dA_{LS} = 0 \tag{2.29}$$

taking into account that any increase in the solid-liquid interface is compensated by a reduction in the solid-gas interface. By substituting the Eqs. 2.28 and 2.29 into Eq. 2.27, The Young equation is derived.

The last argument for characterizing an interface is the pressure difference between two fluid phases, called "Capillary Pressure". Considering the system reported in Fig. 2.4b and defining the capillary pressure as

$$P_c = P_2 - P_1 \tag{2.30}$$

the work done by phase 2 on phase 1 for increasing its volume by dV and interface area by dA, is

$$dW = P_2 dV - P_1 dV = (P_2 - P_1)dV = P_c dV = \sigma dA \tag{2.31}$$

so the capillary pressure is

$$P_c = \sigma \frac{dA}{dV} \tag{2.32}$$

Evaluating dA and dV, with the hypothesis that the increase of radius dr is small

$$dA = \alpha\beta(r_1 + r_2)dr \tag{2.33}$$

and

$$dV = \alpha\beta r_1 r_2 dr \tag{2.34}$$

where r_1 and r_2 are the two radii of curvature, and substituting Eq. 2.33 and 2.34 in 2.32

$$P_c = \gamma \left(\frac{1}{r_1} + \frac{1}{r_2} \right) = \gamma(\kappa_1 + \kappa_2) \tag{2.35}$$

where κ_1 and κ_2 are the curvature in the two directions taken into account. The Eq. 2.35 links the increase in pressure across an interface to the product of surface tension and local curvature of the interface. The latter, considering a drop or a bubble, in which the two radii of curvature are

the same ($r_1 = r_2 = r$), becomes the well-known "Laplace Pressure"

$$P_c = \frac{2\gamma}{r}. \tag{2.36}$$

2.1.4 Hydrodynamic Instabilities

Hydrodynamic instabilities refer to disturbances or perturbations in the motion of fluids that can lead to the development of complex flow patterns, turbulence, and irregular behavior. These instabilities arise due to the interplay of various forces and interactions within a fluid, and they can occur in both liquids and gases. In this literature review, the discussion centers on three key phenomena: the Saffman-Taylor instability, the formation of fingers during an accelerated spreading process (as in the spin coating process), and the Kelvin-Helmholtz instability, particularly its alteration under oscillatory forcing conditions, commonly referred to as "frozen waves" or the Oscillatory Kelvin-Helmholtz instability. This comprehensive exploration provides a solid foundation for comprehending the recently uncovered fingers instability in this research work.

The Kelvin-Helmholtz Instability (KHI) is a hydrodynamic instability observed when immiscible, incompressible, and inviscid fluids are in relative, irrotational motion. The uniform velocity and density profiles exist within each fluid layer, but they experience discontinuity at the plane interface between the two fluids. This discontinuity in tangential velocity, representing shear flow, generates vorticity at the interface. Consequently, the interface transforms into an unstable vortex sheet, rolling up into a spiral pattern [12, 13]. The fundamental mechanism behind Kelvin-Helmholtz Instability development relies on the presence of uniform velocity shear, without the need for gravitational or density differences. In most cases, theoretical and numerical calculations simplify by neglecting gravity, density variations, surface tension, and viscosity. In this treatment, KHI is considered a fluid instability where a lighter fluid overlays a heavier one [14]. When the situation is reversed, with a heavier fluid over a lighter one, the instability is known as Rayleigh-Taylor Instability (RTI) [14]. Another inviscid fluid instability involving density stratification is Richtmyer-Meshkov Instability (RMI), which is a shock-induced interfacial instability [15, 16]. KHI, RTI, and RMI exhibit distinct linear growth rates (exponential for KHI and RTI, proportional to time for RMI), allowing differentiation at the linear stage. However, in the fully nonlinear stage, when complex interfacial motion with roll-up occurs, these instabilities are often

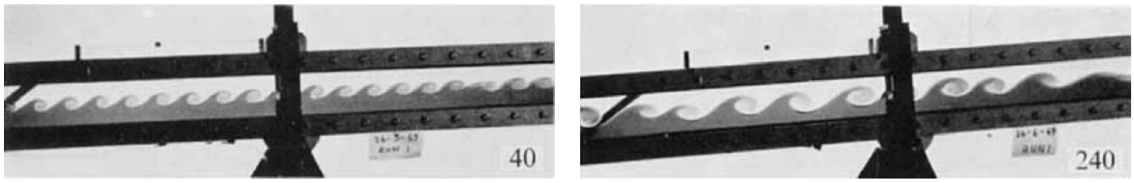

Figure 2.5. Classical Kelvin-Helmholtz Instability. It is a fluid instability that occurs when there is a velocity difference across the interface between two fluids. Reproduced with permission from [11]. *Open Access, CC License.*

indistinguishable and commonly discussed collectively as KHI.

The classical Kelvin-Helmholtz instability, induced by a steady shear, generates waves that exhibit a curling and rolling-up behavior, as illustrated in Fig. 2.5. These waves often evolve into a series of vortices or cat-eye structures and can rapidly transition to turbulence due to flow's highly nonlinear nature [11]. Considering two inviscid fluids layers, differing in densities ρ_1 and ρ_2, moving with uniform speeds U_1 and U_2. The interfacial tension and gravity act as stabilizing forces, while inertia is a destabilizing force. A linear stability analysis reported a critical velocity depending on fluid densities

$$(U_1 - U_2)^2 = \frac{2(\rho_1 + \rho_2}{\rho_1 \rho_2} \sqrt{\sigma g(\rho_1 - rho_2} \tag{2.37}$$

where ρ_1, ρ_2 and σ are the fluid densities and the interfacial tension, respectively [14].

However, a modification of the Kelvin-Helmholtz mechanism, driven by an oscillatory base flow, presents a notable departure from this complexity. In this case, the oscillatory nature ensures that the average shear force is zero, mitigating the inclination for roll-up. Consequently, the resulting waves demonstrate greater regularity and exhibit a time-averaged left-right reflection symmetry. This symmetry contributes to the formation of standing or "frozen" waves rather than traveling waves. Such instability is frequently referred to as the Oscillatory Kelvin-Helmholtz instability (OKHI).

Numerous experimental and theoretical studies have been carried out on the Oscillatory Kelvin-Helmholtz Instability. These investigations aim to unravel the underlying mechanisms [17, 18, 19] of the phenomenon and assess the impact of various parameters, including surface tension [20, 21], viscosity [22, 23], as well as the amplitude and angular frequency of rotational [17, 18, 24] or horizontal [19, 22, 23] sinusoidal oscillatory forcing, on its behavior.

The interface between two immiscible liquids, such as silicon oil and water, layered in a gravitationally stable configuration and characterized by significant viscosity differences, when subjected to alternating rotational motion within the container, can deform [17]. When the azimuthal shear stresses reach a critical threshold, the interface between the two liquids destabilizes, resulting in the formation of waves along the periphery of the container (Figure 2.6a). These waves exhibited a sinusoidal shape in the direction perpendicular to the imposed motion (Fig. 2.6b*[left]*). The radial extent of these waves was limited to a few centimeters, and notably, no waves formed within a circular region at the center of the interface (Fig. 2.6b*[right]*). On the other hand, Figure 2.8 depicts qualitatively the evolution of frozen waves arising under horizontal vibrations, while the frequency of forcing is kept constant and the oscillation amplitude increases. The main effect is in increasing the height of frozen waves [22]. The dynamics in both cases of rotational or horizontal forcing are qualitatively similar. If the amplitude or frequency of the oscillation exceeds a critical value, interfacial waves will develop, Thus, for a given frequency, the flow becomes unstable at a certain amplitude. Similarly, for a given amplitude, the flow becomes unstable at a certain frequency [25].

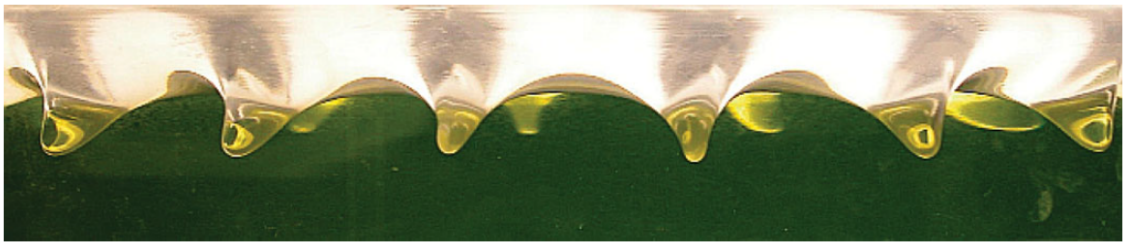

(a)

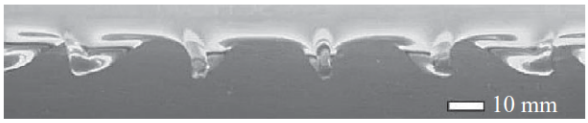

Linear evolution

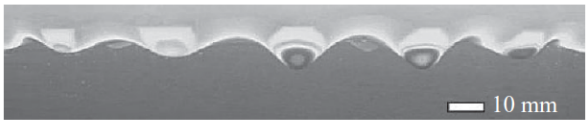

Nonlinear amplification

Final saturated state

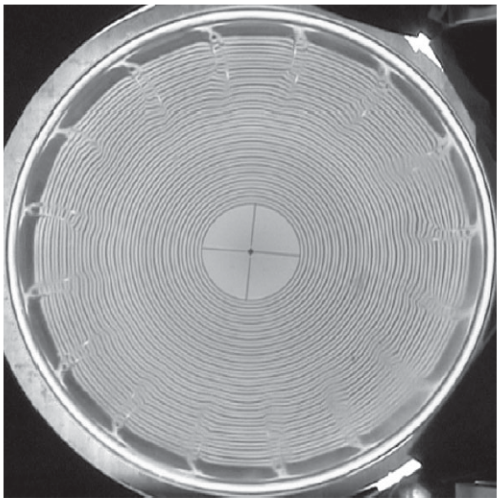

(b)

Figure 2.6. Oscillatory Kelvin-Helmholtz Instability. a) Frozen waves formed at silicon oil-water interface along a cylindrical container periphery. **b)** *[left]* Wave evolution from a lateral view and *[right]* final saturated state from a top view. Reproduced with permission from [17]. ©*Cambridge University Press, 2011.*

The critical parameters for characterizing instability include the velocity threshold at which wave relief emerges and the characteristic wavelength, specifically represented by the wavenumber, which defines the spacing between waves. Simplifying the modeling of the Oscillatory Kelvin-Helmholtz instability, researchers adopted an inviscid approach, disregarding the viscosity contrast effect in fluids. Kelly [26] and Lyubimov and Chereponov [27] formulated inviscid theories that anticipate an instability characterized by a threshold in relative velocity between two overlapped fluids and a most unstable wavenumber mode similar to the classical Kelvin-Helmholtz instability. Designed to address the interface between two immiscible fluids with comparable densities, the theory assumes the fluids are inviscid and overlapped within a vessel, experiencing disturbances due to horizontal vibrations [27]. The theory predicts a system that destabilizes for certain values of oscillation amplitude and frequency, dependent solely on surface tension and fluid densities. Furthermore, it anticipates that the characteristic wavelength of wave reliefs is the capillary length, regardless of forcing features. This theory will be presented in its entirety in Section 2.1.5, as it forms a crucial foundation for the current study and will be extensively utilized throughout the research.

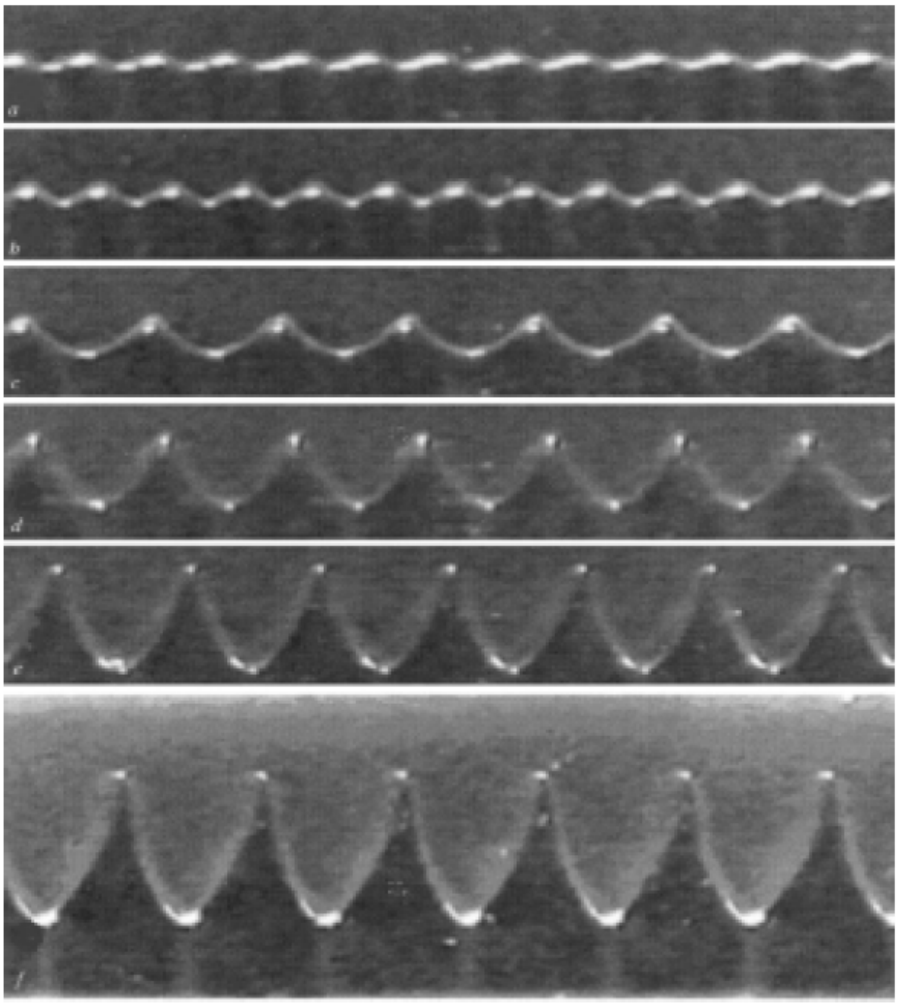

Figure 2.7. Frozen waves onset in horizontally vibration field. Change in the interface with the increase in vibration intensity. Reproduced with permission from [19]. ©*Plenum Publishing Corporation, 1969.*

Neglecting viscosity contrast simplifies the theory but fails to accurately predict the velocity threshold and characteristic wavelength. In actual systems, the inviscid theory holds when oscillation amplitude approaches zero and frequency is high [28]. The exploration of linear stability in oscillatory flows within thick viscous fluid layers involves examining dynamics within Stokes boundary layers for both layers [18]. The investigation, developed for the asymptotic scenario of small oscillation amplitude relative to wavelength, uncovered noteworthy impacts of oscillation frequency and viscosity contrast on instability thresholds and critical wavenumber. The interplay of different length scales accompanied these effects. Diverse instability mechanisms were suggested, resembling the classical Kelvin-Helmholtz instability for high-frequency flows and a short-wave instability akin to steady Couette flow for low-frequency flows. Despite being a short-wavelength instability, viscosity may prevail over inertia in certain parameter regimes. A destabilizing mechanism driven by viscosity contrast for the short-wavelength interfacial instability observed in two-layer Couette flow was introduced [29]. When a small perturbation displaces the interface, velocity adjustments occur

in both layers to maintain stress balance at the interface. This velocity perturbation manifests as counter-rotating vortices above and below the peaks of the perturbed interface. In scenarios where the upper fluid exhibits significantly higher viscosity than the lower one, the lower fluid bears most of the accommodation, leading to an increase in the disturbance magnitude with viscosity contrast. Although a minor contribution from inertia is necessary for interface destabilization within a linear theory, it plays a role by advecting vorticity distributions on both sides of the interface, creating out-of-phase components. As the counter-rotating vortices on either side of the interface differ in magnitude, their velocity disturbances do not cancel out. Consequently, their cumulative effect progressively deforms the interface, especially with larger viscosity contrasts. It was found that the velocity threshold and the wavenumber varied with the frequency. In particular, significantly lower thresholds and longer waves were found than those predicted by the inviscid theory of the oscillatory Kelvin–Helmholtz instability [17].

Experiments involving fluids with high viscosity and density contrast, layered in a horizontally vibrational field, were performed [19]. The horizontal vibration of the vessel generates a time-periodic basic shear flow [22]. Under conditions of weak vibrational influence, the fluid interface remains flat, and both fluids oscillate longitudinally in a plunger-like fashion with opposing phases. When the vibration frequency reaches a specific critical value (at a fixed amplitude), a two-dimensional periodic pattern of hills and valleys emerges on the interface, oriented perpendicularly to the vibration axis (see Figure 2.7). This stationary relief becomes observable. The crests of this relief oscillate at the vibration frequency with an amplitude much smaller than that of the cavity oscillation. The wave essentially stays in the same position on average, with its profile being "frozen" in the reference frame tied to the cavity. The quasi-steady relief exhibits similar properties to waves formed on the boundary of steady counterflows. By adjusting the frequency and amplitude of the external forcing, the critical value of the vibrational parameter for the onset of frozen waves monotonically decreases toward a constant threshold [19]. This trend aligns well with the stability predictions of Lyubimov and Cherepanov [27] for very high frequencies.

Through conducting experiments with fluids exhibiting significant density contrast and low interfacial tension, and formulating a theoretical framework that incorporates viscosity contrast, it was observed that the inviscid theory consistently underestimates the threshold for fluids with equal viscosities. In contrast, it generally overestimates the threshold for fluids with unequal viscosities [22].

When subjected to high-frequency forcing, the interface becomes unstable, exhibiting characteristics akin to the long-wave Kelvin-Helmholtz instability. Viscous dissipation has a limited destabilizing impact under these conditions. In the case of moderate-frequency vibrations, destabilization becomes more pronounced, particularly in systems with substantial viscosity contrast. In stark contrast, at low frequencies, viscosity acts to stabilize the fundamental flow by inhibiting long-wave perturbations. Generally, viscosity tends to suppress short-wave perturbations, while

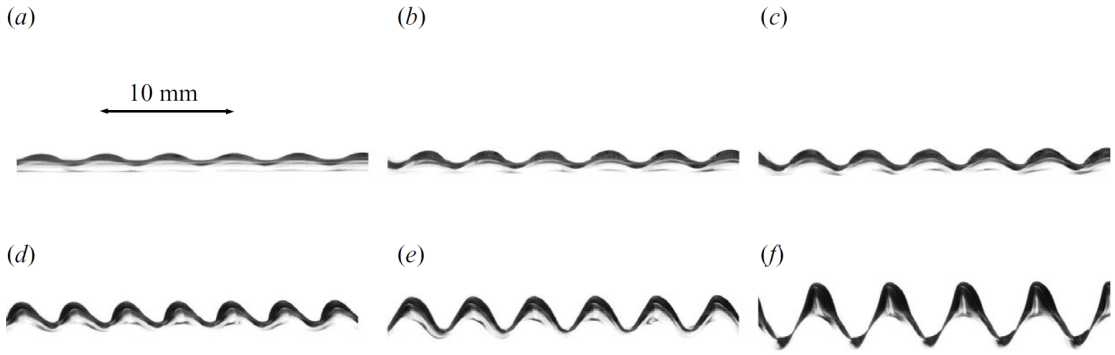

Figure 2.8. Frozen waves onset in horizontally vibration field. Change in interface with the increase of oscillation amplitude. Reproduced with permission from [22]. ©*Cambridge University Press, 2007.*

long-wave perturbations are less affected by its influence [23].

The onset of frozen waves in a rotating system can be influenced by interfacial tension, which depends on whether short or long wave destabilization occurs. When the system is disturbed by a low-frequency forcing, short wave destabilization emerges, and surface tension has a stabilizing effect. Conversely, high frequencies alter the instability range, leading to long wave disturbances that are not hindered by interfacial tension [20]. Similar findings were observed by [21].

Experiments aimed at assessing interfacial stability in a fluid with matched density were performed, investigating carbon dioxide liquid-vapour equilibrium system near its critical point [30]. Beyond a certain velocity threshold, frozen waves onset was observed. This wave exhibited a sine-like interface profile, remaining stationary in the reference frame of the vibrated sample cell. By manipulating vibration parameters, surface tension, and the density difference between the phases through temperature adjustments, it was determined that both the wavelength and amplitude of the stationary profile were influenced by the frequency and amplitude of the vibration. Moreover, these parameters were found to be proportional to the capillary length. These observations align with a model that assumes inviscid and incompressible flow [27], averaging the impact of vibration over a period. The resulting mechanism resembles a Kelvin-Helmholtz-like instability, arising from the relative motion between the two fluid phases.

The shear stresses causing this instability can be applied in different overall directions, creating two concentric fluid layers in a Hele-Shaw-like cell [31]. The cell is a short horizontal cylinder rotating around its axis, with the end walls forming a narrow gap. Under uniform rotation, the interface takes on an axisymmetric shape. However, as forcing modulation grows, the axisymmetric boundary loses stability, leading to the appearance of a regular quasi-stationary relief at the interface. The modulation-induced relief is a result of tangential velocity discontinuity due to interactions between the liquids and the cavity end walls, stemming from viscosity contrast. The viscosity contrast plays a dual role, causing tangential velocity discontinuity, and significantly influences the threshold of Kelvin-Helmholtz instability. This contrast results in a lower stability

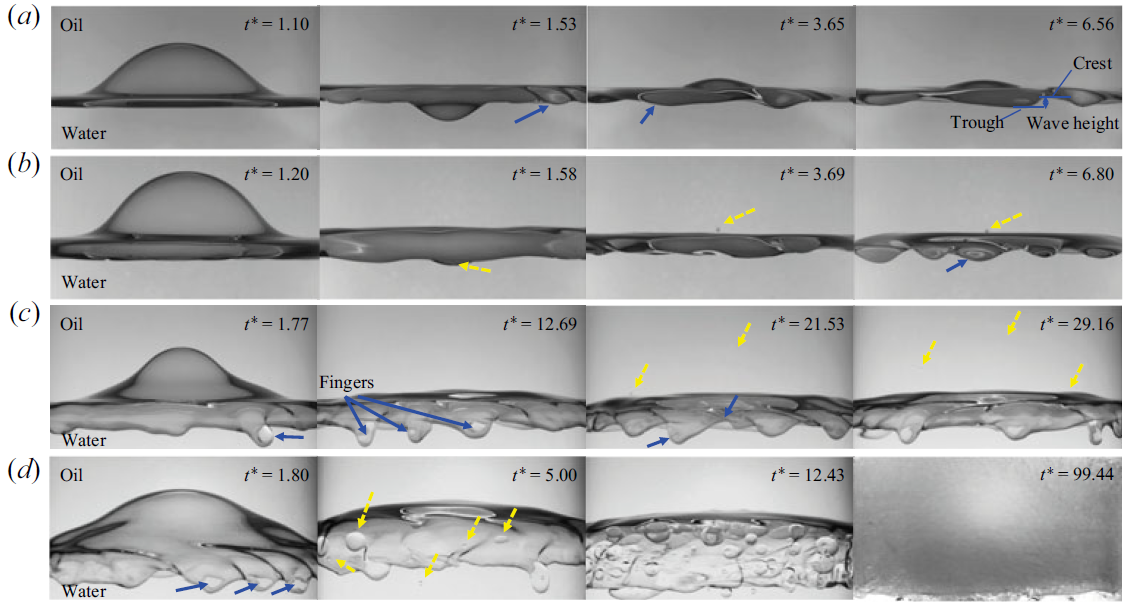

Figure 2.9. Droplet formation. Representative spatio-temporal evolution of the disturbed interface in a side view for high oscillation amplitude. Here, the Oscillatory Kelvin-Helmholtz instability is the underlying condition for droplets formation. Reproduced with permission from [24]. ©*Cambridge University Press, 2007.*

threshold and an increased relief wavelength.

A comprehensive study investigated the entire destabilization process of the interface between immiscible layered fluids within a cylindrical container subjected to oscillations around its axis [24]. This research is groundbreaking as it presents the first evidence that the Oscillatory Kelvin-Helmholtz (OKH) instability may underlie the onset of a different instability. Notably, at the initial stage of rotary oscillation, the oil–water interface experiences a significant rise in the core region due to faster momentum transfer from the container wall to the more viscous upper liquid (oil) compared to the lower liquid (water). This creates a large positive radial pressure gradient in the upper oil, causing water to bulge up with a convex curvature in the center of the container. The oscillatory motions of the oil–water interface in the central region, exhibiting both convex and concave curvatures (Figure 2.9), result from the periodically induced accelerating–decelerating flow and the associated pressure gradient. When the external rotary oscillations surpass the threshold for breaking the flat interface, interfacial waves emerge near the wall, where the relative motion between oil and water layers is most pronounced. These wave patterns display oil penetrating water and gradually fading away as the relative velocity decreases away from the vessel edge, defining a frozen waves pattern (indicated by blue arrow in Figure 2.9b. As rotational disturbances intensify further, exceeding the thresholds for wavy deformation near the wall, the formation of a single water droplet at the core region occurs (Figure 2.9b, yellow arrow). This droplet is generated during the downward motion of the bulging interface and bounces in sync with the periodic oscillation while remaining above the center area. The subsequent process involves the sequential formation of

multiple droplets near the container wall, evolving from finger-like patterns into elongated troughs and narrower crests (Figure 2.9c, blue arrows). In the final stage, the system forms an emulsion (Figure 2.9d). The initiation of the first oscillating waves in the near-wall region results from a combination of velocity-induced and standard Oscillatory Kelvin–Helmholtz instabilities. To form a single droplet at the core region, specific conditions must be met: the rise velocity of the interface must exceed a critical value related to vibrational inertia, and the centrifugal force in the near-wall region, characterized by the length scale of the Stokes boundary layer, should dominate over gravitational forces to form a falling jet. Once these conditions are satisfied, the critical interface shape is determined, and the destabilization of the jet is driven by surface tension, ultimately leading to the formation of an emulsion.

Examining the conditions under which the Oscillatory Kelvin-Helmholtz instability occurs facilitates a better understanding of the observed onset of the new instability in this context. Meanwhile, the well-documented occurrence of finger formation in existing literature provides a valuable backdrop for recognizing that the fingers observed in this study are entirely novel. Fingers can form during the displacement of fluids in the Hele-Shaw cell, known as Saffman-Taylor instability [32, 33, 34] and the accelerated spreading process, such as spin coating [35, 36, 37, 38, 39, 40, 41, 42].

In the spin coating process, a liquid droplet is applied onto a dry solid surface and subsequently spread by rotating the disk. In cases where the flow maintains axisymmetry, a uniform film is formed over time. However, these flows are susceptible to non-axisymmetric perturbations that can induce instability. When the initial instability occurs at the leading edge of the droplet, the liquid tends to preferentially flow through rivulets [36]. The destabilization process was reported [35, 36]. In the early stages, the circular spread of the droplet remains stable, as depicted in Figures 2.10a-b. Initially, the droplet profile is relatively flat, and the film height decreases near the contact line (Figure 2.10a). Subsequently, a bump forms near the droplet's rim, marked by a bright annulus clearly visible in Figure 2.10b. Small amplitude waves spontaneously emerge and modulate the rim. Over time, both the wave amplitude and the mean radius of the droplet increase, while the angular wavelength of the instability remains constant (Figures 2.10c-f). Wavy modulations of the contact line correspond to variations in the rim profile perpendicular to the primary flow, creating a capillary pressure gradient in that direction. This constitutes the fundamental instability mechanism for liquid films spread by an external force, contingent upon the existence of a protrusion in the profile. The capillary pressure gradient induces a secondary flow that generates small droplets, visible in Figure 2.10e near the contact line, ultimately leading to the formation of fingers (Figure 2.10f). The drop height and radius temporal evolution were evaluated, normalizing the time as t/t_0 where $T_0 \sim V^{(1/3)}\beta^{(5/3)}$, where V is the drop volume and $\beta = \gamma/\rho\omega^2 V$ is analogous to an inverse Bond number, taking into account the competition between the interfacial and centrifugal force. Both datasets collapse onto a master curve, highlighting the centrifugal effect.

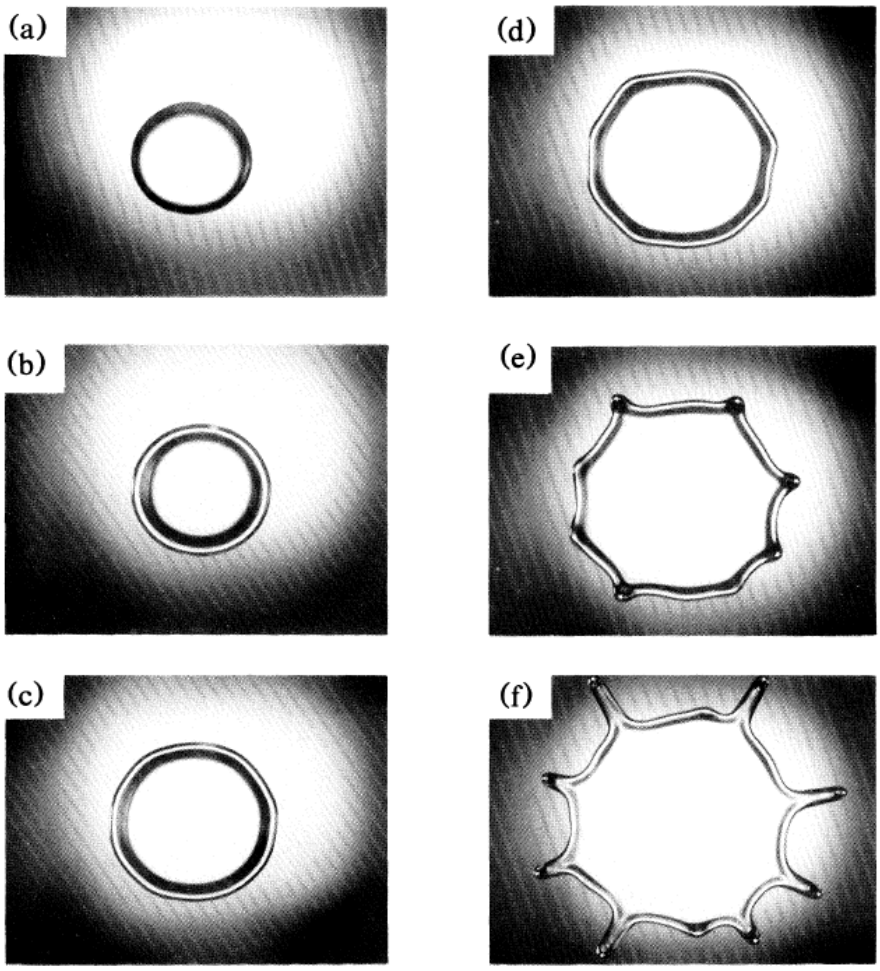

Figure 2.10. Radial Fingering. The different stages of spreading of a spinning drop. **a)** initial condition. **b)** formation of a bump. **c)** Wavy modulation of the rim at the early stage of instability. **d)** Wavy perturbation. **e)** Break up into fingers. **f)** Well-developed fingering. Reproduced with permission of [35]. ©*American Physical Society, 1989.*

The linear stability analysis of the contact line in the flow of a thin fluid film down an inclined plane, which is mathematically analogous to a flow influenced by centrifugal force, has been documented [38]. In this scenario, a thin film with a small dynamic contact angle, propelled by an external body force, exhibits instability leading to the formation of fingers perpendicular to the main flow. The instability is most pronounced in the capillary region near the contact line, where the surface tension force is comparable to viscous and gravitational forces. The calculation of the fastest growing wavelength is performed under the assumption of small-amplitude disturbances. These instabilities have implications for the finger patterns observed in spinning drops. The observed azimuthal wave number and finger growth rate align closely with theoretical predictions, even in the presence of fluid elasticity [36], but with a substantial shift in scaled time, suggesting that the scaling used in the theoretical expression is inappropriate [37]. The number of fingers increased with both angular speed and drop volume while the scaled growth rate of the fingers, in which the time is scaled with $\eta/h_0^2\rho\omega^{2}$", where η is the fluid viscosity, h_0 initial height of the drop,

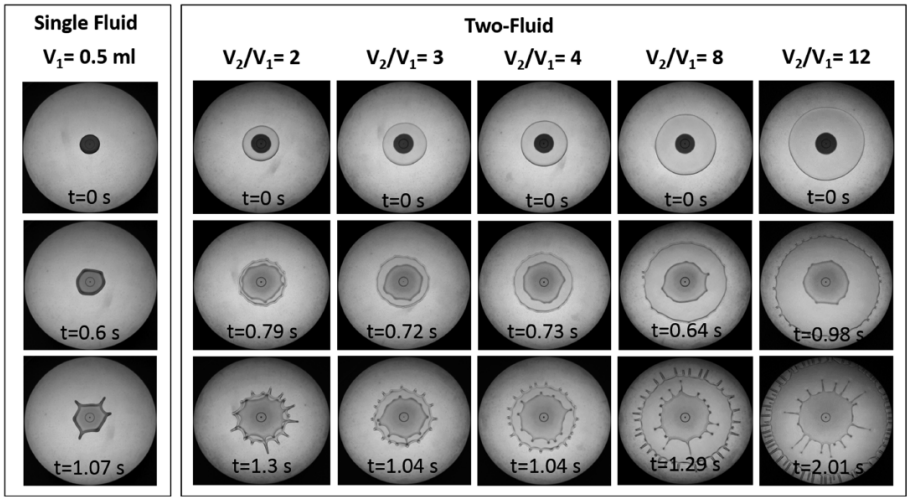

Figure 2.11. Fingers formation in layered system. The left panel corresponds to the spreading of a single liquid, while the panel on the right corresponds to the spreading of the same liquid when enclosed by another liquid on top for varying volume ratio of the two liquids. Reproduced with permission from [41]. ©*AIP Publishing, 2018.*

and *omega* the angular velocity, was constant, both in quantitative agreement with theoretical predictions [37]. However, alterations in contact angle and surface tension have a notable impact on the critical radius (the radius at which the instability arises). This, in turn, influences the observed number of fingers, as changes in capillary number or contact angle lead to variations in the bump's height and length during growth [36].

The instability of fingers can be influenced by the presence of particles in the spreading fluid. The critical radius for the initiation of instability demonstrates a rise with an increase in the particle fraction, reaching its highest value before experiencing a slight decrease, while the instability wavelength shows a non-monotonic dependence on the particle fraction [42].

The spreading of layered fluids due to centrifugal force was also considered [39, 40, 41]. The spreading of superposed drops of two Newtonian liquids on top of a horizontal spinning disk was experimentally [41] and theoretically [39] studied. The inner fluid is positioned at the center of a rotating disk, and the outer fluid is placed directly above it. This arrangement had a negligible impact on the outer liquid's spreading, but it significantly influenced the inner liquid's behavior. The thinning dynamics of both fluids were investigated using lubrication theory [39]. Considering factors such as viscosity and evaporation/condensation effects for layers with uniform thickness, the lower layer experiences a monotonic thinning process but never completely reaches zero thickness. When evaporation leads to mass loss, the upper layer disappears in a finite time, while condensation effects result in the upper layer approaching a steady-state thickness. Generally, disturbances affecting the lower layer have a more significant impact on the upper layer than disturbances in the upper layer have on the lower layer. Disturbances along the upper gas–liquid free surface propagates outward more rapidly than those along the lower liquid–liquid interface. Additionally, disturbances causing a decrease in film thickness tend to dissipate more slowly. Regarding the destabilization

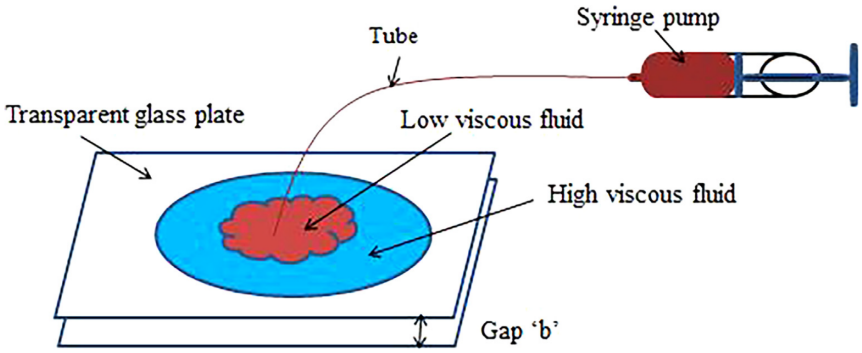

Figure 2.12. Radial Hele-Shaw cell. Reproduced with permission from [43], ©*Elsevier Ltd., 2019.*

scenario, the droplet exhibits increased spreading and a higher tendency to break into multiple fingers compared to the scenario where the same liquid is spreading without the presence of the outer liquid. Upon comparing the experimentally observed number of fingers with predictions from the existing theory for a single liquid [38], the theory tended to overestimate the number of fingers for the inner liquid when it was covered by an outer liquid. When considering a small but non-negligible surface tension ratio between the two liquids, the presence of the outer interface led to a reduction in the value of the most unstable wave number, also observed experimentally and indicating a correlation between the decrease in the number of fingers and the presence of the outer liquid. Furthermore, the sustained rotation of the disk resulted in the formation of droplets at the tips of the fingers, which then traveled outward. The development of fingers in this context resembles a single fluid, and the crucial condition for this phenomenon is the formation of bumps along the contact line of drops [35]. The size of the capillary bump grows larger as the viscosity ratio increases. Additionally, the capillary bump becomes sharper with a reduction in the interfacial tension ratio. The volume ratio increase does not impact the uniformity of the film. A consistent two-layer thin film can be established when the upper layer fluid is less viscous or when the surface tension between the upper gas-liquid interface exceeds the interfacial tension between the inner liquid-liquid interface [40].

The Saffman–Taylor instability, commonly referred to as viscous fingering, is the emergence of patterns within an unstable interface between two fluids in a porous medium [32]. In the radial Hele-Shaw cell, depicted in Figure 2.12, a static layer of highly viscous fluid is confined between two glass plates. Notably, one of these plates features a small aperture at its center. Utilizing a syringe pump, a less viscous fluid is introduced onto the surface of the thin viscous film through the central aperture in the plate. The lower-viscosity fluid travels across the surface of the high-viscosity fluid, exerting pressure and inducing the formation of a finger-like pattern at the interface between the two fluids. This distinctive pattern emerges as a result of viscous fingering instability, where the low-resistance hydraulic pathway facilitates the displacement of the fluid, giving rise to the characteristic viscous fingering pattern [34].

The onset and development of Saffman-Taylor instability can be influenced by a diverse set of

parameters, which can be summarized as follows [34]:

- Interfacial instabilities occur inherently only when the viscosity ratio is less than unity.
- Viscous fingering forms exclusively in systems with a viscosity ratio greater than unity, but external surface forces (such as an electric field) must be present.
- Newtonian fluids exhibit a dense branching pattern compared to non-Newtonian fluids.
- Fractal fingers emerge due to successive shielding of alternating fingers.
- Increasing injection rate leads to wider fingers but a reduced number of fingers.
- Higher injection rates result in narrower fingers and increased side branching.
- In highly confined systems, the amplitude and number of fingers increase, and the growing fingers are independent of plate confinement.
- Dendrite-like finger patterns can be formed with the assistance of anisotropy.
- Viscous fingering patterns manifest earlier in shear-thinning fluids compared to shear-thickening fluids, and shear-thinning fluids are less stable than Newtonian fluids.
- Increased viscosity ratio, elasticity number, and capillary number enhance sweep efficiency and flow stability. Conversely, increased mobility ratio and mobility factor lead to decreased sweep efficiency.
- Dynamic wetting delays finger-tip splitting, and finger shielding diminishes with a higher mobility ratio.
- Highly ramified and long fingers appear at a high viscosity ratio, and instability is quantified by the unstable wavelength.
- Wetting films stabilize finger formation and regulate finger growth.

2.1.5 Oscillatory Kelvin-Helmholtz Instability Inviscid Theory

The inviscid theory is applicable for modeling the Oscillatory Kelvin-Helmholtz instability, which is the fundamental mechanism underlying the emergence of the new fingers instability.

Kelly [26] and Lyubimov and Chereponov [27] developed inviscid theories that predict an instability characterized by a threshold in relative velocity between the two overlapped fluids and a most unstable wavenumber mode identical to the classical Kelvin-Helmholtz instability. The theory was initially formulated to address the interface between two immiscible fluids with comparable densities and supposed inviscid, overlapped within a vessel, and that experience disturbance due to horizontal vibrations [27]. This concept is reintroduced here in the context of miscible interfaces. The dynamic vibration of a container significantly impacts the response of fluid interfaces within

it. When a vessel experiences intense horizontal vibrations and contains a fluid with a free surface, the fluid tends to accumulate near one of the vertical walls of the vessel. The free surface remains nearly flat and stationary with respect to the vessel, with the angle of inclination to the horizontal depending on the vibration frequency. However, when the vessel holds a system of immiscible fluids with comparable but different densities, horizontal vibrations induce the formation of a stable wave pattern at the fluid interface.

Considering two overlapped fluids fill a vessel, the mutual interface is horizontal, and it is perturbed by

$$r = ak\ sin\ ft + r_0 \tag{2.38}$$

where r and r_0 are the radial coordinate and its mean, $f\ [Hz]$ is the frequency of the vibrations, a is their amplitude and k is the unit vector along the axis of the vibrations.

In the framework of the vessel, the equations of the fluid motion

$$\frac{\partial v_\beta}{\partial t} + (v_\beta \nabla)v_\beta = -\frac{1}{\rho_\beta}\nabla p_\beta + v_\beta \Delta v_\beta - g\gamma + af^2 k\ sin\ ft \tag{2.39}$$

where γ is the unit vector directed vertically upward and $\beta = 1, 2$ labels the fluids. The remaining notation is standard. The no-slip conditions are satisfied on the vessel's rigid walls. The stress balance, rate continuity, and kinematic conditions are satisfied at the interface $F(r, t) = 0$:

$$-[\sigma_{i,j}]n_j + [p]n_i = \sigma(\nabla n)n_i \tag{2.40}$$

$$[v] = 0,\ \frac{\partial F}{\partial t} + v\nabla F = 0,\ n = \frac{\nabla F}{|\nabla F|} \tag{2.41}$$

where $\sigma_{i,j}$ is the viscous stress tensor, n the normal vector to the surface and σ is the surface tension.

When $f\ >>\ v/L^2$, where L is the characteristic length of the hydrodynamic structures, all processes can be divided into fast and slow. The non-linear terms can be discarded if $a^2\ f^2/L\ <<\ a\ f^2$, namely imposing constraints on the amplitude of vibrations $a\ <<\ L$, decoupling the problem into fast pulsation and average parts. The conditions $f\ >>\ a\ L^2$ and $a\ << L$ are satisfied, assuming the amplitude of the vibrations is small and the vibration frequency is significant. Introducing the time sequence

$$t_{-1} = ft,\ t_0 = t,\ t_1 = f^{-1}t, ... \tag{2.42}$$

and assuming that all the variables in Equations 2.39, 2.40, 2.41 depend on both the fast time t_{-1} and the slow times $t_0,\ t_1$..., the derivative of velocity and pressure fields, and the interface function F with respect to time can be represented in the form of series

$$v_\beta = v_{beta}^{(0)} + f^{-1}v_\beta^{(1)} + ...,\ p_\beta = fp_\beta^{-t} + p_\beta^{(0)} + f^{-1}p_\beta^{(1)} + ...,\ F = F_0 + f^{(-1)}f_1 + ... \tag{2.43}$$

The Equation 2.39 gives the following leading orders in f^{-1}:

$$f\frac{\partial v_\beta}{\partial t_{-1}} = -f^{-1}\frac{\nabla p_\beta}{\rho_\beta} + bfk\ sin\ t_{-1},\ \nabla v_\beta^{(0)} = 0 \tag{2.44}$$

whence

$$v_\beta = bV_\beta\ cos\ t_{-1} + u_\beta,\ p_\beta^{(-1)} = bP_\beta\ sin\ t_{-1} \tag{2.45}$$

$$\rho_\beta(V_\beta + k) = \nabla P_\beta,\ \nabla V_\beta = 0, \nabla u_\beta = 0 \tag{2.46}$$

The fields $V_\beta, u_\beta, P_\beta$ do not depend on the fast time t_{-1}. Given the previous assumption, the thickness of the viscous skin layer near the wall is small in comparison with the dimensions of the vessel. The no-slip condition can be changed with a no-flow condition because V_β is not a viscosity function, namely the velocity's second spatial derivatives. From the boundary conditions 2.41, the principal part of F does not depend on the fast time. Substituting the Eq. 2.45 in the Eq. 2.39 and averaging them over the vibration period, the equation for the mean velocity u_β

$$\frac{\partial u_\beta}{\partial t} + (u_\beta\nabla)u_\beta = -\nabla\left(\frac{p_\beta}{\rho_\beta} + b^2V_\beta^2\right) + v_\beta\Delta u_\beta - g\gamma \tag{2.47}$$

with boundary conditions

$$-[\sigma_{i,j}]n_j + [p]n_i + \frac{1}{2}b^2[\rho V_n W_n]n_i = \sigma(\nabla n)n_i \tag{2.48}$$

$$[\rho W_\tau] = 0,\ [W_n] = 0,\ \frac{\partial F}{\partial t} + u\nabla F = 0, W_\beta = V_\beta + k \tag{2.49}$$

omitting the subscript (superscript) zero; n and τ specify the normal and tangential vector components to the interface, respectively. The tensor $\sigma_{i,j}$ is determined in the field of mean velocity u_β.

Considering the equilibrium condition, in which there is no averaged motion and the interface is steady,

$$rot\ W_\beta = 0, \nabla W_\beta = 0, W_{\beta n}|_0 = k_n \tag{2.50}$$

and, on the interface $F(r) = 0$, conditions 2.49 are satisfied while the Eq. 2.48 becomes

$$[p] + \frac{1}{2}b^2[\rho V_n W_n] = \sigma(\nabla n) \tag{2.51}$$

and using the Eq. 2.47 for determining the equilibrium pressures($u_\beta = 0$).

Let's consider the system reported in Fig. 4.19a, the horizontal vessel dimension is assumed large, in comparison with h, and the vessel is unbounded in this direction. The vibration field is in the x direction. Solving the Equations from 2.49 to 2.51 at the interface $z = \zeta(x, y)$

$$rot\ W_\beta = 0, \nabla W_\beta = 0 \tag{2.52}$$

$$W_{1z}(z = -h) = 0, W_{2z}(z = h) = 0, W_{1n} = W_{2n}, \rho_1 W_{1\tau} = \rho_2 W_{2\tau} \tag{2.53}$$

$$\frac{b^2}{4}[W_{1n}^2(\rho_1 - \rho_2) - (\rho_1 W_{1\tau}^2 - \rho_2 W_{2\tau}^2] - (\rho_1 - \rho_2)g\zeta + \sigma(\nabla n) = const \tag{2.54}$$

The problem has an equilibrium solution:

$$\zeta = 0,\ W_{1x} = \frac{2\rho_2}{\rho_1 + \rho_2},\ W_{2x} = \frac{2\rho_1}{\rho_1 + \rho_2},\ W_{1y} = W_{2y} = W_{2z} = W_{1z} = 0, \int_{-h}^{\zeta} V_{1x}dz + \int_{\zeta}^{h} V_{2x}dz = 0 \tag{2.55}$$

Because the vibrations are along the x-axis, the considered plane perturbations depend on x and z. Since W_β are solenoidal in two-dimensional problem, the stream functions Ψ and Φ, that are harmonic, can be introduced

$$W_{1x} = \frac{2\rho_2}{\rho_1 + \rho_2} + \frac{\partial \Psi}{\partial z},\ W_{1z} = -\frac{\partial \Psi}{\partial x},\ W_{2x} = \frac{2\rho_1}{\rho_1 + \rho_2} + \frac{\partial \Phi}{\partial z},\ W_{2z} = -\frac{\partial \Phi}{\partial x}, \Delta\Psi = 0,\ \Delta\Phi = 0 \tag{2.56}$$

Linearizing the problem near the equilibrium solution 2.55, the bifurcation curve is obtained

$$b^2 = \frac{(\rho_1 + \rho_2)^3}{2\rho_1\rho_2(\rho_1 - \rho_2)^2}[\sigma k + (\rho_1 - \rho_2)gk^{-1}]th\ kh \tag{2.57}$$

The Eq. 2.57 is the critical value for the amplitude of the vibration rate. Above it, the plane interface becomes unstable and a wave relief develops. The minimum critical value is

$$b_{min}^2 = \frac{(\rho_1 + \rho_2)^3}{2\rho_1\rho_2(\rho_1 - \rho_2)^2}[\sigma + (\rho_1 - \rho_2)g]^{(1/2)} \tag{2.58}$$

and a wave relief can develop at the interface of the two fluids, with the wavelength

$$\lambda_{cap} = 2\pi\sqrt{\frac{\sigma}{(\rho_1 - \rho_2)g}} \tag{2.59}$$

namely the capillary wavelength. Therefore, the critical inviscid wavenumber can be defined as

$$k_{cr,inv} = 2\pi/\lambda_{cap} \tag{2.60}$$

The Eq.2.58 can be written as suggested by [30]

$$(af)^2_{cr,inv} = \frac{(\rho_1+\rho_2)^3}{2\rho_1\rho_2(\rho_1-\rho_2)}\left[\frac{\sigma g}{(\rho_1-\rho_2)}\right]^{1/2} \tag{2.61}$$

The dispersion relation given by Eq. 2.61 is analogous to that of the classical Kelvin-Helmhotlz instability, where short and long-wavelength perturbations are suppressed by the stabilizing effect of capillary and buoyancy force respectively. Thus, in absence of viscosity, the capillary length is the natural length scale of the instability [22]. The inviscid theory consistently underestimates the instability threshold for liquids of equal viscosity but generally overestimates the threshold for fluids of unequal viscosity [22]. In real systems, the theory is valid in the limit of vanishing oscillation amplitude and high frequencies [28], under investigation in this research work.

2.2 Miscible Interface

2.2.1 Historical Perspective

The idea of capillary force arising in systems formed by miscible fluids took hold more than one century ago. The main theoretical work is Korteweg's [44], whose theory will be reported in the next section. His work found its raison d'être in many communications, letters, and works before 1901, in which the existence of an appreciable capillary force at the interface between two miscible fluids was debated. Conflicting theories were published before 1901. Bosscha, in the proceedings of the Academy of Sciences of Amsterdam 1871/72, reported observations about the formation of bulges of a liquid in a miscible environment, which more and more take the form of drops [44]. In his work, a test tube with a tapered, funnel-shaped bottom was partially immersed in a water-filled cylindrical vessel. As the water level inside the tube matched that of the vessel, a soluble crystal was gently introduced into the tube's water. The liquid within the tube becomes notably denser than the surrounding water, prompting it to flow through its fine opening, creating a slender stream. This liquid thread is a regular water jet, although it moves considerably slower. As the thread elongates, bulges or beads along the thread's length happen. These bulges continue to develop until they reach a critical point, at which they separate into individual drops, allowing the individual drops to fall freely (**ndr.** Plateau-Rayleigh instability). Bosscha assumed the existence of capillary force, but his idea was not shared by Thomson and Newall, associating such phenomena, which they observed independently, with instabilities of motion [45].

Later, Freundlich wrote, in his work [46],

" ...there is little new to be said .... We have only to remember here we are in the end always dealing with solutions. For the one liquid will always be soluble in the other to some degree, however small. Hence the dynamic tension of liquids, when first brought into contact, is to be distinguished from the static tension, when the two liquids are mutually saturated. Not only do liquids that are not miscible in all proportions have a mutual surface tension; but even two completely miscible liquids, before they have united to form one phase, exhibit a dynamic interfacial tension. For we get by careful overlaying of any two liquids a definite meniscus, a jet of one liquid may be generated in another, and so on. The tension decreases rapidly during the process of solution, and becomes zero as soon as the two liquids have mixed completely."

The presence of a significant interfacial tension at the boundary between two miscible fluids remains a topic of ongoing debate. Despite the formulation of Korteweg's theory and numerous experimental studies conducted over the past three decades aimed at measuring or demonstrating its impact on the initiation of hydrodynamic instabilities, uncertainties persist in the scientific discourse.

2.2.2 Korteweg's Stresses

Korteweg argued that density gradients could cause stresses that mimic the immiscible interfacial tension [44]. He proposed smooth constitutive equations for stresses arising from density gradients. His work was motivated by Van der Waals's theory (of which a modern derivation is reported in 2.1.2), in which a finite thickness of the interface was assumed, defining the interface as a continuous region in which a density gradient is present. Diffuse interface theory provides a framework for modeling the evolution of miscible interfaces with dynamic surface tension [47]. Such a description is suitable for miscible fluid, as reported below.

A continuum approach with a compressible fluids model was proposed for the same issue reported in 2.1.2. The total stress is the sum of the usual Nevier-Stokes type stress $T^{(1)}$ and $T_{(2}$, depending on density derivatives

$$T_{ij}^{(1)} = -p\delta_{ij} + \mu\left(\frac{\partial u_i}{\partial x_j} + \frac{\partial u_j}{\partial x_i}\right) + \lambda\frac{\partial u_l}{\partial x_l}\delta_{ij} \tag{2.62}$$

and

$$T_{ij}^{(2)} = (\gamma\nabla^2\rho - \alpha\nabla\rho\cdot\nabla\rho)\delta_{ij} - \beta\frac{\partial\rho}{\partial x_i}\frac{\partial\rho}{\partial x_j} + \delta\frac{\partial^2\rho}{\partial x_i\partial x_j} \tag{2.63}$$

where p and the coefficient $\alpha, \beta, \delta, \gamma, \mu$ and δ are function of density rho and temperature θ.

This theory can be reduced to the classical theory of capillarity [1, 3]. As an illustration, considering a spherical mass of fluid in equilibrium, with a radial variation of density $\rho = \rho(r)$, in spherical coordinates, the Eq.2.62 and 2.63 became

$$T^{<rr>} = -p - (\alpha+\beta)\rho'^2 + \gamma(\rho'' + \frac{2}{r}\rho') + \delta\rho'' \tag{2.64}$$

$$T^{<\theta\theta>} = T^{<\phi\phi>} = -p - \alpha\rho'^2 + \gamma(\rho'' + \frac{2}{r}\rho') + \delta\frac{\rho'}{r} \tag{2.65}$$

where $\rho' = dp/dr$, $T^{<rr>} = e_r T e_r$ and the stress tensor T

$$T + pI = \lambda(trD)I + 2\mu D - \alpha(\nabla\rho)^2 I - \beta\nabla\cdot\nabla\rho + \gamma(\Delta\rho)I + \delta\nabla^2\rho \tag{2.66}$$

If $b(r)$ is the radial component of the external body force, at equilibrium $b^{<\theta>} = b^{<\phi>} = 0$ and the radial component of the momentum equation

$$\frac{\partial T^{<rr>}}{\partial r} + \frac{2}{r}(T^{<rr>} - T^{<\theta\theta>} + \rho b(r) = 0 \tag{2.67}$$

Assuming density as in Fig. 2.2, it varies in $r_1 < r < r_2$ and, outside this range, is constant. So

$$T^{<rr>}\,|_{r_1}^{r_2} = -\int_{r_1}^{r_2}\rho b(r)dr - \frac{2\delta\rho'}{r}\,|_{r_1}^{r_2} + 2\int_{r_1}^{r_2}\frac{\beta + \partial\delta/\partial\rho}{r}\rho'^2 dr \tag{2.68}$$

Assuming $\rho' \to 0$ for $r = r_1$ and $r = r_2$, because far from the transient region, if $r_1 \to r_0$, $r_1 \to r_0$ and

$$(\beta + \frac{\partial \delta}{\partial \rho})\rho'^2 \to S^* \delta(r - r_0) \tag{2.69}$$

where $\delta(r - r_0)$ is the Dirac's delta function, the first term of 2.68 vanishes and the second term reduces to $2S^*/r_0$, where S^* is the surface tension, obtain the classical jump for the normal stress at the interface between two fluid with different densities. This theory can be applied to the slow diffusion of miscible incompressible liquids, modeled as a simple mixture. Since the density of the mixture is a linear function of the volume fraction (it changes with diffusion), the velocity can be decomposed into a solenoidal and expansion part. The latter is proportional to the volume gradient and it is due to diffusion, being important at early times of mixing. Considering a system formed by two fluids, with mass for unit volume γ and υ, the mass, in a generic material volume $V(t)$, for each fluid can change only if γ (or υ) diffuse across the boundary of V. So,

$$\frac{d}{dt}\int_{V(t)} \gamma dV = -\int_{\partial V} \mathbf{q}_\gamma \cdot \mathbf{n} dS \tag{2.70}$$

where q_γ is the flux of γ. Because of $V(t)$ is a material volume

$$\frac{d}{dt}\int_{V(t)} \rho dV = 0 \tag{2.71}$$

with $\rho = m/V$. Being J the Jacobian of the transformation from $V(t)$ to V_0

$$\frac{dJ}{dt} = J \; div \; \mathbf{u} \tag{2.72}$$

and $dV = JdV_0$, bringing the time derivative under the integral

$$\int_V \frac{d\rho}{dt} + \rho \; div \; \mathbf{u} \; dV = 0 \tag{2.73}$$

$$\int_V \frac{d\gamma}{dt} + \gamma \; div \; \mathbf{u} + div \; \mathbf{q}_\gamma \; dV = 0 \tag{2.74}$$

thus,

$$\frac{d\gamma}{dt} + \gamma \; div \; \mathbf{u} = -div \; \mathbf{q}_\gamma \tag{2.75}$$

In the isothermal case, $d\rho/dt = \rho'(\gamma)d\gamma/dt \neq 0$ and

$$div \; \mathbf{u} = -\frac{1}{\rho}\frac{d\rho}{dt} = \frac{1}{\rho}\rho'(\gamma)\frac{d\gamma}{dt} \neq 0 \tag{2.76}$$

Supposing a simple solution, $\rho = \gamma + \upsilon$, the Eq. 2.75 can be applied also to υ. The continuity

equation 2.76 can be written as

$$\frac{d\upsilon}{dt} + \frac{d\gamma}{dt} + (\upsilon + \gamma)\ div\mathbf{u} = 0 \tag{2.77}$$

Using the Eq. 2.75, 2.76, 2.77

$$div\ (\mathbf{q}_\upsilon + \mathbf{q}_\gamma) = 0 \tag{2.78}$$

and for conserving the total mass

$$\int_{\partial V} (\mathbf{q}_\upsilon + \mathbf{q}_\gamma) \cdot n\ dS = 0 \tag{2.79}$$

by implying that $\mathbf{q}_\gamma \cdot \mathbf{n} = \mathbf{q}_\upsilon \cdot \mathbf{n} = 0$. If the volume V does not change on mixing, $V = V_\gamma + V_\upsilon$ and density can be expressed as function of volume fraction $\phi = V_\gamma / V$ by

$$\rho(\phi) = \rho_\gamma \phi + \rho_\upsilon (1 - \phi) = \gamma + \upsilon \tag{2.80}$$

where ρ_γ and ρ_υ are the density of the two fluids, the constitutive equation of the fluxes can be expressed as non-linear Fick's law

$$\mathbf{q}_\gamma = -D_\gamma(\phi)\nabla(\rho_\gamma \phi) \tag{2.81}$$

$$\mathbf{q}_\upsilon = -D_\upsilon(\phi)\nabla(\rho_\upsilon (1 - \phi)) \tag{2.82}$$

and, substituting in 2.79

$$div\ [(D_\upsilon \rho_\upsilon - D_\gamma \rho_\gamma)\nabla\phi] = 0 \tag{2.83}$$

at each point in V, the diffusion functions ratio

$$\frac{D_\upsilon}{D_\gamma} = \frac{\rho_\gamma}{\rho_\upsilon} \tag{2.84}$$

is constant.

Since the density of a simple mixture changes with diffusion, the velocity field is not solenoidal, but the Eq. 2.75 and 2.76 imply $div\ \mathbf{W} = 0$ and $div\ \hat{\mathbf{W}} = 0$, where $\mathbf{W} = \mathbf{u} - [(\rho_\gamma - \rho_\upsilon)/\rho_\gamma \rho_\upsilon]\mathbf{q}_\gamma$ and $\mathbf{W} = \mathbf{u} - [(\rho_\upsilon - \rho_\gamma)/\rho_\gamma \rho_\upsilon]\mathbf{q}_\upsilon$, only when the Boussinesq approximations are relaxed and $\rho = \rho^*(1 + \beta T)^{-1}$, so$\mathbf{W} = \mathbf{u} - \beta\kappa\nabla T$, where ρ^* and β are constant and κ is the thermo-diffusion coefficient.

The usual diffusion equation reported by Landau and Lifshitz [48] is

$$\rho\frac{d\tilde{\phi}}{dt} = -div\ \mathbf{i} \tag{2.85}$$

where

$$\tilde{\phi} = m_\gamma / m = \gamma / \rho \tag{2.86}$$

is the mass fraction, m is the total mass and i is the diffusion flux. Substituting 2.86 in 2.85 and using the Eq. 2.76, the left side of 2.85

$$\rho \frac{d\gamma/\rho}{dt} = \frac{d\gamma}{dt} + \gamma \; div \; \mathbf{u} \tag{2.87}$$

being

$$div \; \mathbf{i} = div \; \mathbf{q}_\gamma \tag{2.88}$$

After combining Eq. 2.87 and 2.88,

$$\frac{d\phi}{dt} + div \; (\phi \mathbf{u}) = div \; [D_\gamma(\phi) \nabla \phi] \tag{2.89}$$

$$D_\gamma = \frac{\rho_\upsilon D(\phi)}{\rho_\gamma \phi + \rho_\upsilon (1 - \phi)} \tag{2.90}$$

Generalizing Korteweg's formula 2.63,

$$T_{ij}^{(2)} = \delta_1 \frac{\partial \rho}{\partial x_i} \frac{\partial \rho}{\partial x_j} + \delta_2 \frac{\partial \phi}{\partial x_i} \frac{\partial \phi}{\partial x_j} + \gamma_1 \frac{\partial^2 \rho}{\partial x_i \partial x_j} + \gamma_2 \frac{\partial^2 \phi}{\partial x_i \partial x_j} + \gamma_3 \left(\frac{\partial \rho}{\partial x_i} \frac{\partial \phi}{\partial x_j} + \frac{\partial \rho}{\partial x_j} \frac{\partial \phi}{\partial x_i} \right) \tag{2.91}$$

it is invariant to a change of fluids in the mixture and isotropic. The parameters $\delta_1, \delta_2, \gamma_1, \gamma_2$ and γ_3 depend on ρ, ϕ and temperature θ. Such stresses become important in high gradients regions, whose effect mimics the interfacial tension. Considering a simple mixture, the dependence of ρ on ϕ is expressed by the Eq. 2.80 and $\rho_\upsilon, \rho_\gamma$ depend on θ. A term for pressure must be entered as a mechanical variable

$$p = -\frac{1}{3} trace \; \mathbf{T} \tag{2.92}$$

Splitting T into a pressure and a deviator

$$\mathbf{T} = -p\mathbf{I} + \mathbf{T}^D \tag{2.93}$$

where

$$T_{ij}^D = 2\mu D_{ij} - \frac{2}{3}\delta_{ij} \; \mu div \; \mathbf{u} + \tau_{ij} \tag{2.94}$$

and

$$\tau = \mathbf{T}^{(2)} - \frac{1}{3}\mathbf{I} tr \mathbf{T}^{(2)} \tag{2.95}$$

are traceless.

The seven unknowns $(\mathbf{u}, p, \rho, \theta, \phi)$ satisfy the continuity equation 2.76, the simple mixture equation 2.80, the diffusion equations 2.89 and 2.90, an energy equation and, the equation of

momentum

$$\rho \frac{d\mathbf{u}}{dt} = -\nabla p + div\ \mathbf{T}^D + \rho \mathbf{g} \tag{2.96}$$

As reported in [4], with a thermodynamic approach, the Effective Interfacial Tension (EIT, *effective* is used to designate the surface tension in miscible systems) is derived from

$$\Gamma_e = \frac{\partial F}{\partial A} \tag{2.97}$$

where F is the mixing free energy of the two fluids and A is the interfacial area. Assuming local equilibrium [49],

$$F = \int_V f(\phi, \nabla\phi) dV = \int_V [f_0(\phi) + \kappa(\nabla\phi)^2 + [O(\nabla\phi)]^4] dV \tag{2.98}$$

where f_0 is the free energy of an homogeneous mixture and κ is the Korteweg constant, an unknown empirical coefficient. Assuming small composition gradients and a flat interface, the Eq. 2.98 can be integrated over the coordinates (x, y), tangential to the interface, obtaining F as function of z. Substituting in 2.97

$$\Gamma_e = \kappa \int_{-\frac{\delta}{2}}^{\frac{\delta}{2}} (\nabla\phi)^2 dz \tag{2.99}$$

and assuming a linear concentration profile in the transition zone, the Eq. 2.99 can be simplified as

$$\Gamma_e = \kappa \frac{(\nabla\phi)^2}{\delta} \tag{2.100}$$

where $\nabla\phi = \phi_1 - \phi_2$ is the change in composition. Zeldovich has proposed similar conclusions [50], deriving from thermodynamics that a capillary force should also exist in miscible systems, and it can be found without assuming the equilibrium [51]. The Eq. 2.100 was also proposed by Smith *et al.* [52] and, in the current context, it serves as the foundational basis for interpreting experiments that explore off-equilibrium interfacial tension.

More recently, many works presented mathematical analysis and numerical simulation for transient capillary phenomena in miscible fluids [53, 54, 55, 56]. The model includes the Nevier-Stokes equations with a Korteweg stress term, diffusion, and convection. Simulations showed convection flows arise in various configurations, with concentration or temperature gradient, similar to surface tension-induced convection or Marangoni convection. This is attributed to effective dynamic interfacial tension [53, 54]. The Korteweg stress-based model offers a means to capture these complex diffusion-convection dynamics.

2.2.3 *Effective Interfacial Tension*

Many attempts were made to measure the interfacial tension between miscible fluids, using several methods. Quincke made the first measurements [57], using the method of Drop Weight

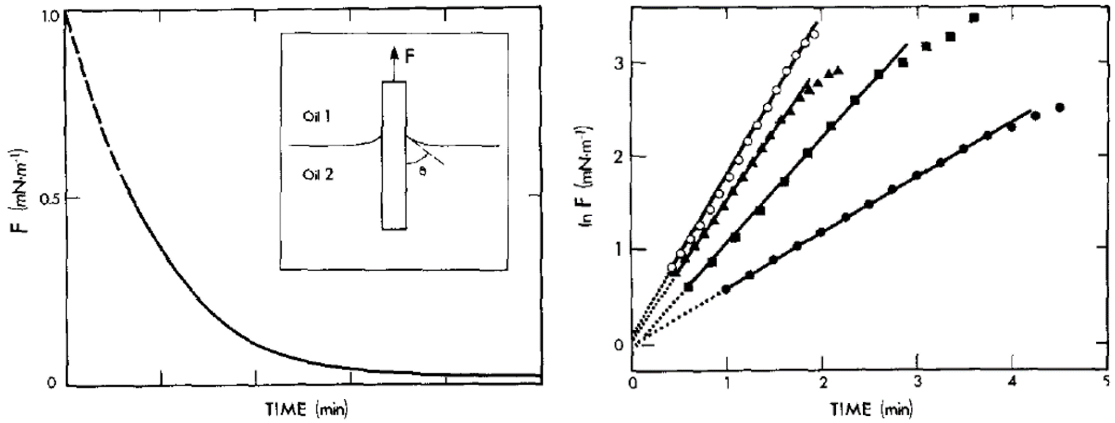

(a) (b)

Figure 2.13. Measured capillary force for 2000cs-1cs silicon oils interface. a) Typical capillary force decay (Inset: Sketch of the experimental system). **b)** Logarithm of capillary force in time for different experimental runs. The extrapolated force for $t = 0$ is, for all the runs, $F_0 = 1mN/m$. Reproduced with the permission from [52]. ©*Elsevier Inc., 1981.*

for testing Ethyl Alcohol and Aqueous Salt solution (sulfate of zinc, copper, etc...) in contact, miscible in all proportions. In these systems, the drop keeps its shape for a while, allowing *EIT* evaluation at an early time of contact. The obtained values were in the range of 0.8 to 3 mN/m. The Wilhelmy Plate method was also used for such measurements [52]. Smith *et al.* measured the *EIT* in 2000 $cs - 1$ cs silicon oils system, over a period of time, extrapolating the value to the time of contact. The interdiffusion is too slow for such systems to allow this kind of measurement. A Wilhelmy balance was loaded with the denser silicon oil, and then the less dense was poured on the other (Fig. 2.13a-insert). This method makes use of

$$P = 2(l + d)\sigma cos\theta \tag{2.101}$$

where l and d are the length and the thickness of the plate, respectively, σ is the interfacial tension, and θ is the apparent contact angle. Because of the difficulties in measuring θ, the capillary force for unit length was measured

$$F = \sigma cos\theta = P/[2(l + d)] \tag{2.102}$$

as a function of time. In Fig.2.13a, the capillary force decay is reported. In Fig. 2.13b, F as a function of time, for different experimental runs, is reported. Here, according to the theory, the capillary force should decay as $t^{-1/2}$, but the experimental results show slopes that vary between 0.6 to 1.4 due to the difficulties in keeping the same initial condition for each run. The extrapolation to $t = 0$ leads to the same value of force, 10^{-3} mN/m, confirming the consistency for the initial time. This technique and the Drop Weight Method are not suited for making measurements of very low interfacial tension.

Two methods are valuable for assessing extremely small interfacial tension: the Spinning-Drop

Tensiometry(SDT) [58, 59, 60, 61, 62], for the first time proposed by Vonnegut *et al.* [63] and the Surface Light Scattering(SLS) [64, 65, 66, 67, 68]. For the SDT method, the *EIT* is derived by geometrical considerations [69]. Considering two fluids of density ρ_1 and ρ_2, with $\rho_1 > \rho_2$, a drop of the less dense fluid is immersed in the denser fluid environment in a rotating tube. The long axis of the drop is coincident with the horizontal axis of rotation of the tube (Fig. 2.14a). A schematic section of the SDT apparatus is reported in Fig. 2.14b. The drop elongates horizontally up to centrifugal and interfacial force balance during the spinning. The shape of the drop makes the pressure difference, ΔP,

$$\Delta P = \gamma J \tag{2.103}$$

where γ is the interfacial tension and J is the interface total curvature. In cylindrical coordinates, the pressure difference and the curvature can be expressed as

$$\Delta P = P_0 - \frac{1}{2}\Delta\rho\omega^2 r^2 \tag{2.104}$$

$$J = \frac{1}{r} = \frac{d}{dr}\left(\frac{r}{1+\left(\frac{dr}{dx}\right)^2}\right) \tag{2.105}$$

where $\Delta\rho$ and P_0 are the density difference and the value of pressure at $r = 0$, respectively, and ω is the rotating frequency. Using the Vonnegut approximation [63], valid when the ratio between the horizontal drop length L and the drop diameter y_0 is bigger than 4, from the Eq. 2.104 and 2.105

$$\gamma = \frac{1}{4}y_0^3\Delta\rho\omega^2 \tag{2.106}$$

The determination of *EIT* is only related to the measurement of the drop diameter. When the Vonnegut approximation can not be met, the interfacial tension can be determined by $\gamma = \Delta\rho\omega^2/4c$, with the correction factor c obtained from a table based on measurements of the drop's half length and half-height [70]. Such a method is very sensible to temperature and cell properties because the thermodynamic equilibrium is required.

The SLS apparatus, reported in Fig. 2.14c, allows *EIT* measurements evaluating the little roughness created by thermal motion on a flat interface [69]. The mean displacement, ζ, with respect to flat equilibrium, depends on interfacial tension, according to $\zeta \propto \gamma^{-1}$, so the smaller the latter, the larger is ζ. The interfacial deformation can be expressed as a summation of Fourier components that exhibit optical behavior similar to diffraction gratings. Each scattering angle is associated with a given wave vector, q, of the Fourier decomposition. Each Fourier component resembles a capillary wave with a wavelength of $2\pi/q$. The governing wave equation encompasses restoring forces resulting from capillarity and gravity and damping forces stemming from the viscosity of the liquids. When light interacts with this dynamic grating, it experiences a frequency shift when the wave is in motion and is subject to frequency broadening under all circumstances. The light that scatters is detected using a photomultiplier and combined with light with identical

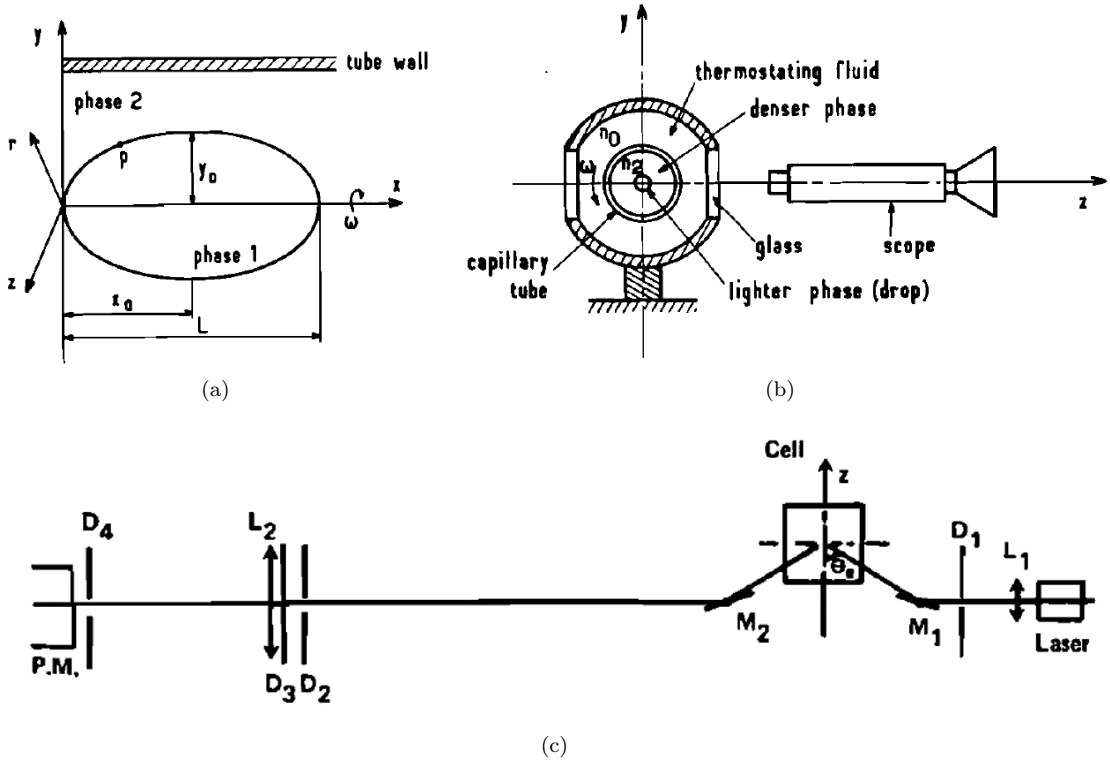

Figure 2.14. SDT and SLS Methods. a) Sketch of a rotating drop. **b)** Schematic section of SDT apparatus. **c)** Set-up sketch for SLS apparatus. Reproduced with permission from [69]. ©*Taylor & Francis, 2010.*

properties to the laser source. This additional light is generated using a diffraction grating placed near the scattering cell. Detection occurs at scattering angles that correspond to the diffraction patterns produced by the grating. By fine-tuning the contrast of the grating, heterodyne detection is achieved. The power spectrum of the photocurrent precisely mirrors the power spectrum of the thermal fluctuations occurring at the interface. The restoring force is small for low interfacial tension compared to the viscosity force. The photocurrent spectrum has a Lorentzian shape; it is centered at zero frequency and has a width related to the *EIT*,

$$\Delta\nu = \frac{\gamma q + (\rho_1 - \rho_2)g/q}{4\pi(\eta_1 + \eta_2)}) \frac{1}{1 + \frac{Nq}{2(\eta_1+\eta_2)}} \tag{2.107}$$

where ρ_1, ρ_2, η_1 and η_2 are respectively the densities and the viscosity of the two liquids, N is a surface viscosity, related to the frequency. This method has no serious disadvantages. Such as experiments were performed by studying the *EIT* between isobutyric acid and water by observing the relaxation of thermally excited capillary waves [64, 65]. In this binary mixture, there exists an upper critical temperature, denoted as T_c, below which the fluids do not mix and are immiscible. When the initial two-phase arrangement is heated beyond T_c, the fluids become miscible in all proportions. However, the interface can remain stable for hours if they are not mechanically

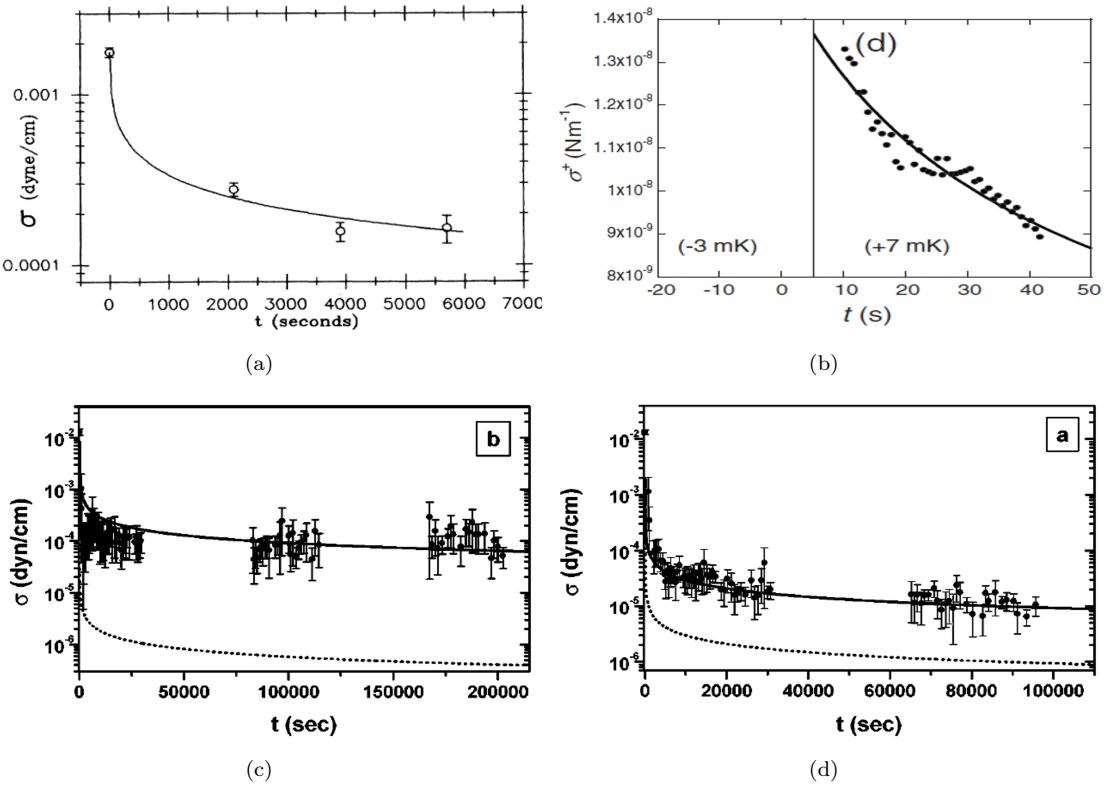

Figure 2.15. Effective Interfacial Tension measurements using the light scattering method. **a)** *EIT* averaged all over wavenumbers and temperature. The solid line is the best fitting, using the Eq. 2.108. Reproduced with permission from [65]. ©American Physical Society, 1991. **b)** *EIT* decay profile for the systems isobutyric acid/water above the T_c. Reproduced with permission from [64]. ©American Physical Society, 2010. **c)** *EIT* profile of dissolving interface for cyclohexane/methanol and **d)** for cyclohexane and deuterated methanol. Reproduced with permission from [66]. ©*American Physical Society, 1999.*

disturbed. The auto-correlation function was measured for various wave numbers, and this data was employed in conjunction with the relaxation rate of capillary waves to extract the effective interfacial tension. This allowed for the determination of the effective interfacial tension as a function of both time and temperature [65]

$$\sigma(T,t) = F(T)/[\xi_0 + (D_{eff}t)^{1/2}] \tag{2.108}$$

where $F(T)$ is constant in their range of temperature, xi_0 is the initial equilibrium correlation length at T_c, and D_{eff} is the effective diffusion constant (different from the homogeneous coefficient. As reported in Fig. 2.15a, the interfacial tension disappears slower than predicted using the diffusion coefficient in the homogeneous phase. For the same system, Lacaze *et al.* [64] reported slower *EIT*. They measured the evolution of the structure factor, L_m, of the interface, which is a quantity that describes the shape and size of the fluctuations of the surface, using Low-Angle Light Scattering.

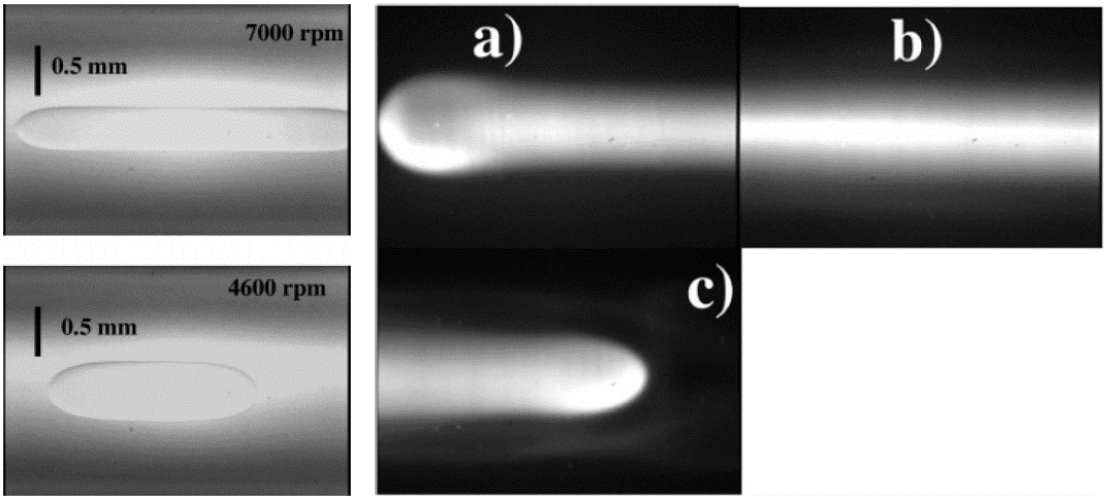

(a) (b)

Figure 2.16. Spinning-Drop Tensiometry(SDT) experimental snapshots. a) Shape of an isobutyric acid drop in a water environment under the effect of two different rotation rates. Reproduced with permission from [61]. ©American Chemical Society, 2006. **b)** Image of the left, central, and right side of a Dodecyl Acrylate drop in Poly(dodecyl acrylate). Reproduced with the permission from [58]. ©*American Chemical Society, 2007.*

It is related to the interfacial tension by

$$L_m = L_0 + b\left(\frac{\sigma(t)}{\eta}\right)(t - t_2) \tag{2.109}$$

where b is a fitting parameter, η the viscosity, t_2 is the initial time and L_0 the pattern wavelength reached at $t_2 =$. Using a local equilibrium diffusive approach, as reported in Fig. 2.15b, the fitted the *EIT* decay profile with

$$\sigma(t) = \frac{\sigma_{fit}}{\sqrt{1 + \frac{4\pi D}{l_{i,fit}}(t - t_2)}} \tag{2.110}$$

where σ is the surface tension at or above the critical point, σ_{fit} is the surface tension below T_c, D is the diffusion coefficient, and $l_{i,fit}$ is the local thickness that increases with time. Similar results were reported by Vlad *et al.* [66], with the addition of a possible role of gravity in the slowdown of diffusion, studying near-critical cyclohexane-methanol and cyclohexane-deuterated methanol systems. The latter has a density contrast much bigger than the first one. In Fig. 2.15c-d, interfacial tension profiles are reported. Because the thickness of the interface is $L = \sqrt{Dt}$, σ can be considered to be proportional to L^{-1}. Using the diffusion coefficient for the homogeneous phase, the dotted line in the figure is the interfacial tension theoretical profile. In contrast, the solid line is obtained with an effective diffusion constant smaller than the homogeneous one. The gravity effect seems to play a role in such a difference. For a short time, the process is dominated by diffusion, and for a long time, gravity could affect dissolution when the characteristic time of diffusion becomes bigger.

Isobutyric acid-water system was also studied by using the SDT [61]. Experiments were performed using both a one-phase system, quenched below the critical temperature to allow isobutyric acid drop formation and then heated up over T_c, and a two-phase system with the injection of a pure drop of acid in water, already above the critical temperature. The Vonnegut approximation is valid for such systems, and the interfacial tension can be evaluated using the Eq. 2.106. Indeed, in both cases, the dependence of y_0^{-3} from ω^2 is linear, excluding also gravitational effect. The surface tension values were in the range evaluated by May *et al.* [65], and it diminishes in time. In Fig. 2.16a, an interesting drop shape change is reported. Reducing the rotation rate, above T_c, capillary force effect can be observed, and the drop contracts, which is evidence for the *EIT* [61]. They also reported that, upon a large decrease in rotation rate, a Rayleigh-Tomotika instability could be observed, which consists of a stream of fluid breaking into smaller drops because of the interfacial tension. An unusual diffusion of the drop was also reported. The transition zone remains sharp for such a system, and the drop volume decreases with time. Interfacial thickness did not grow with $t^{1/2}$ [58], as expected from Fickian diffusion [71]. Pojman *et al.* [61] also measured the interfacial tension between 1-Butanol and water, a partially miscible system, as previously reported systems. Zoltowski obtained similar results *et al.* [58] for a monomer-polymer system formed by Dodecyl Acrylate and Poly(dodecyl acrylate). Fig. 2.16b presents images of drop at three locations along its length. The inner and outer diameters can determine the thickness of the interface. The outer diameter is the drop diameter used for measurements while the inner diameter continues to decrease, approaching the center. It was shown that the interfacial tension relaxes with increasing temperature but increases with increasing the monomer and polymer concentration. A recent study focused on the water-glycerol system revealed that when subjected to sufficiently low *Effective Interfacial Tension* values, the droplets exhibited a distinctive 'dumbbell' shape, characterized by two large lobes connected by a thin midsection, rather than the expected elliptical shapes [60]. The deformation dynamics of the droplets were effectively modeled by considering the balance of normal stresses on the droplet surface, namely the interfacial tension, the resistance of viscous shear stress against droplet deformation, and the externally applied normal stress. By fitting the model to the initial linear deformation regime, a remarkably low interfacial tension was extracted at the interface between water and glycerol, being orders of magnitude lower than reported in existing literature for the same system [72]. Notably, the ultra-low EIT values aligned closely with theoretical predictions derived from a straightforward phase field model, requiring no adjustable parameters [60].

An interesting method for evaluating the interfacial transition zone relaxation is the Laser Line Deflection(LLD), coupled to SDT [71, 73]. Concentration gradients give rise to changes in refractive indices. LLD is an optical approach that detects refractive-index variations. It offers cost advantages compared to interferometry and is less sensitive to vibrations. LLD has been applied since 1999 to investigate the diffusion of glycerol and water [74], as well as different molecular weights of

silicone oils [75]. Let's briefly outline the method: A laser sheet is directed through a sample. In cases where the laser travels through a spatially uniform medium, the light remains undisturbed. However, when the laser encounters an interface between diffusing components, it creates a concentration gradient, resulting in a refractive-index gradient. When the laser light traverses this refractive-index gradient within the sample, it is deflected at an angle roughly proportional to the gradient. For 1-butanol-water and isobutyric acid-water, a non-Fickian propagation of the transition zone boundaries was reported [73]. At the same time, the Dodecyl Acrylate-Poly(dodecyl acrylate) system relaxed as expected with a concentration-independent diffusion coefficient [71, 73]. Experiments reveal the interfacial diffusion between miscible liquids is often non-Fickian initially, transitioning to Fickian diffusion at longer times [47].

The shared conclusion is that the *Effective Interfacial Tension* between miscible fluids exists and relaxes with time until the interface is gone.

2.2.4 Hydrodynamic Instabilities

Hydrodynamic instabilities within the context of the debated existence of *Effective Interfacial Tension* between miscible fluids may serve as an indirect indicator of its presence. Miscible systems appear to be influenced by the same instabilities that affect immiscible systems, where surface tension plays a significant role as a control parameter [74]. Observations such as delayed droplet coalescence [76, 77, 78, 79], drops deformation [80, 81, 82], meniscus shape in capillary tubes [83, 84, 85, 86, 87, 88, 89, 90, 91], fingering formation (such as Saffman-Taylor instability) [92, 93, 94, 95, 96, 97, 98, 99, 100], and the occurrence of waves (Kelvin-Helmholtz instability) [28, 101, 102] offer both experimental and theoretical support for the emergence of transient interfacial tension in miscible systems due to Korteweg stresses. Various studies will be presented to establish a comprehensive background in the literature, contributing to a better understanding of the research focus, specifically the investigation of a miscible interface. Furthermore, the Saffman-Taylor instability offers an indirect means of gauging the *Effective Interfacial Tension* [103].

A falling drop in a miscible environment undergoes shape deformation. Towards the rear of the drop, a tail forms, gradually thinning. A depression appears near the rear stagnation point. Eventually, the tail separates [80]. During the fall, shear forces at the interface create a region with increasing vorticity, causing the drop edges to move upwards and take on a torus-like shape, often referred to as a mushroom shape [82]. This shape tends to expand horizontally due to radial drift, a result of the combination of vertical and angular velocities transferred by shears. The torus becomes unstable due to Rayleigh-Taylor instability, as the fluid inside is heavier than the liquid below. The drop breaks due to this instability, and the surrounding region is filled with falling matter, generating secondary drops that undergo a similar process. The droplet size exhibits multi-fractal properties, with the average dimension decreasing to a minimum before increasing, as diffusion becomes dominant. This stage occurs when each droplet volume reaches a

critical point for further splitting. The final stages are dominated by diffusion, leading to droplet mixing with the solvent [81]. The theoretical analysis, initially assuming zero interfacial tension for miscible fluids, had to consider a non-zero value to match experimental and numerical data. This suggests the existence of a small, time-dependent interfacial tension across the drop interface [80]. Comparable considerations were explored in the context of a pendant drop submerged in a miscible environment [104, 105]. A diffuse layer of material emerges at the interface between the two liquids due to diffusion across the boundary. This diffusive layer descends under the influence of gravity, forming a slender tail beneath the pendant drop, akin to the phenomenon observed in falling drops [80]. Initially, the volume of the pendant drop increases as the diffuse layer develops, leading to an outward expansion of the drop boundary. Subsequently, after reaching its maximum volume, the pendant drop experiences exponential decay over time as the drainage of the diffuse layer progresses. The exponential decay rate is intricately linked to the diffusion coefficient between the two liquids.

Sessile drops composed of the same liquid rapidly coalesce, causing the contact region's surface to level out swiftly. The connecting neck between the drops consistently fills up until the liquids completely merge, resulting in a quick coalescence [76]. Sessile drops formed with miscible liquids may exhibit delayed coalescence under specific conditions. Unlike quick merging, the main portions of the two droplets remain separate for a significant duration, often lasting several minutes, with only a shallow connection between them [79]. Such drops can display either fast or delayed coalescence, depending on the surface tension contrast. In instances of fast coalescence, the contact area between the droplets quickly evens out, resembling the kinetics of identical liquids. However, the center of gravity of the resulting drop shifts towards the droplet with the lower surface tension, indicating the presence of a Marangoni flow [77]. In cases of delayed coalescence, the connecting neck between the two droplets remains shallow, maintaining separation between their primary volumes. During this period, the droplets are in contact solely through an extremely thin film, typically just a few micrometers thick. Only after the surface tension gradient significantly diminishes do the two droplets eventually merge [77]. The distinct compositions of the droplets, particularly their different surface tensions, create a directed flow from the droplet with lower surface tension towards the one with higher surface tension. This flow generates dynamic pressure, countering the capillary pressure that typically promotes coalescence. As a result, the droplets come into contact but remain separate until the mixing flow weakens, eventually allowing the main portions of the droplets to merge into a single droplet [79]. The delayed coalescence is attributed to the presence of an interfacial tension [78]. Interfacial tension plays a crucial role also in the spreading behavior of a sessile drop within a miscible environment [104, 105]. Unlike the shape evolution observed in an immiscible setting, a sessile drop in a miscible environment exhibits unique characteristics. The drop, situated on a solid surface, develops spreading with an elevated leading edge, in addition to the contact line. Interestingly, the contact line progresses at a slower rate while the leading edge

leads to the radial advancement of the drop. The fluid flow is mainly confined to the liquid-liquid interface between the drop and its surroundings, manifesting as a draining flow that feeds into the leading edge. To investigate this phenomenon, measurements of the leading-edge radius over time were conducted using the same fluids with different viscosities. These measurements were normalized by scaling the leading-edge radial data with the initial radius of the sessile drop and time data by a characteristic drainage time, depending on the viscosity and density differences between the liquids [106, 107], finding a unified response. However, when applying the same scaling to leading-edge radial data for liquid pairs with substantially different chemical compositions, but still miscible, a unified response was not observed across the various liquid pairs. The discrepancy in scaling outcomes suggests that the difference in surface energies between each liquid pair may play a crucial role in the case of chemically different yet miscible liquid pairs, a factor not accounted for in the scaling parameter [105].

Research on capillary displacement aimed to investigate the presence of interfacial tension at the boundary between miscible fluids. In the absence of a pressure difference between the ends, the anticipated diffusion process in a horizontal tube filled with solute and in contact with the solvent at its end is simple interphase diffusion: once the interface is established, there should be no generation of flow, and the interface should remain stationary. Contrary to expectations, the observed dynamics are different [84]. Initially, the solvent displaces a small portion of solute at both ends, but once the interface enters the tube, the solute phase becomes immobilized due to a balance between gravity and capillarity. Whole interfaces with nearly constant shapes move toward the tube's center. Despite smearing over time due to mutual interphase diffusion, the speed of boundary movement far exceeds the diffusion rate. The interfacial mass transfer leads to the shrinking of the solute droplet, while the solute/solvent boundaries remain visible. The meniscus shape observed allows for an estimate of the surface tension coefficient. When the tube is positioned vertically, gravitational instability results in a non-symmetric finger flow [86], showing an unstable and sinuous interface between liquids [87]. In a gravitationally stable configuration, an axisymmetric finger of the intruding liquid forms. Under specific conditions, a spike of the more viscous liquid is observed at the tip of the main finger [87]. In experiments involving a pressure gradient, where a less viscous fluid displaces a more viscous one, the tube's orientation plays a crucial role. In a vertically placed tube with a gravitationally unstable configuration, the heavier fluid tends to penetrate downwards along the tube wall, increasing thickness around the finger. In a gravitationally stable case, the heavier fluid tends to move away from the wall layer, reducing its thickness. In a horizontal tube, gravity tends to move the main body of the lighter finger towards the upper part of the tube, potentially leading to gravitational instability that cuts the finger into two longitudinal parts. The comparison of immiscible [108] and miscible experiments allow for the determination of an effective surface tension [83]. Such dynamics were numerically verified [62, 89]. Experiments with the same fluids of different viscosities demonstrated that molecular structure

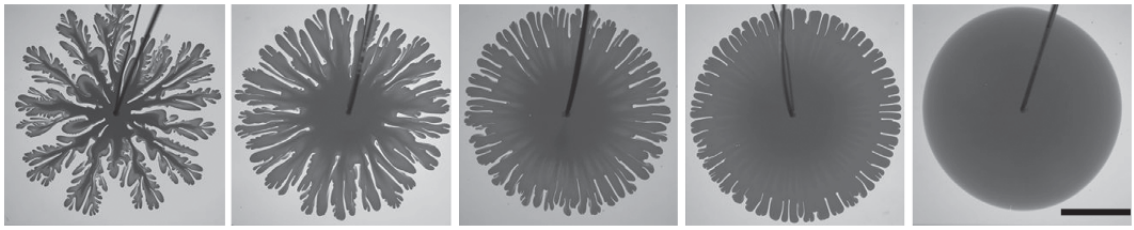

Figure 2.17. Saffman-Taylor instability. Viscous fingering pattern for decreasing (from left to right) viscosity ratio, η_{in}/η_{out}. Reproduced with permission from [93]. ©*Springer Nature Limited, 2014.*

has a minimal influence on the fingering displacement behavior [85]. Additionally, miscible molten silicates forming a meniscus suggested the presence of interfacial tension [109]. The impact of Korteweg stresses, along with the associated vorticity and stream-function fields they induce, was evaluated in the context of net flow displacements within horizontal capillary tubes and density-driven instabilities in vertical tubes [88]. In both scenarios, the presence of Korteweg stresses led to the development of a vortex ring-like structure near the concentration front's tip. Notably, due to the negative nature of the Korteweg stress coefficient [110], the vortex ring within the horizontal tube serves as a decelerating force for the advancing front. This observation suggests that the described meniscus behavior can be influenced by this phenomenon. Similarly, within the vertical tube, the Korteweg stresses slow down the rise of bubbles and fingers formed due to the unstable density stratification.

Injecting co-current and concentric streams of miscible fluids with equal density but different viscosities into a cylindrical pipe revealed two distinct and unstable axisymmetric patterns: mushrooms and pearls [90]. These patterns were observed due to viscosity perturbations. Interestingly, the necessity of a high viscosity ratio for absolute instability mirrors the conditions observed in immiscible flows [91].

The primary focus of this literature analysis revolves around the examination of finger-related phenomena, such as the Saffman-Taylor instability, and wave formation, particularly the Oscillatory Kelvin-Helmholtz instability. These two instabilities will be juxtaposed with a novel destabilization scenario that is presented in the current study.

Viscous fingering, also recognized as the Saffman–Taylor instability, is a hydrodynamic phenomenon observed when a less viscous fluid displaces a more viscous one in porous media or within Hele-Shaw flows, referring to Stokes flows occurring between two parallel flat plates with a narrow gap between them [111].

In systems under study, the dominance of advection over diffusion typically results in well-defined interfaces that separate fluids. Miscible fluids exhibit a branching fractal pattern resembling ramified fingers [93], as depicted in the leftmost image in Fig. 2.17. However, as the viscosity ratio increases, an inner circle devoid of fingers, composed solely of the invading fluid, emerges and systematically expands (Fig. 2.17, from left to right). At high viscosity ratios, this inner circle

encompasses the entire pattern, suppressing the instability entirely (rightmost image in Fig. 2.17. The viscosity ratio not only influences the rate of pattern growth but also dictates its fundamental nature. By manipulating this single parameter, the system undergoes a transition from fractal growth, characterized by growth exclusively at the pattern's edge, to proportionate growth, where multiple length scales all exhibit uniform growth rates while preserving the overall shape. The classic Saffman-Taylor theory posits that the most unstable wavelength

$$\lambda_c = \pi b \sqrt{\frac{\sigma}{\Delta\eta V}} \tag{2.111}$$

is determined by the competition between interfacial tension, σ and interfacial stresses, dependent on interfacial velocity V and viscosity differences $\Delta\eta$ [112]. In the limit of zero interfacial tension, a fractal structure is expected to form, with a minimal most-unstable wavelength. Experimental observations deviate from this expectation, revealing the emergence of diverse large-scale structures. The large-scale aspects of these patterns are dictated by the viscosity ratio between the two liquids and remain independent of the most unstable wavelength, which governs local instability at the interface. Particularly noteworthy is the existence of a completely stable displacement regime at high viscosity ratios, indicating that, in miscible fluids, inertia prevails over interfacial tension due to their small size. This effect of viscosity contrast is not observed in immiscible systems.

A comparison between miscible and immiscible viscous fingering reveals insights into the influence of interfacial tension on the fingering patterns [95]. Figure 2.18 illustrates the fingering phenomena for both cases, showcasing a decrease in flow rate from left to right. In the case of miscible fingers (top images), the global fractal structure remains relatively consistent across different flow rates. The fingers exhibit chaotic growth in the Hele-Shaw cell through a finger-splitting mechanism. Despite variations in flow rate, the overall fractal pattern of miscible fingers does not show significant changes. Conversely, the impact of flow rate on immiscible fingers is more pronounced. The bottom images indicate that, as the flow rate increases, the fingers become narrower, and side branching becomes more prominent. Unlike miscible fingers, immiscible fingers display a more dramatic response to changes in flow rate. Moreover, the absence of a fractal structure is observed in the case of high surface tension (immiscible systems), which stabilizes short-wave destabilization [112].

To explore the early stages of radial viscous fingering, a perturbation theory was employed [92]. According to the principle of minimum entropy production, the initial radial viscous fingering between miscible fluids should feature a cut-off wavelength that remains independent of both the injection rate and the viscosity contrast. Recent work reported that this theory effectively captures the behavior observed in molecular Newtonian liquids when a rapid interdiffusion tends to blur concentration profiles, rendering capillary forces negligible [93]. However, when interfacial stresses cannot be neglected, the wavelength associated with the onset of radial viscous fingering becomes

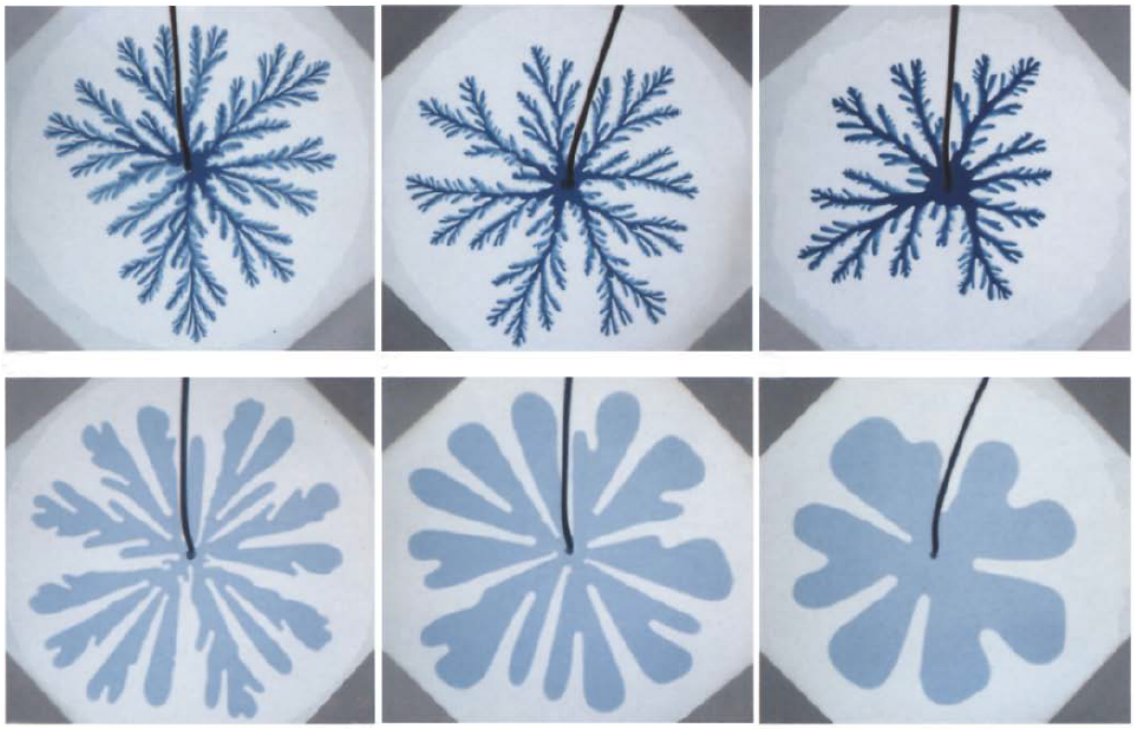

Figure 2.18. Miscible-immiscible viscous fingering comparison. The flow rate of the inner fluid decreases from left to right. **a)** Miscible fingering shows fractal structures due to a splitting mechanism. **b)** Immiscible fingering. The fractal structures are stabilized by higher interfacial tension. Reproduced with permission from [95]. ©*Springer-Verlag, 1987.*

dependent on both the injection rate and, notably, the physicochemical properties of the fluids in contact [103]. These results were obtained through experiments involving colloidal suspensions in contact with their own solvents, where interdiffusion can be neglected on the time scale of the experiments. The presence of an effective interfacial tension provides a satisfactory explanation for the observed phenomena [99]. The dependence of the observed number of fingers on injection rate aligns with predictions for a finite (positive) interfacial tension [103]. Further insights were gained by investigating suspensions across a broad range of volume fractions. The interfacial tension was found to be proportional to the square of the volume fraction, consistent with Korteweg's theory for miscible fluids [113].

Surface tension plays a crucial role in the dynamics of the Saffman-Taylor instability, and with its finiteness and positiveness serves as a key parameter governing the system. However, deviations from the typical Saffman-Taylor mechanism can arise due to gradients in surface tension, anyway leading to the formation of fingers. For instance, in a microscale hele-shaw cell, where no external pressure gradients are applied, the diffusion-initiated interfacial dynamics between heptane and viscous crude oil exhibit a two-stage dispersive mechanism. In the first stage, spontaneous fractal-like fingering occurs as a result of the preferential extraction of light components from the crude oil by heptane. This creates a distinct interface between the two phases. In the second stage, diffusive mixing between heptane and the heavy components of the crude oil takes place.

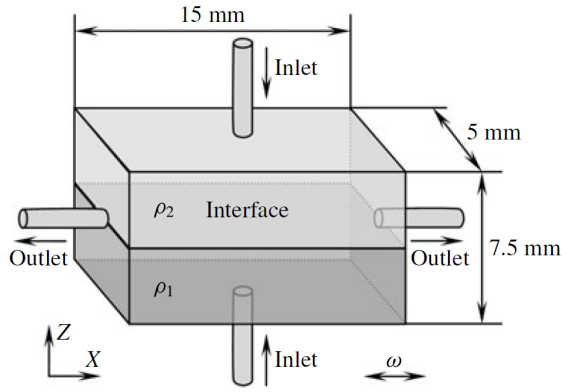

Figure 2.19. Oscillatory Kelvin-Helmholtz instability. Experimental arrangement for creating a sharp interface between miscible fluids. Reproduced with permission from [101]. ©*Royal Society of Chemistry, 2015.*

Dynamic interfacial tension gradients induced by compositional gradients lead to convection cells at the finger tips, driving self-similar fractal-like finger splitting [97]. Another example involves the spreading of a sessile drop of aqueous surfactant solution on a glass surface moistened with a thin layer of miscible liquid (water) [100]. This system exhibits surface tension-induced instability, characterized by spreading fingers. The velocity and shape of these fingers depend on the ambient water layer's thickness and surfactant concentration. Unlike the Saffman-Taylor instability, the Marangoni effect, driven by gradients in surface tension, governs this instability. Increasing surfactant concentration suppresses the instability. Additionally, the wavelength in the electrohydrodynamic instability between miscible fluids of different conductivities is explained by a transient interfacial tension [114].

Miscible systems, similar to immiscible ones, can also experience waves formation at a sheared interface through a Kelvin-Helmholtz-like mechanism. When horizontal vibrations are applied to a cell containing two superimposed miscible liquids, a horizontal pressure gradient is generated, leading to oscillatory shear flows. Interestingly, the waves formed in this scenario remain, on average, in the same place due to the harmonic change in the flow direction, effectively freezing the wave profile in the reference frame of the vibrating container. As for the case of the classic Kelvin–Helmholtz instability without surface tension, the critical wavelength that initially emerges is zero (for zero surface tension). This issue renders the problem Hadamard ill-posed and inconsistent with experimental observations. The only documented vibrational experiments involved water and glycerol [102] and mixtures of water and isopropanol [101]. In both instances, finite unstable standing waves were observed at a critical velocity amplitude. To address these challenges, an injection system (depicted in Fig. 2.19) was developed, allowing for the creation of a sharp interface between two miscible liquids [101]. The layers have equal thickness, and both liquids are simultaneously injected into the cell using two identical syringe pumps—one through the orifice at the bottom for the denser fluid and the other through the orifice at the top for the lighter fluid. Excess fluid exits the cell through orifices in the side walls. The cell is refilled with fluids between

Figure 2.20. Oscillatory Kelvin-Helmholtz instability. The development of the frozen wave instability between miscible liquids under horizontal vibration. Reproduced with permission from [101]. ©*Royal Society of Chemistry, 2015.*

each test to maintain a thin, straight interface between the two miscible fluids in the X–Y plane. Experiments conducted with these systems, subjected to horizontal vibrations, reveal the existence of frozen wave instability between two ordinary miscible liquids with similar (though not identical) densities and viscosities. As the oscillatory forcing increases, the amplitudes of the interface perturbations steadily grow, forming a distinctive saw-tooth frozen structure [28, 101], as depicted by the spatio-temporal evolution of the destabilization scenario reported in Fig. 2.20. The distinction between immiscible and miscible fluids is exemplified by the frozen wave shapes. Triangular waves are attributed to the absence of interfacial tensions and negligible viscous effects in miscible fluids, while immiscible fluids exhibit sinusoidal frozen waves. Despite the notion that the oscillatory Kelvin–Helmholtz instability standing waves are ostensibly unaffected by the viscous component of the stress tensor, experiments with a water/glycerol system reported sinusoidal wave shapes, contrary to expectations [102]. This unexpected outcome was rationalized by proposing that the frozen waves are slightly in motion, preventing the complete dismissal of viscous effects. Viscous stresses, in turn, tend to stabilize short wavelengths, resulting in smoother disturbances and the observation of sinusoidal waves. Regardless of the wave shape, the onset of interfacial instability in miscible liquids occurs beyond a well-defined threshold. Increasing the oscillatory speed above the critical value leads to a continuous growth in the amplitude of the perturbation. Comparisons with theoretical predictions [27] for immiscible liquids reveal that the inviscid model significantly underestimates the instability threshold. However, at high frequencies and vanishing amplitude, experiments and inviscid theory show reasonable agreement [28]. Another distinction from instability in immiscible fluids is that, in miscible fluids, the driving force—the density gradient across the contact line—diminishes with time due to convective mixing and diffusion. As a result, the flow dynamics in miscible fluids are inherently transient. Numerical investigations were conducted [28]. To reconcile these findings, Cahn–Hilliard–Navier–Stokes equations were employed, assuming a small non-zero interfacial tension between the fluids [28]. This assumption, though debated, proves crucial in the context of hydrodynamic instabilities, underscoring its controlling role in the stability analysis of miscible interfaces.

2.3 Thin Film Drainage

2.3.1 Bubble-Solid Interaction and Thin Film Drainage

In the context of a stationary bubble within an infinite liquid medium, the density contrast between the bubble and the surrounding liquid induces a constant buoyancy force, prompting the bubble to ascend. The upward movement continues until the emergent drag force matches the buoyancy force. Throughout this acceleration phase, the drag force takes some time to establish itself, leading to a historical force, commonly known as the Basset force [115]. It is noteworthy that the consideration of the Basset force depends on whether the bubble surface is deemed immobile; this factor can be disregarded when the surface is regarded as mobile [115]. Moreover, as the bubble undergoes acceleration, the surrounding liquid must also accelerate, giving rise to an additional force known as added mass force. Upon colliding with a horizontal solid surface, a thin liquid film forms between the bubble and the surface. This film exhibits a non-uniform thickness, adopting an axisymmetric dimpled shape, with the maximum thickness occurring at the axis of symmetry. The minimum thickness, referred to as the film radius or radial film size, is also part of this dynamic. During the collision, an increase in pressure within the thin liquid film results in a film force acting on the bubble. In scenarios where the film between the bubble and the surface is extremely thin, surface forces become significant due to Van der Waals and electrical double-layer interactions. Generally, these surface forces become relevant when the film thickness is 100 nm or less [116]. In cases where the Reynolds number is less than 1, achieving such film thicknesses is common, and the associated forces play a crucial role [117]. However, in dynamic scenarios with a Reynolds number much greater than 1, such as during bubble collisions with a solid interface, the film thickness typically reduces to the order of microns. Consequently, these surface forces are commonly disregarded in such situations [115, 118]. If, during the impact, the film fails to reach its critical rupture thickness, the bubble rebounds from the surface. This collision-rebound cycle persists until the film ruptures or the bubble dissipates all its kinetic energy. Various factors influence collisions, such as liquid properties, bubble size, and impact velocity [119]. Surface roughness and hydrophobicity also play a role in the collision dynamics [120, 121, 122]. The rupture of the film between the bubble and surface leads to three-phase contact formation, and the characteristics of the film drainage are crucial for determining the impact outcome [121]. Extensive research has focused on understanding the drainage and rupture of thin liquid films trapped between a bubble and a solid surface [115, 120, 121, 122, 123]. The drainage rate of these thin liquid films depends on several variables, including bubble size, impact velocity [119, 120, 124], liquid viscosity [125], surfactants [120, 123, 126], and radial film size [127, 128]. The theoretical foundation for describing fluid flow in thin films dates back to Reynolds, who first studied it, resulting in the development of lubrication equations that are still in use today [129]. The interaction between dynamic bubbles and solid surfaces has been explored in a study that specifically examined the influence of surface

roughness [118]. The research revealed that at high surface roughness values (50 μm, the bouncing cycle of bubbles is hindered, leading to immediate bubble attachment, while lower roughness values < 1 μm promote more bouncing cycles. Two main reasons were identified for this phenomenon: (i) higher roughness corresponds to taller surface asperities, increasing the probability of the thin liquid film reaching its critical rupture thickness sooner, and (ii) rougher surfaces with larger cavities contain more gas, facilitating quicker bubble attachment. Furthermore, an analysis of the collision process was conducted based on kinetic energy, specifically impact velocity [128]. The findings indicated that an increase in kinetic energy resulted in a greater number of bouncing cycles before film rupture. The hypothesis suggested that this outcome is linked to the radial size of the film formed during the impact. Higher energy collisions lead to the formation of a larger film radius due to increased bubble deformation. The larger film radius is associated with a slower drainage rate, as indicated by the inverse relationship between the film drainage rate and film radius. Consequently, the larger film radius prolongs the time necessary to reach a critical rupture thickness. The impact of surface-active substances attached to the bubble surface has been explored in previous studies [120, 121]. As the bubble ascends, these substances create a non-uniform distribution over its surface, leading to a surface tension gradient that immobilizes the bubble. This immobilization increases the drag force on the rising bubble, causing a considerable reduction in its terminal velocity. Additionally, these substances play a crucial role in the film drainage during a bubble's collision with a solid surface. At low concentrations, the bubble surface behaves similarly to the stagnant cap model [130], where the top of the bubble is mobile, and the bottom is immobile. This reduces the bubble impact velocity without affecting the film drainage rate. The decreased impact velocity results in fewer bouncing cycles before film rupture, primarily due to the radial film size considerations. On the other hand, at higher concentrations, the entire bubble surface becomes immobile. Consequently, the film drainage rate slows down significantly, prolonging the time required to reach the critical rupture thickness.

Numerical models have been developed to accurately predict the trajectory and velocity profiles of bubbles during collisions, considering both clean and contaminated scenarios [131, 132]. These models employ point force analysis to determine the bubble's equation of motion, coupled with the Stokes-Reynolds-Young-Laplace equations for predicting film drainage. The challenge of measuring film thickness variation during bubble collisions is addressed by utilizing interferometry, allowing for the experimental observation of spatio-temporal evolution in film thickness [118]. Remarkably, these experimental measurements align with predictions derived from the numerical models. Subsequent studies using interferometry explore the impact of bubble surface mobility on the drainage process [133]. The impact of surface viscoelasticity on the drainage of a thin film between two fluid particles undergoing gentle collision was examined [134].

After the bouncing process, a bubble comes to rest on a horizontal solid surface and a dimple-shaped film is formed, initiating a subsequent drainage process. Extensive research has been

conducted to comprehend the dynamics of this drainage and film rupturing. The drainage process is influenced by various parameters and conditions, including hydrodynamic boundary conditions, interaction forces between interfaces, and the impact velocity of the bubble [118, 119, 135, 136]. Additionally, film drainage is contingent on variables such as bubble size [128, 127], liquid viscosity [125], the presence of surface-active molecules or impurities, and dissolved gases, among others [123, 126, 137, 138, 139]. The drainage behavior of thin films can be described using the Stokes-Reynolds-Young-Laplace equations [136, 140, 141], and a scaling analysis for resolution is presented in Section 2.3.2. Fisher *et al.* successfully showed and measured the drainage of aqueous films between a bubble and a hydrophilic quartz plate for the first time [142, 143, 144]. Recently, the wetting film profile was successfully predicted by exploring the Stoke-Reynolds-Young-Laplace model with the assumption of tangential immobile and no-slip boundary conditions at the bubble and quartz surfaces, respectively [136]. When elastic forces are introduced at the interface, it leads to a delayed viscous response. This delay causes the interface to exhibit inviscid behavior (mobile interface) for a specific duration before returning to Newtonian behavior. This marks a transition from mobile to immobile behavior. The length of this delay is directly proportional to the surface Weissenberg number, while the initiation of deviation from inviscid behavior is determined by surface viscous forces. Furthermore, this delay signifies a time-dependent alteration in the tangential mobility of the interface during drainage. In this context, inviscid and Newtonian interfaces represent the most and least mobile states, respectively. The presence of physical impurities and absorbing-non-absorbing particles strongly influence the bubble-solid interaction, and thus, the film drainage becomes much more complex to understand. Surprisingly, there has been no prior investigation into the impact of micro-particles, adsorbed on bubble surface, on the stability and drainage time of the thin film.

A brief review of polystyrene microparticles behavior at the interface during particle-bubble interactions is presented to enhance the comprehension of the reported findings. Colloidal particles act like surfactant molecules, being adsorbed to a fluid-fluid interface. At low PS particle concentrations, the surface tension is not significantly reduced [145]. When adsorbed to a fluid-fluid interface, PS particles can form highly ordered structures even at low surface coverage [146, 147, 148]. Depending on surface pressure (i.e. coverage), PS interfacial structures could show surface elasticity, due to electrostatic interactions between particles (low coverage - low elasticity) or due to strong hydrophobic attraction (high coverage - high elasticity) [134].

2.3.2 Stokes-Reynolds-Young-Laplace Equations

The drainage of a film formed between a solid and a liquid/air interface can be modeled in the framework of the augmented Young-Laplace equation. In the lubrication approximation, the equation balances out the capillary pressure due to the local curvature, ζ, of the liquid/air interface of surface tensionγ, the disjoining pressure Π and the viscous shear stress in the liquid film of

viscosity η and velocity field $v_r(z)$, oriented in the radial direction and varying with z.

$$\frac{\partial}{\partial r}(\gamma\zeta - \Pi) = \eta\frac{\partial^2 v_r}{\partial z^2} \tag{2.112}$$

The equation 2.112 distinguishes three regimes contingent on the interplay between the capillary term and the disjoining pressure term: a capillary regime, a disjoining pressure-dominated regime, and a mixed capillary/disjoining pressure regime. In cylindrical geometry, the Eq. 2.112 can be written as a function of the film thickness and its derivative. Assuming the lubrication approximation, the radial velocity has a parabolic profile. The velocity vanishes at the solid interface, $z = 0$. The velocity profile

$$v_r = \frac{6q}{3\beta - 2}\frac{z(\beta h - z)}{h^3} \tag{2.113}$$

where q is the radial flux for unit of perimeter and β is a parameter related to a boundary condition at the liquid/air interface: If the tangential stress vanishes at this interface, $\beta = 2$, defining a mobile interface; if the tangential velocity cancels, $\beta = 1$, defining an immobile interface. Combining the Eq. 2.112 with the velocity profile 2.113

$$\frac{\partial P}{\partial r} = -\eta\frac{12q}{(3\beta - 2)h^3} \tag{2.114}$$

The pressure can be written as the sum of the Young-Laplace pressure, disjoining pressure, and capillary pressure depending on local film curvature $\zeta(h)$

$$P = P_{ext} + 2\gamma R^{-1} - \gamma\left(\frac{\partial^2 h}{\partial r^2} + \frac{1}{r}\frac{\partial h}{\partial r}\right) - \Pi \tag{2.115}$$

where h is the film thickness. The flux q depends on radial coordinates by the volume conservation equation

$$\frac{\partial rq}{\partial r} = -r\frac{\partial h}{\partial t} \tag{2.116}$$

The combination of Eqs. 2.114, 2.115 and 2.116 give the governing equation for the space and time variations of the film thickness

$$\frac{\partial P}{\partial r} = \frac{\partial}{\partial r}\left(-\gamma\left(\frac{\partial^2 h}{\partial r^2} + \frac{1}{r}\frac{\partial h}{\partial r}\right) - \Pi(h)\right) = \frac{-12q\eta}{(3\beta - 2)}\frac{1}{h^3} \tag{2.117}$$

The main features of dimple relaxation were captured through scaling analysis.

Herein only the mixed regime is considered in which the dimple thickness is controlled by capillary pressure, while the equilibrium thickness at the barrier ring is set by disjoining pressure when it is equal to the Young-Laplace pressure in the drop. At the barrier ring, the height h has a minimum and, expanding in term of $r - r_d$, the shape of the barrier ring for r approaching to r_d

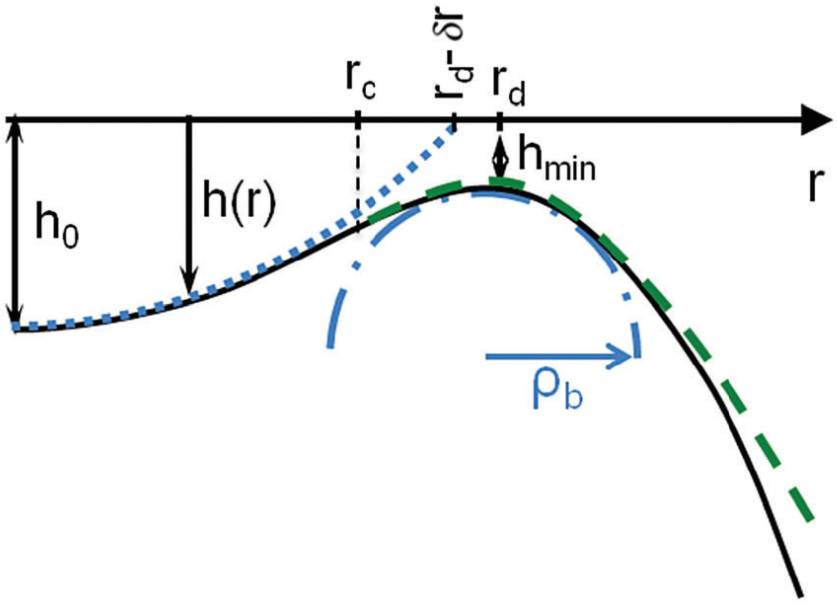

Figure 2.21. Scaling Analysis. Geometrical parameters characterizing the radial film thickness. Reproduced with permission from [149]. ©*The Royal Society of Chemistry, 2017.*

$$h_b(r) \simeq h_{min} + \frac{(r-r_d)^2}{2\rho_b} + \frac{(r-r_d)^3}{6G^2} \tag{2.118}$$

At the center, the dimple shape is approximately parabolic

$$h_d(r) \simeq h_0 \left(1 - \frac{r^2}{(r_d - \delta r)^2}\right) \tag{2.119}$$

where $(r_d - \delta r$, defined in Fig. 2.21, determines the radius for which the parabolic shape is null. To connect the center and the barrier ring, at $r = r_c$, the height h as well as its first and second derivatives are continuous. In the limit of $\delta r << r_d$ and $h_0 << r_D$, the following geometrical relationships

$$G \simeq 2\rho_b \sqrt{\frac{h_0}{r_d}} \tag{2.120}$$

is a parameter related to the barrier ring asymmetry,

$$\rho_b = \frac{3}{8}\frac{h_{min} r_d^2}{h_0^2} \tag{2.121}$$

is the radius of curvature at the barrier ring,

$$r_d - r_c \simeq \frac{G^2}{\rho_b} \simeq \frac{3}{2}\frac{h_{min} r_d}{h_0} \tag{2.122}$$

Additionally, assuming the dimple shape remains parabolic and the radius at the barrier ring is constant, the flux can be estimated by

$$q_b \simeq -\frac{r_d}{4}\frac{\partial h_0}{\partial t} \tag{2.123}$$

In the mixed regime, the barrier ring height has its asymptotic value, set by disjoining pressure. On the other hand, the film drainage is capillary-driven. The capillary term $\gamma\frac{\partial^3 h}{\partial r^3}$ provides a zero-order term in $r - r_d$ to the pressure gradient. The disjoining pressure gradient is $\frac{\partial \Pi}{\partial r} = \frac{d\Pi}{dh}\frac{\partial h}{\partial r}$. As the barrier ring corresponds to a minimum in thickness profile, the Eq. 2.118 has no first-order term, and the disjoining pressure gradient is, therefore, a higher order term in $r - r_d$. So, the disjoining pressure gradient across the barrier ring is negligible compared to the capillary pressure gradient. Additionally, the Young-Laplace pressure experimentally dominates on capillary pressure gradient. Such as the pressure gradient across the barrier ring of length $r_d - r_c$ is $2\gamma R^{-1}(r_d - r_c)^-1$. From the Eq. 2.114

$$\frac{2\gamma}{R(r_d - r_c)} = \eta\frac{12q_b}{(3\beta - 2)h_{eq}^3} \tag{2.124}$$

Explicating the flux from Eq. 2.123

$$\frac{\partial h_d}{\partial t} = -\frac{4}{9}(3\beta - 2)\frac{\gamma h_{eq}^2}{\eta r_{film}^2}h_d \tag{2.125}$$

so

$$h_d = h_{d,0}exp\left(-\frac{4}{9}\frac{\gamma h_{eq}^2}{\eta r_{film}^2}(3\beta - 2)t\right) \tag{2.126}$$

where $h_{d,0}$ is the initial dimple height. The relaxation of the dimple center is exponential [149].

The presented analysis was employed to fit the experimental data, confirming the transition in the behavior of the liquid/air interface from immobile to mobile (see Section 4.2.2).

Materials and Methods

3.1 Hydrodynamic Fingers Instability

In this chapter, comprehensive details regarding the system configurations (Section 3.1.1) and setup employed, regarding miscible interfaces, are presented. The pendant drop and contact angle setups closely align with those documented in the literature, with the sole modification being the custom-designed chamber for forming pendant/sessile drops, enabling the measurement for two liquids systems. The chamber was crafted using a 3D printer for the specific application in this study (Section 3.1.2).

The noteworthy innovation lies in the setups utilized to induce motion and perturb the miscible interface between PDMS and acetone (Sections 3.1.3, 3.1.4). The experimental configurations are intended to enable the investigation of the interface between two fluids in complex flow conditions. These setups comprise a stepper motor to drive the movement, a glass container in which the system is placed, and a top integrated camera (or positioned laterally based on the experimental requirements). The entire arrangement was designed, encompassing the control of the stepper motor to impose motion (Section 3.1.5). The integration of the glass container onto the stepper motor, the housing for the integrated camera, and the resolution of issues related to weight distribution and vibrations were achieved through the development of custom components designed entirely from scratch and fabricated using 3D printing technology. The CADs for each component are detailed and provided in the Appendix A.3.

To analyze experimental snapshots, an in-house custom MATLAB® code was employed (Section 3.1.6).

3.1.1 Materials

Figure 3.1 illustrates the system's configuration, where the two fluids are layered in a glass container. The bottom layer consists of Polydimethylsiloxane (PDMS), with its diameter potentially matching or smaller than the container's diameter (depending on the experiment's purpose). The upper layer consists of Acetone, which may share either one horizontal flat interface with

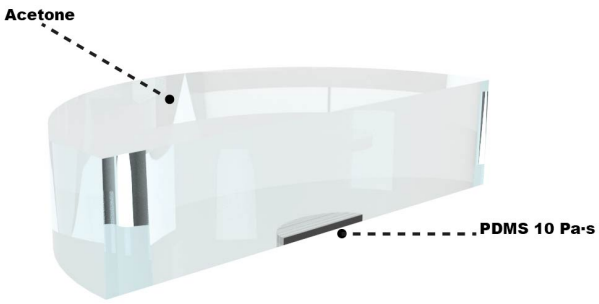

Figure 3.1. System 3D sketch. The system under investigation consists of two layers of fluids. The lower layer is composed of PDMS ($\mu = 10\ Pa \cdot s$), while the upper layer consists of Acetone. In experiments studying hydrodynamic finger instability, the PDMS does not completely cover the glass substrate, allowing the acetone to fill the remaining volume and cover it entirely.

PDMS if it covers the entire substrate or a curved interface if the PDMS layer does not span the entire substrate and Acetone fills the remaining volume. The experimental campaign utilizes Polydimethylsiloxane (PDMS) with CAS No. 63148-62-9 (PSF - 10,000cSt Silicone Fluids) from ClearCo Products Co, Inc. and Acetone from Carlo Erba Reagentes SAS with CAS No. 67-64-1. To enhance the visualization of the PDMS layer, the polymer was blended with 1% in volume of Black (red and blue) Dye BRAVO Luxens. The addition of dye did not affect the viscosity of PDMS. The viscosity of the fluids is $\mu_{PDMS} = 10\ Pa \cdot s$ and $\mu_{Ac} = 3 \cdot 10^{-3}\ Pa \cdot s$, while their densities are $\rho_{PDMS} = 970\ kg/m^3$ and $\rho_{Ac} = 780\ kg/m^3$. In literature, a diffusion coefficient for acetone in crosslinked PDMS is documented to vary from 10^{-6} to 10^{-7} $[cm^2/s]$. Considering $D \sim\ 10^{-7}\ cm^2/s$ as a reference parameter is appropriate, as high-viscosity PDMS is used here and the study indicates that this value was measured within a swollen silicon matrix [150]. For the experiments whose results are reported in Sections 4.1.4, 4.1.5 and 4.1.6, the estimated diffusion time $t_D = h^2/D$ is approximately 7 hours, where $h \sim 2$ $[mm]$ represents the initial height of the PDMS layer after deposition. The experiments were performed at ambient temperature.

These specific fluids were chosen due to their significant viscosity contrast and miscibility. The choice facilitates the formation of hydrodynamic instability under investigation, having a slow diffusion between them. This ensures a lasting interface between them throughout the experiment.

3.1.2 *EIT* and Contact Angles

Pendant drop tensiometry provides a straightforward and elegant method for determining the *Effective Interfacial Tension*, a crucial parameter in the hydrodynamic instability described herein. The technique involves capturing the silhouette of an axisymmetric fluid droplet and iteratively fitting the Young–Laplace equation. This equation balances the gravitational deformation of the drop

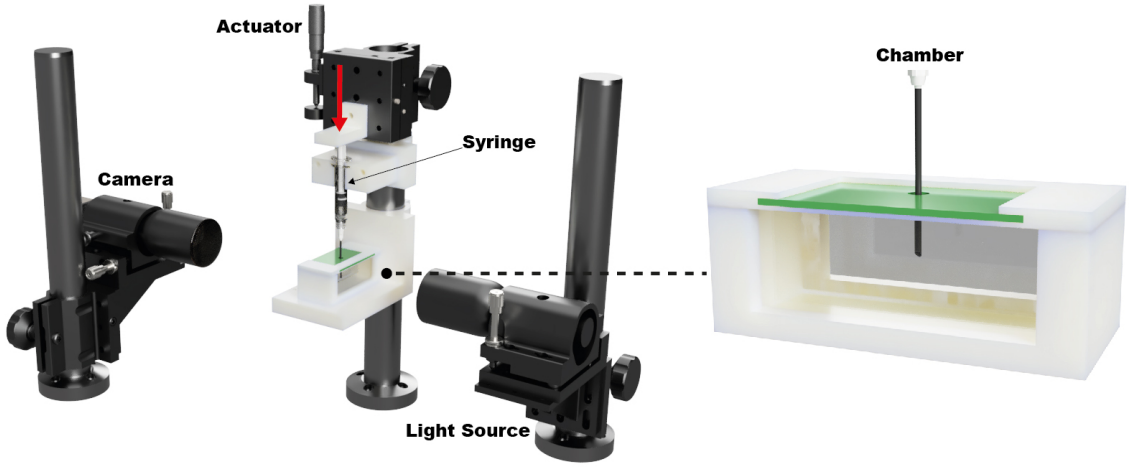

Figure 3.2. Pendant and Sessile Drop Method set-up. *[left]* 3D illustration of the experimental set-up. *[right]* Computer-Aided Design (CAD) of the chamber employed for the *Effective Interfacial Tension* and contact angle measurements.

with the restorative interfacial tension. Despite its apparent simplicity, pendant drop tensiometry comes with complications and limitations related to both the Bond number (which represents the equilibrium between interfacial tension and gravitational forces) and the volume of the droplet.

The equipment needed for pendant drop tensiometry is remarkably simple, consisting mainly of a needle, a camera, and a light source. The left image in Figure 3.2 illustrates the experimental arrangement. The chamber holder, the syringe holder, and the pushing system (white components in the set-up) were designed using Autodesk® Fusion 360™and 3D printed, using Original Prusa i3 MK3S+ printer, in Polylactic Acid (PLA). In the experiment, a vertical actuator was employed to push the piston of a syringe, facilitating the formation of droplets. The PDMS drop was generated within an acetone environment using a custom chamber, with a volume of 24 ml, as depicted in the right image in Figure 3.2. The chamber was designed using Autodesk® Fusion 360™and subsequently 3D printed, using Original Prusa i3 MK3S+ printer, in PLA. Transparent glass walls were incorporated into the design to facilitate the visualization of the drop while safeguarding the PLA walls from the effects of acetone exposure. A green cap, made of polypropylene (PP), with a hole to allow the entry of a needle into the chamber and to avoid acetone evaporation, was utilized. The drop was generated using a 17-gauge stainless steel needle with a flat tip ($1.067\ mm\ I.D., 1.473\ mm\ O.D.$). The images were captured using ThorLabs sCMOS Camera equipped with a telecentric lens (Edmund 2x TML Silver). Ensuring precise determination of interfacial tension requires careful consideration of several factors in the experimental setup despite its apparent simplicity. A diffused light source was used to prevent optical aberrations at the drop periphery and avoid reflections from other sources, such as overhead lighting, on the drop interface. Additionally, avoiding lensing effects that could distort the drop image on the digital camera sensor is crucial, and achieving a homogeneous background in the image is essential for simplifying

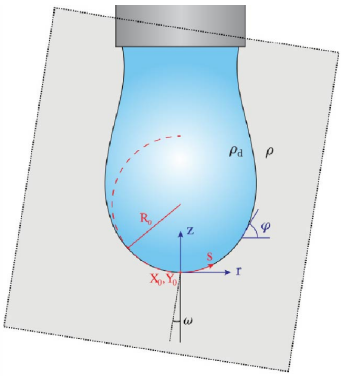

Figure 3.3. Pendant Drop schematic illustration. A schematic of a pendant drop below a needle. The shaded area indicates the portion captured by the camera, which may not be perfectly aligned with the drop. Annotations identify variables employed in the computational process for calculating the Bond number and, consequently, the interfacial tension. Reproduced with permission from [151]. ©*Elsivier Inc., 2015.*

the analysis process. Another concern is droplet oscillation induced by external vibrations and air currents. An anti-vibration table minimizes the impact of external vibrations. In liquid-liquid systems investigated in this study, the inertial damping effect of the continuous liquid phase makes vibrations less problematic when measuring interfacial tensions.

The equilibrium state of a pendant drop, reported in Fig. 3.3, conforms to the Young–Laplace equation. This equation establishes a connection between the Laplace pressure acting across an interface, the curvature of the interface, and the interfacial tension

$$\gamma\left(\frac{1}{R_1}+\frac{1}{R_2}\right)=\Delta P=\Delta P_0-\Delta\rho g z \tag{3.1}$$

where γ is the interfacial tension, R_1 and R_2 are the principal radii of curvature; the Laplace pressure across the interface, $\Delta P = P_{in} - P_{out}$, can be expressed in terms of reference pressure ΔP_0 at $z = 0$ and a hydrostatic pressure $\Delta\rho g z$, where $\Delta\rho$ is the difference between the drop and continuous densities. By taking advantage of axisymmetry and scaling the quantities by R_0, the radius of curvature at the drop apex, the Eq. 3.1 can be expressed in cylindrical coordinates (r, z) in terms of the arc length s from the drop apex

$$\frac{d\phi}{ds}=2-Bo\ z-\frac{sin\ \phi}{r};\ \frac{dr}{ds}=cos\ \phi;\ \frac{dz}{ds}=sin\ \phi \tag{3.2}$$

with boundary conditions

$$r=0;\ z=0;\ \phi=0;\ s=0; \tag{3.3}$$

The shape of the pendant drop is contingent upon a singular dimensionless parameter known as the Bond number, denoted as $Bo = \Delta\rho g R_0^2/\gamma$. An absolute vertical alignment of the needle parallel to gravity is essential to ensuring droplet axisymmetry. The Bond number suggests having

an adequately sized droplet is crucial to ensure non-negligible gravitational effects. When the Bond number is small, it indicates that interfacial forces dominate over gravitational forces, causing the drop profile to deviate only slightly from sphericity. In this scenario, the method's sensitivity is inherently low, as a minor alteration in the drop profile leads to a significant change in the measured interfacial tension. To overcome this limitation, one approach is to use a larger drop, although this may be challenging if the droplet and continuous phases have similar densities and surface tensions. The measurement can also be affected by the drop volume. The Worthington number $Wo = V_d/V_{max}$ scales the drop volume, V_d, by the theoretical maximum drop volume $V_{max} = \pi D_n \gamma / \Delta\rho g$, where D_n is the needle diameter. The Worthington number can effectively be used as a post-measurement 'sanity check' to indicate the likely measurement precision. The measurement is reliable when Wo tends to 1 [151]. For fitting the theoretical drop profile to the experimental image, an open software, Opendrop, was employed [151]. The results are presented in Section 4.1.1.

The contact angles of PDMS, acetone, and the overlapped configuration on glass were determined using the Sessile Drop method. The theoretical elucidation of contact angle is derived from contemplating a thermodynamic equilibrium involving three phases: the spreading liquid phase (L), the solid phase (S), namely the substrate across which the liquid spreads, and a third phase (G), which may be gas or liquid, in which both are enveloped. In this context, being the solid–third phase interfacial energy γ_{SG}, the solid–liquid interfacial energy γ_{SL}, and the liquid–third phase interfacial energy, i.e. the interfacial tension, γ_{LG}, the equilibrium contact angle θ_C can be determined using the Young equation. This equation establishes a relationship between these interfacial energies and the resultant contact angle.

$$\gamma_{SG} - \gamma_{SL} - \gamma_{LG}\ cos\ \theta = 0 \tag{3.4}$$

The contact angle of a sessile drop was measured utilizing a contact angle goniometer. High-resolution camera was employed to capture images, and a specialized software, ImageJ, was used for contact angle evaluation. The experimental setup utilized for these measurements is identical to the one illustrated in Figure 3.2, which is also employed for interfacial tension measurements. The results are presented in Section 4.1.1.

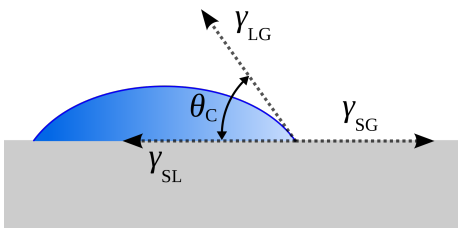

Figure 3.4. Sessile Drop schematic illustration. Schematic of a liquid drop showing the quantities in the Young equation.

3.1.3 Lateral View Set-up

The described experimental setup was constructed to intentionally apply a predetermined motion to the system under examination. Figure 3.5 illustrates the experimental arrangement. The experimental videos were recorded using a ThorLabs sCMOS Camera equipped with a telecentric lens (Edmund 1x TML Silver). The glass vessel, with a diameter of 140 mm, was connected to a stepper motor through a glass container holder designed using Autodesk® Fusion 360™and 3D printed with a Prusa i3 MK3S+ printer in Polylactic Acid (PLA). A stepper motor (NEMA 34HE59-6004S, Bipolar, 4 wires) was utilized for the experiment. Its primary function was to introduce various types of motion. The controlling code for the stepper motor enabled the implementation of diverse functions, providing flexibility in the types of motion the motor could execute. The details of motor control are documented in section 3.1.5.

The arrangement was employed to apply sinusoidal rotational motion and disturb the interface between PDMS and Acetone. The layers composing the system were of equal height, as detailed in Section 4.1.4.

Additionally, the setup was utilized for spreading experiments to measure the height of the PDMS layer spreading in an acetone environment, with results presented in Section 4.1.3. Spreading experiments were conducted at rest, with PDMS volume set at 1 ml and acetone volume at 120 ml. The PDMS layer had a diameter smaller than the vessel, allowing acetone to overlap and fill the remaining volume around it.

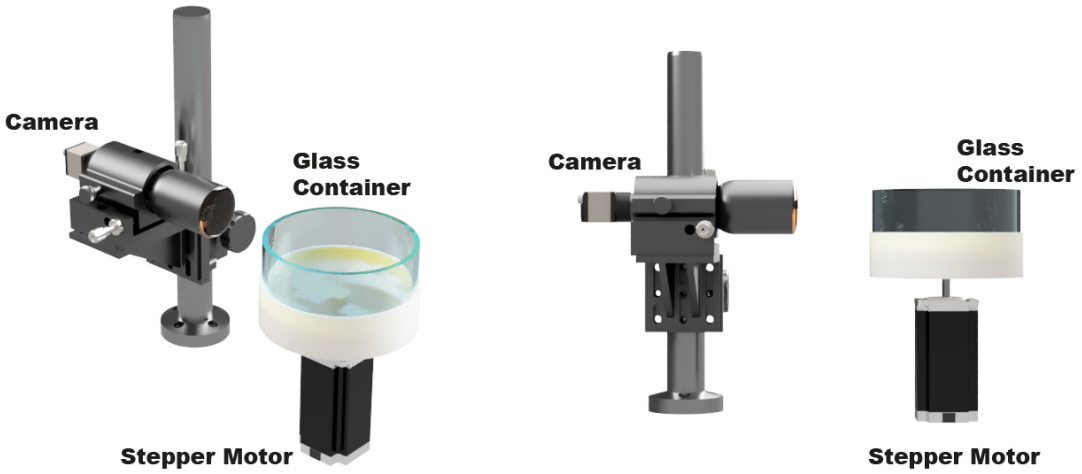

Figure 3.5. Oscillatory Kelvin-Helmholtz Instability set-up. 3D illustration of the experimental set-up.

3.1.4 Top View Set-up

The experimental setup described here was employed to investigate the Hydrodynamic Fingers Instability. The findings of these experiments are presented in Sections 4.1.4, 4.1.5 and 4.1.6. Figure 3.6 provides an overview of the experimental arrangement. The glass container, with a diameter of 140 mm, is connected to a stepper motor. The details of motor control are documented in section 3.1.5. A vessel holder, created using Autodesk® Fusion 360™and 3D printed with a Prusa i3 MK3S+ printer using Polylactic Acid (PLA), secures the glass container to the stepper motor. A GoPro camera (Hero 8, 4000x3000 pixel, 30 fps) is affixed to the holder through a scaffolding, also designed on Autodesk® Fusion 360™and 3D printed with a Prusa i3 MK3S+ printer using PLA. This scaffolding serves the dual purpose of balancing the weight and preventing any issues related to labeling the glass substrate. The built-in camera moves in tandem with the vessel, enhancing the visualization of the experimental dynamics. To mitigate vibrations associated with the transfer of motion from the stepper motor to the glass vessel, a vibration damper, designed on Autodesk® Fusion 360™and 3D printed with a Prusa i3 MK3S+ printer using PLA, was employed. As indicated in section 3.1.5, the vibration damper does not impact the motion transmission from the stepper motor to the vessel.

The system under investigation is described in Section 3.1.1. To ensure alignment of the PDMS layer center with the container center, a custom fluid dispenser was designed using Autodesk® Fusion 360™and 3D printed with a Prusa i3 MK3S+ printer, using PLA (see Figure 3.7a). The dispenser, equipped with a syringe holder, can be positioned in the vessel for precise deposition of

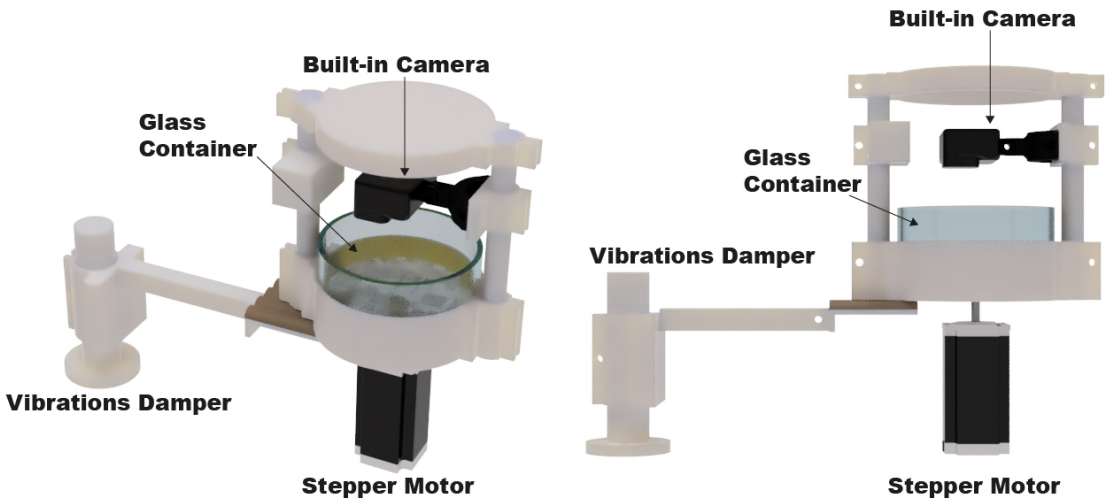

Figure 3.6. Hydrodynamic Fingers Instability set-up. 3D illustration of the experimental set-up.

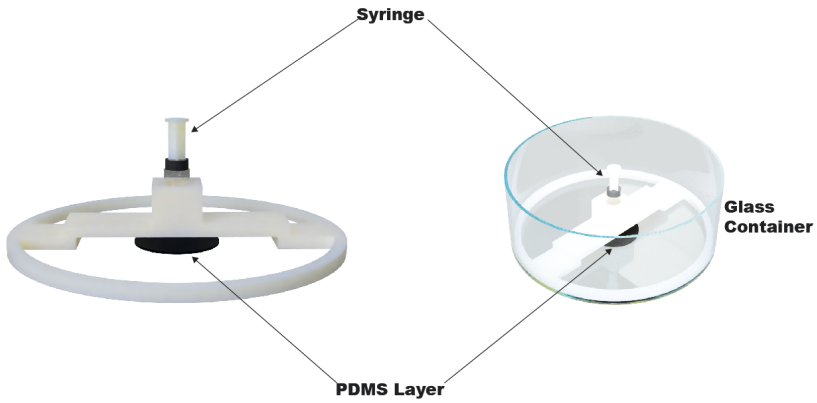

(a)

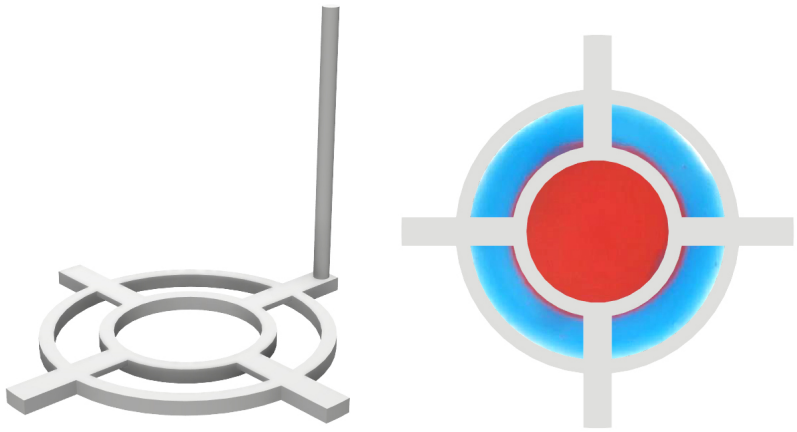

(b)

Figure 3.7. Fluid Deposition. a) CAD of the fluid dispenser utilized for aligning the PDMS layer at the center within the vessel. **b)** CAD of fluid dispenser for aligning PDMS at the center within a vessel and creating a concentric configuration with two different colored PDMS layers.

PDMS. Careful addition of acetone is crucial to prevent the mixing of the two fluids and disturbances to the deposited PDMS layer. Due to the difficulty in depositing the PDMS layer with a consistent diameter in each experiment, a waiting time of 10 min was planned between fluid deposition and the start of perturbation, allowing the layer to spread and ensuring consistent initial conditions for all experiments (as detailed in Section 4.1.3). After the spreading phase and establishing initial conditions, the system is perturbed by a rotational sinusoidal perturbation around the central axis of the container, $\Omega = A\ sin\ \omega t$ where A represents the oscillation amplitude and ω is the angular frequency. Experiments were conducted by varying these parameters within the ranges $A \in [0 - 0.2]\ [rad]$ and $\omega \in [0 - 100]\ [rad/s]$.

A different custom fluid dispenser was designed using Autodesk® Fusion 360™and 3D printed with a Prusa i3 MK3S+ printer, using PLA (see Figure 3.7b), for creating the concentric configura-

tion with two different colored PDMS layers. The dispenser features a separation wall at a certain radial position to separate the two layers, and the connection between the internal and external walls avoids touching the container bottom, allowing the outer PDMS layer to form an annulus. The dispenser can be easily positioned within the vessel for precise fluid deposition.

3.1.5 Control of Motion System

The glass vessel's movement is imposed by a stepper motor (NEMA 34HE59-60004S, Bipolar, 4 wires), which is effectively managed by a Fully Digital Stepper Driver DM860I. The control of the stepper motor is orchestrated through custom code (reported in Appendix A.1) for Arduino Uno, an open-source microcontroller board featuring the Microchip ATmega328P microcontroller (MCU). An electric power supply (Velika S-800-48 Switching Power Supply) provides the necessary electrical power for the system. This setup enables precise control and coordination of the motion applied to the vessel.

The stepper motor is designed to perform at 40000 or 51200 steps for each complete 360° rotation, depending on the desired level of precision and power. In the code, the specified motion is denoted as $\Omega = A_s \; sin \; \omega t$, with A_s representing the motion in steps and ω $[rad/s]$ the angular frequency. To assess motion characteristics, motion checks were conducted at various values of A_s and ω, considering using a vibration damper in the system. The number of steps determines the oscillation amplitude, as expressed by $A = 2\pi/A_s$. The movement of the glass container was monitored using the open-source software Tracker. The radial position of the tracked motion over time was analyzed utilizing a fitting curve denoted as $\Omega = A_{fit} \; sin \; \omega_{fit} t$. In Figure 3.8, an example with $A = 0.31$ $[rad]$ and $\omega = 1$ and 10 $[rad/s]$ is presented. The table 3.1 highlights instances where the values employed in the Arduino code align well with the fitted parameters, indicating

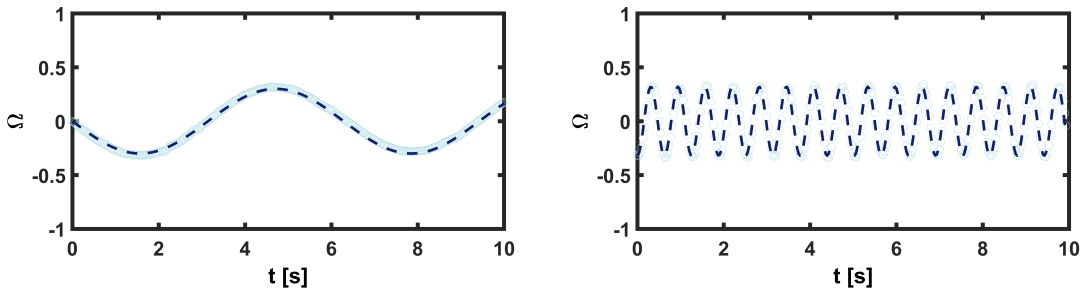

(a) (b)

Figure 3.8. Motion system. Radial position of the tracked motion over time. *[Legend]* $\Omega = A_{fit} \; sin \; \omega_{fit} t$ and experimental points for **a)** $A = 0.314$ $[rad]$ and $\omega = 1$ $[rad/s]$ and **b)** $A = 0.314$ $[rad]$ and $\omega = 10$ $[rad/s]$.

Table 3.1. Fitting parameters for vessel motion.

Steps	$A[rad]$	ω $[rad/s]$	A_{fit} $[rad]$	ω_{fit} $[rad/s]$	R^2
1000	0.157	10	0.154	10	0.9902
1000	0.157	15	0.157	15	0.998
1000	0.157	20	0.157	20	0.998
2000	0.314	1	0.305	0.995	0.995
2000	0.314	2	0.906	2.002	0.9955
2000	0.314	10	0.327	10	0.99
3000	0.471	10	0.456	10	0.938
4000	0.628	10	0.636	9.998	0.982
5000	0.785	10	0.777	10	0.9792

effective control of the stepper motor and the container's motion. In conclusion, the vibration damper's sole effect is eliminating issues associated with vibrations.

3.1.6 Images Processing

The leftmost image in Figure 3.9 is a typical experimental snapshot. It underwent processing using a custom MATLAB® code (detailed in Appendix A.2), as demonstrated by subsequent images in the same figure. The primary objective of this code is edge detection, specifically the determination of the coordinates of the contact line of the PDMS layer, achieved through the application of the Sobel operator. This operator serves as a discrete differentiation operator, approximating the gradient of the image intensity function. At each pixel, the Sobel operator yields either the corresponding gradient vector or the norm of this vector. Notably, the operator is computationally efficient, involving convolution with a small, separable, and integer-valued filter in both horizontal and vertical directions. It employs intensity values within a $3x3$ region surrounding each image point to estimate the respective image gradient. The coefficients that weigh the image intensities to generate the gradient approximation are exclusively integer values. A sequence of operations was performed on the images to attain this goal.

The process began by converting the image from RGB to grayscale, where each pixel represented only the intensity of light. Subsequently, a linear filter was applied, reducing the intensity at each grayscale pixel by 50% of the background intensity. Contrast enhancement was then implemented, saturating the bottom 1% and top 1% of all pixel values. This enhancement function linearly mapped pixel values between the saturation limits to a range of 0 to 1. The purpose was to boost contrast, making binarization easier and resulting in a binary image with only black and white colors. This transformation accentuated intensity gradients in the targeted region. Finally, the image underwent a complement transformation, where zeros turned into ones and ones into zeros. This reversal optimized the utilization of the Sobel operator.

This entire process aimed to enhance the magnitude of the intensity gradient in the peripheral zone of the PDMS contact line, enabling more effective application of the Sobel operator. The outcome is a matrix, mirroring the image's dimensions, with logical values of 0 and 1. A value

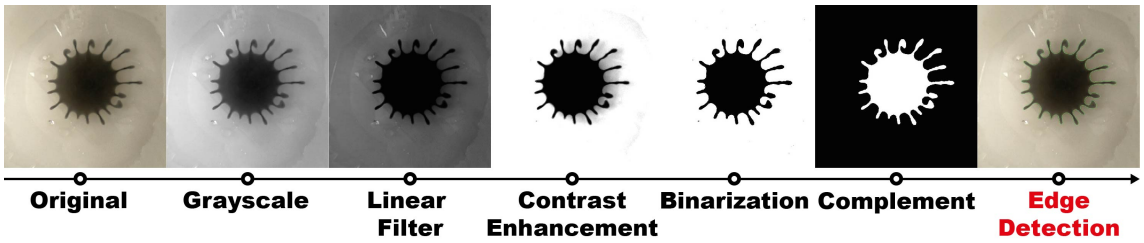

Figure 3.9. Image Processing. Steps for edge detection in image processing using a MATLAB® custom code (reported in Appendix A.2). The code is specifically designed for analyzing experimental images captured from a top view.

of 1 indicates the presence of an edge at that position as defined by the Sobel operator. In this matrix, the horizontal and vertical positions of "true" values determine the pixel coordinates (or in millimeters when multiplied by a conversion factor) of each point on the edge. Armed with these coordinates, various calculations can be derived, such as the perimeter of the PDMS layer, the radial extension of the fingers, and other relevant measurements.

3.2 Thin Film Drainage

3.2.1 Materials and Interferometer Set-up

The liquid drainage after bubble-solid interactions was captured using the interferometer reported in Figure 3.10. The experiments were conducted in a cylindrical chamber with a diameter of approximately 2.6 cm and a height of about 4.7 cm, as depicted in Figure 3.10*[right]*. The chamber has a needle at the bottom. All tests were carried out under room temperature conditions and atmospheric pressure. Deionized water (MilliQ, resistivity 18.2 $M\Omega$ cm) and aqueous colloidal suspensions of polystyrene (PS) with varying diameters (approximately 0.6 μm and 3 μm) and concentrations (0.1 $mg/ml, 0.15$ mg/ml and 0.3 mg/ml) were used in the experiments.

To initiate the experiments, air bubbles with a specified radius $R = 1.2 \pm 0.3$ mm were released through a 27-gauge blunt-tipped needle (0.21 mmi.d and 0.413 mm o.d). These bubbles were generated using a syringe (1 ml) connected to a pump (Harvard Apparatus Pico Plus 11, Harvard Apparatus, Holliston, MA) with a constant flow rate of 30 $\mu L/min$. The bubbles ascended and collided with a pre-cleaned hydrophilic glass slide positioned at the top. The distance between the needle tip and the glass substrate was maintained at a constant 3.2 mm for all experiments. A side camera (iDS, UI308xCPM) recording at 160 fps captured the ascension and collision events. To ensure a linear rising trajectory and prevent the creation of path instabilities or zig-zag patterns, the bubble radius was kept constant. The recorded side-view videos underwent analysis using

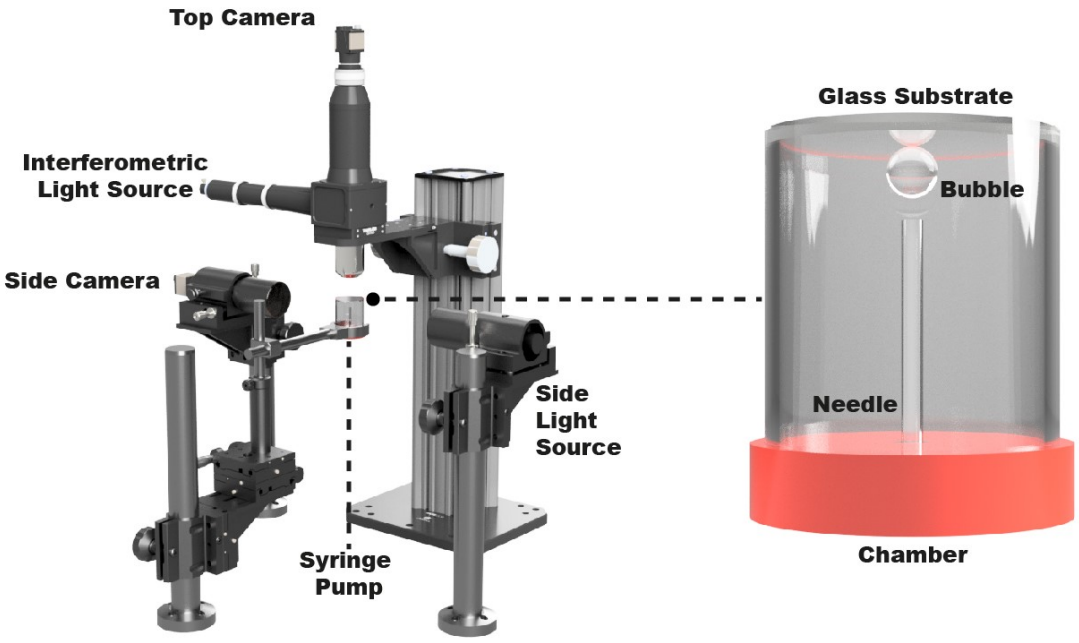

Figure 3.10. Thin Film Drainage Set-up. *[left]* Schematic of the experimental setup used to capture bubble/wall interacions. *[right]* The fluid chamber shows a bubble being released from a needle.

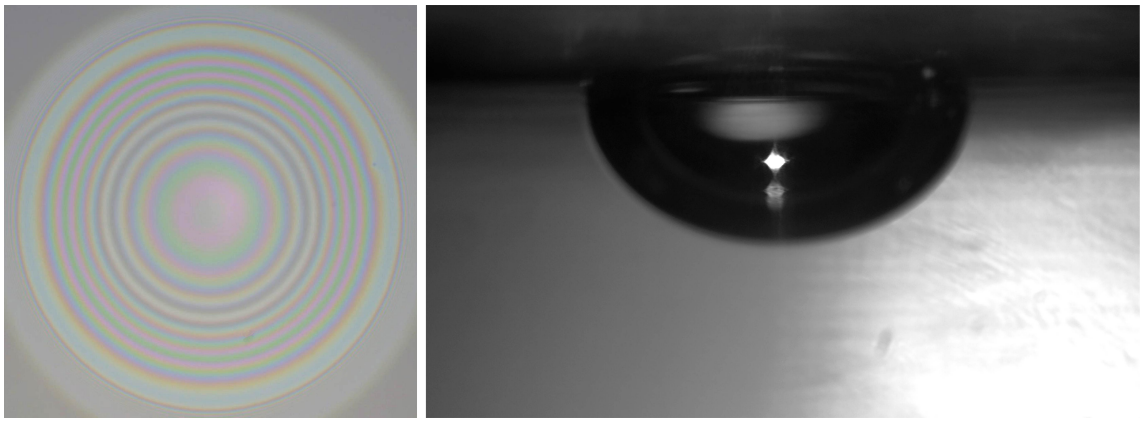

Figure 3.11. Experimental Snapshots. *[left]* A representative interference pattern from which the thickness of the entrapped film between the bubble and the wall was calculated. *[right]* An image of the bubble pressed against the glass substrate as captured using a side camera.

image processing software, including Image J and Tracker. The interferograms of the thin films were recorded using a top camera (iDS, UI306xCPC). In the interferometry setup, a white light source was employed, and the light passed through a 50:50 beam splitter directed toward the bubble impact area. A Python 2.7-based software developed in-house was utilized to map and measure the film thickness from the recorded interferograms.

In Figure 3.11, typical experimental snapshots are reported. From the side view, the volume and approach velocity of the bubble were measured. The interferograms allowed to measure the thin film thickness as reported in Section 3.2.2.

A Pendant Drop Tensiometer was employed to measure the surface tension of the polystyrene aqueous suspension. The bulk viscosity was measured by using a rheometer (TA instruments discovery HR 3) with a 2° cone and plate geometry. The equilibrium contact angles of water and the colloidal suspension on the glass substrate were measured using a custom-made goniometer.

3.2.2 Interferometry

Thin film thickness profile could be measured by three-wavelength interference color analysis. The method used in this study allows to analyze and estimate the distribution of film thickness based on interference color images obtained using a color camera with three-wavelength illumination. The validity of the proposed approach was confirmed through both computer simulations and experimental tests [152].

When light strikes a thin film and is reflected by both the upper and lower boundaries, neglecting multiple reflections allows to derive the intensity as the sum of the two reflected waves

$$I(\lambda) = I_1(\lambda) + I_2(\lambda) + 2\sqrt{I_1(\lambda)I_2(\lambda)}\ cos\ \delta(\lambda) \tag{3.5}$$

where I_1 and I_2 are the intensities of waves, λ is the wavelength, and δ is the phase difference between them. Considering a uniform refractive index, $n(\lambda)$, and normal incidence of light, the

optical path difference between the two reflections from a thin film is $2n(\lambda)t$, where t is the thickness of the layer. Therefore the phase difference for light reflected from the two surfaces is $\delta(\lambda) = 4\pi n(\lambda)t/\lambda$. For a nondispersive medium, for which $n(\lambda) = n$

$$I(\lambda) = I_1(\lambda) + I_2(\lambda) + 2\sqrt{I_1(\lambda)I_2(\lambda)}\ cos\ (4\pi nt/\lambda) \tag{3.6}$$

Considering the case of three-wavelength (RGB) illumination, $I_1 = I_2 = 1/2$ and $\lambda_R = 600\ nm, \lambda_G = 560\ nm$ and $\lambda_B = 470\ nm$. The theoretical intensities of each wavelength for the optical thickness range $0 - 2.5\mu m$ were calculated, obtaining the synthesized color chart as function of the film thickness.

In the analysis of interference patterns within the scope of the current experiments, a bespoke software application was employed, developed using Python 2.7 [153]. The software encompasses three principal functionalities:

- Generation of a color map tailored to the specific hardware configuration and film material under investigation.
- Transformation of interference patterns into corresponding film thickness values.
- Visualization and exportation of data for subsequent post-processing.

Initially, the software integrates the spectral characteristics of the light source, camera pixel sensitivity, and optical components with the refractive indices of the film materials. This integration facilitates the computation of colors corresponding to film thicknesses within the predefined range of study. Subsequently, a graphical user interface is utilized for the sequential analysis of individual video frames. During frame analysis, pixels along distinct color contours are manually selected, and their colors are matched to entries in the color map, thereby associating them with specific film thicknesses. This manual matching process introduces an estimated error of approximately $\pm 15\ nm$ in film thickness, based on the discernible spacing between different color bands within the color map. Finally, the film thickness across the entire frame is estimated by employing linear interpolation on the remaining pixels. Leveraging the manually matched pixels, this process yields a 3D surface representation of the film thickness. Subsequently, the data from each analyzed frame are exported to files for subsequent post-processing.

Results and Discussion

4.1 Hydrodynamic Fingers Instability

In this chapter, qualitative and quantitative evidence of a novel Hydrodynamic Fingers Instability are presented. The experimental system comprises layered PDMS and Acetone in a gravitationally stable configuration, enabling the examination of the miscible interface under rotational sinusoidal motion. The destabilization process, distinctly observable and unprecedented, necessitates the characterization of the system through *Effective Interfacial Tension* and contact angle measurements, given their significance in the onset and final stages of destabilization (Section 4.1.1).

The reported destabilization process involves the convergence of two instabilities: the well-known Oscillatory Kelvin-Helmholtz instability and a newly identified one leading to the formation of fingers. As elaborated in Section 4.1.2, the system experiences perturbation through a motion, inducing different velocities in the two fluids, generating an azimuthal pressure gradient that results in an oscillatory shear flow. The action of shear stresses on the interface induces the formation of waves. Upon reaching a critical magnitude in wave height, the centrifugal force, directed radially, becomes more pronounced in regions with a larger PDMS layer, influenced by wave formation, thereby contributing to the radial growth of fingers. In contrast, the centrifugal force is less pronounced in areas between these regions where the cross-section has a smaller height. To enhance control over the destabilization phase, an initial spreading phase at rest was implemented to ensure consistent initial conditions for each experimental run (Section 4.1.3). Qualitative evidence of the Oscillatory Kelvin-Helmholtz instability is detailed in Section 4.1.4, while quantitative conclusive evidence is presented in Section 4.1.5. The role of centrifugal force in this phenomenon is further elucidated in Section 4.1.6 through scaling analysis.

4.1.1 *EIT* and Contact Angles Measurements

For characterizing the system formed by PDMS and Acetone, the *EIT* was determined utilizing the Pendant Drop Method, as outlined in Section 3.1.2. This method was specifically adapted for

liquid-liquid systems. Fig. 4.1a illustrates the formation of a drop by PDMS, surrounded by Acetone. Multiple experimental snapshots were employed to generate the graph presented in Fig. 4.1b. The averaged *Effective Interfacial Tension* is determined to be $\sigma = 0.76 \pm 0.04\ mN/m$. This estimation is considered reliable as indicated by the Bond number $Bo = 0.4$, which characterizes a regime where shape perturbations result in only minor variations in the measured interfacial tension. Additionally, the Worthington number $Wo > 0.4$ is sufficiently large to mitigate the effect of drop volume on measurement sensitivity [151]. The limitations of the pendant drop method constrain the attainment of a larger Wo value. In this method, the drop formation becomes challenging when the surface tension of the pure liquids in air closely aligns and the viscosity of the fluid constituting the droplet is elevated.

The measurements align with the theoretical prediction reported in the literature where a preliminary estimation of the interfacial tension between two fluids involves the difference in surface tension of the pure liquids. Therefore, $\sigma = |\sigma_{Ac} - \sigma_{PDMS}| \sim 0.7$, where $\sigma_{Ac} = 21.5\ mN/m$ represents the surface tension of Acetone and, $\sigma_{PDMS} = 20.8\ mN/m$ is the surface tension of PDMS.

The *EIT* value can be regarded as a quasi-equilibrium value because the diffusion time (7 hours, as reported in Section 3.1.1) is significantly greater than the experimental time ($\sim 15\ min$). While the *EIT* approaches zero during the diffusion time, in the pendant drop method, after the drop formation, and during the conducted experiments following fluid deposition, it can be considered to approximate a quasi-equilibrium condition.

The system exhibits an *Effective Interfacial Tension* despite the miscibility of the two fluids. As reported in Section 2.2.3, concentration inhomogeneities at a miscible interface result in the emergence of the so-called Korteweg stresses. These stresses emulate the interfacial tension observed in immiscible systems [44, 58, 103, 111]. The magnitude of the *Effective Interfacial Tension*

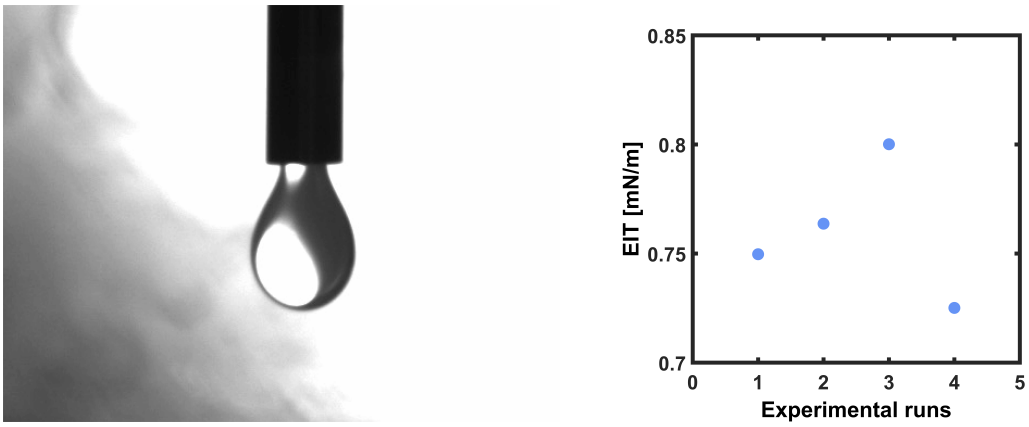

(a) (b)

Figure 4.1. PDMS-Acetone *EIT* measurements. a) Experimental snapshot of the pendant drop formed by PDMS ($\mu = 10\ Pa \cdot s$) in Acetone environment. **b)** *EIT* values for several experimental runs.

is quite noticeable and has the potential to influence hydrodynamics.

On the other hand, the Sessile Drop Method was used for measuring the contact angle, as detailed in Section 3.1.2. Figs. 4.2a and 4.2b depict the Acetone and PDMS drop on glass, in air, respectively, while Fig. 4.2c represents the layered systems formed by a drop of PDMS on glass, surrounded by Acetone. Here, the ambient fluid is a liquid. The equilibrium contact angles were measured using a custom-made goniometer, resulting in $\theta_{Ac} = 21°$ (Fig. 4.2a), $\theta_{PDMS} = 29°$ (Fig. 4.2b), and $\theta_{Ac-PDMS} = 133°$ (Fig. 4.2c).

The contact angle measurements on the glass substrate reveal that acetone exhibits greater wettability than PDMS, which could assume significance as it is expected to impact the final stage of the newly discovered hydrodynamic instability.

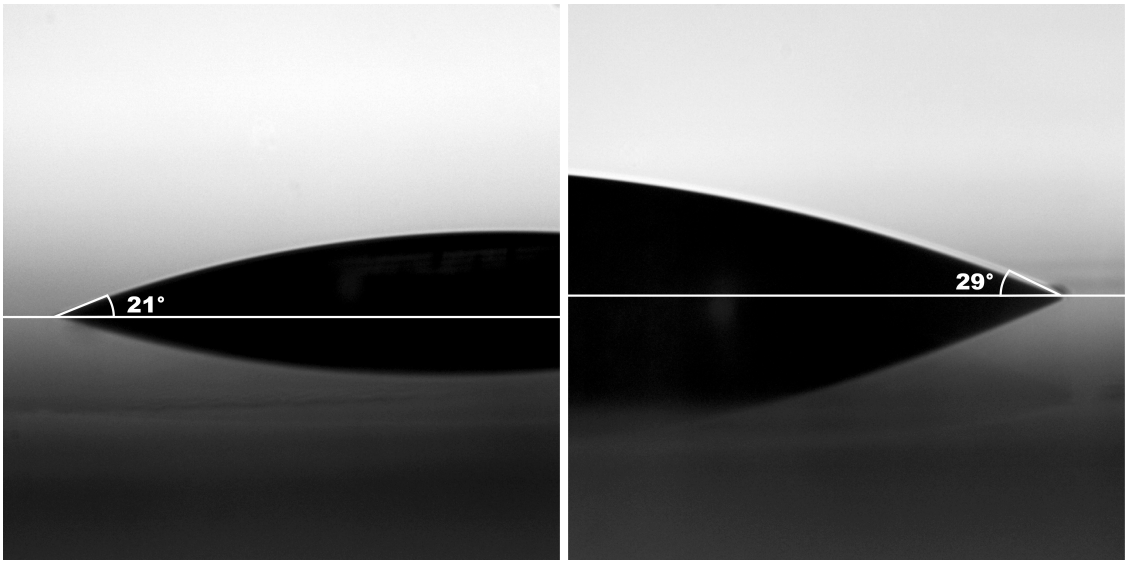

(a) (b)

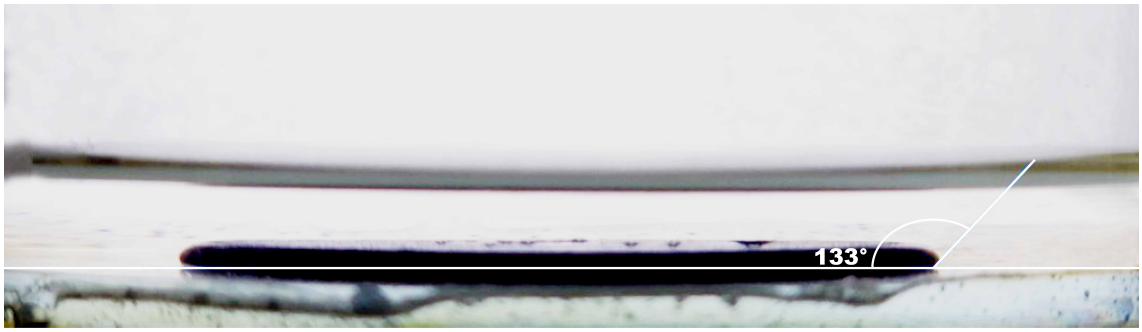

(c)

Figure 4.2. PDMS-Acetone Contact Angle measurements. a) Experimental snapshot of an acetone sessile drop on glass in air. **b)** Experimental snapshot of PDMS sessile drop on glass in air. **c)** Experimental snapshot of the layered system formed by a PDMS sessile drop on glass in an Acetone environment.

4.1.2 Experimental Evidence and Qualitatively Dynamics

The experimental system is illustrated in Fig. 4.3. A PDMS layer is deposited at the center of a glass container, covering only a portion of the substrate. Acetone fills the remaining volume, overlapping with the PDMS layer. A rotational sinusoidal oscillation is applied around the container's central axis, with the centers of the container, PDMS layer, and Acetone coinciding, as Section 3.1.4 outlines. Within this system, the interface is schematically characterized by two significant regions crucial for the subsequently described dynamics: a horizontal contact surface, identified as ζ, and a vertical axisymmetric contact surface, located at a distance r from the center of the PDMS layer, and denoted as δ. This vertical contact surface defines the radial boundary surface of the PDMS layer.

After fluid deposition, four distinct phenomena can be identified (Fig. 4.4). Before imposing the motion, the PDMS layer can spread on the glass substrate for 10 minutes to mitigate any issues related to the deposition process (spreading phase). Subsequently, under the influence of the imposed motion, the spreading process accelerates (oscillated spreading phase). As the spreading phase unfolds, destabilization occurs. The formation of waves disrupts the previously stable horizontal region, ζ, resulting in varying heights within the PDMS layer. Then, radial finger-like protrusions become evident, which emerge and grow from the vertical boundary surface, δ, as the onset of the waves alters its cross-sectional profile (destabilization phase).

The experimental snapshots, reported in 4.5, illustrate the spreading phase. During this phase, the PDMS layer exhibits a spreading behavior akin to a sessile drop on the glass substrate. As mentioned, adopting this approach helps avoid any issues associated with fluid deposition. The spreading phase remains consistent across all experimental runs, regardless of the oscillation amplitude and angular frequency variations, and it lasts for 10 *min*, ending when the perturbation starts. This phase serves as a standardized initial condition, as outlined in Section 4.1.3.

In Figures 4.6, 4.7, and 4.8, experimental snapshots of the O-spreading, waves, and fingers phase are presented for various oscillation amplitudes and angular frequencies. Following the initiation of perturbation, there is an acceleration in the spreading process, referred to as the O-Spreading phase, evident in the initial two columns of each figure. Concurrently, a distinctive

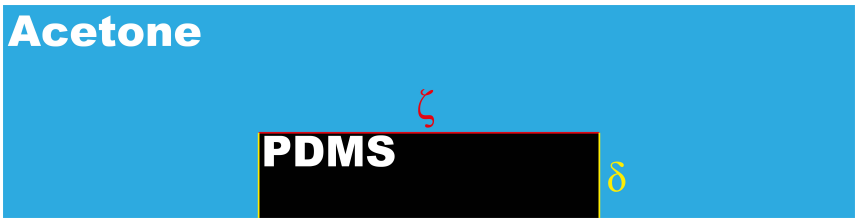

Figure 4.3. Experimental system. Sketch of the overlapped system comprising PDMS (black) and Acetone (blue). The interface is schematically characterized by two significant regions: a horizontal contact surface, ζ, and a vertical axisymmetric contact surface, located at a distance r from the center of the PDMS layer, δ.

Figure 4.4. Dynamics timing. Experimental and dynamics steps.

pattern of valleys and hills emerges on the horizontal interface, discernible through variations in black intensity across the figures. As time progresses, as shown in the third column of each figure, small protrusions begin to develop on the vertical interface. These protrusions have the potential to elongate, giving rise to elongated fingers in the radial direction. The figures indicate a discernible influence of oscillation amplitude and angular frequency on the formation of fingers, as depicted in the final columns of each figure.

Figure 4.9 illustrates explicitly how the number of fingers (N) varies with angular frequency for different oscillation amplitudes. When the amplitude A is held constant, there is a noticeable increase in the number of fingers with higher values of ω. Similarly, when ω is fixed, increasing the amplitude (as indicated by the upward progression of the red dashed line in the figure) leads to a rise in the number of fingers. Along the green dashed line, the number of fingers remains constant. In this case, decreasing the amplitude (from left to right) necessitates a larger ω for the system to form the same number of fingers.

In Figure 4.10, the spatio-temporal progression of the PDMS layer contact line during spreading, O-spreading phases, and destabilization is depicted. By referencing the color bar, time is represented from white to black. The contour lines were generated using a custom image process-

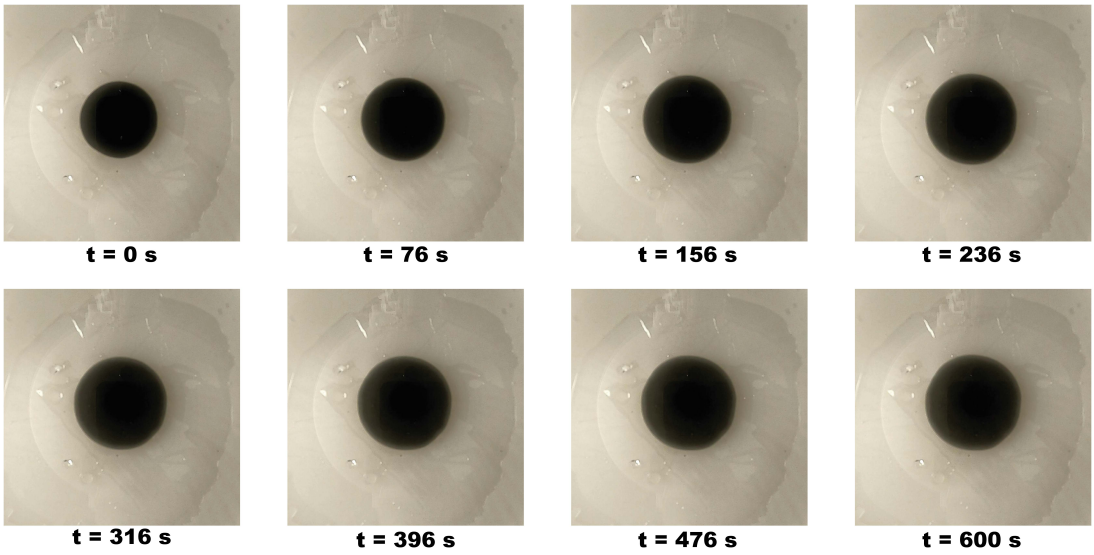

Figure 4.5. Spreading phase. Photographs capturing the experimental snapshots of the spreading phase precede the perturbation of the system, serving to define the initial conditions ($t_{spread} = 10\ [min]$).

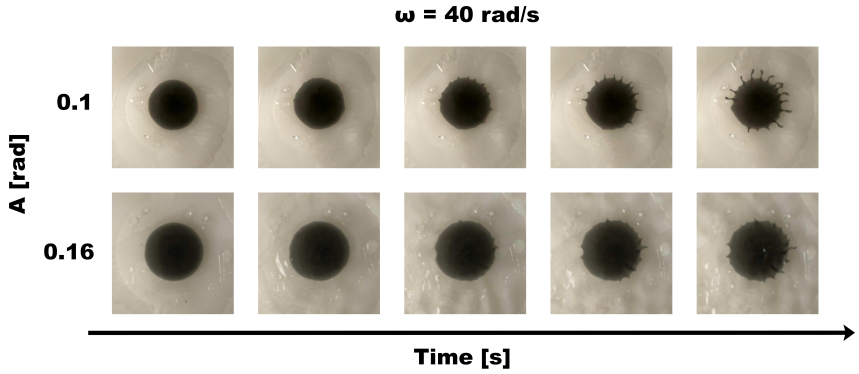

(a)

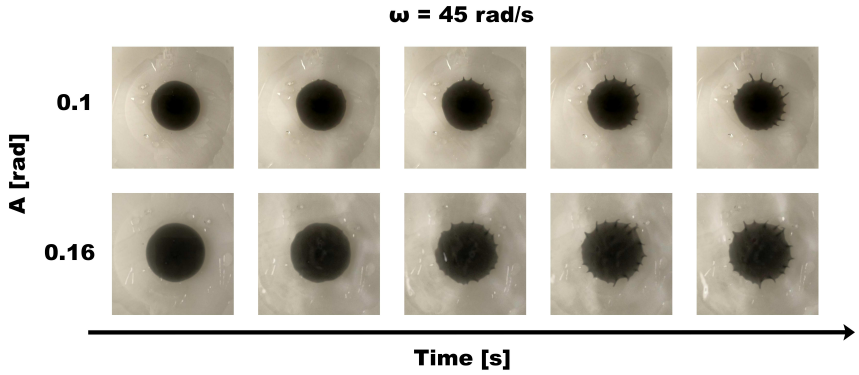

(b)

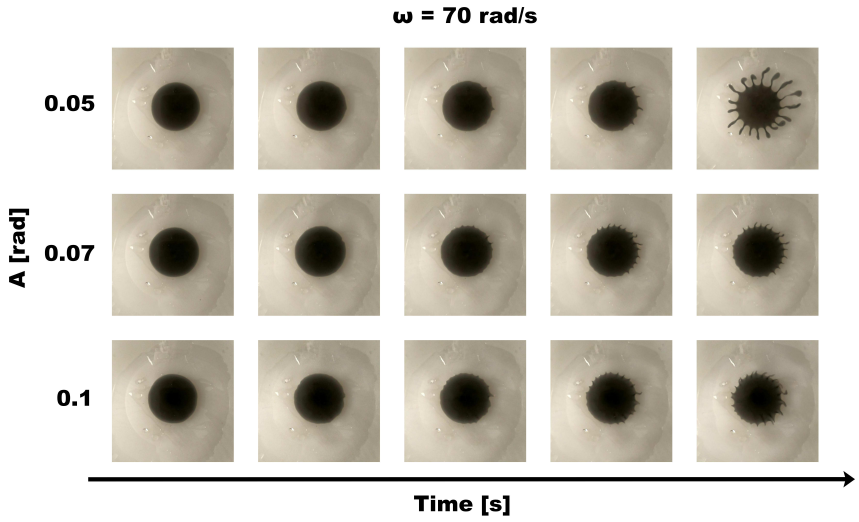

(c)

Figure 4.6. Hydrodynamic Fingers Instability: experimental snapshots. Top view of the PDMS fingers spatio-temporal evolution, growing in acetone bulk for several oscillation amplitude, A, and **a)** $\omega = 40$ $[rad/s]$ **b)** $\omega = 45$ $[rad/s]$, and **c)** $\omega = 70$ $[rad/s]$.

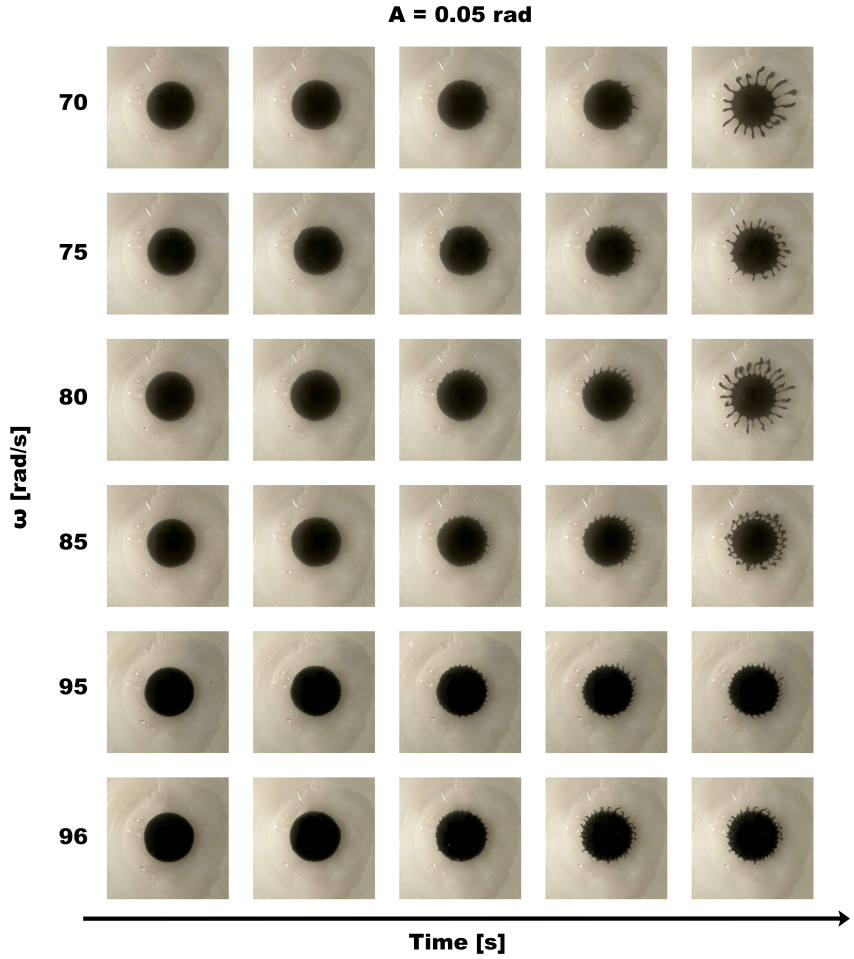

(a)

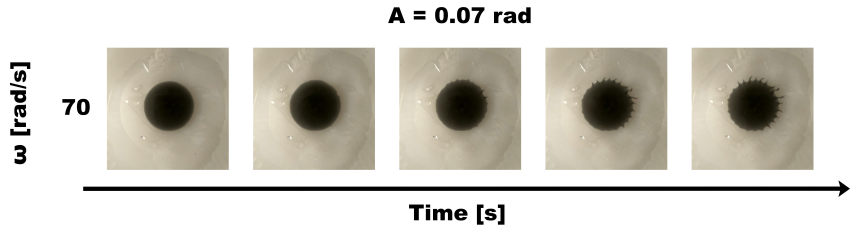

(b)

Figure 4.7. Hydrodynamic Fingers Instability: experimental snapshots. Top view of the PDMS fingers spatio-temporal evolution, growing in acetone bulk for several angular frequencies, ω, and **a)** $A = 0.05$ $[rad]$, and **b)** $A = 0.07$ $[rad]$

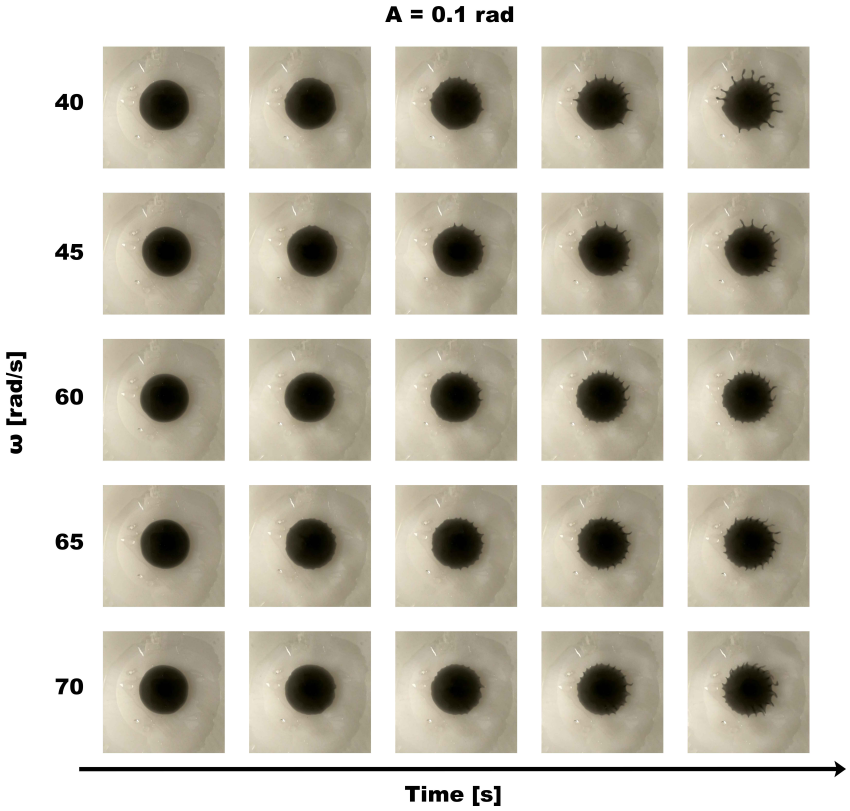

(a)

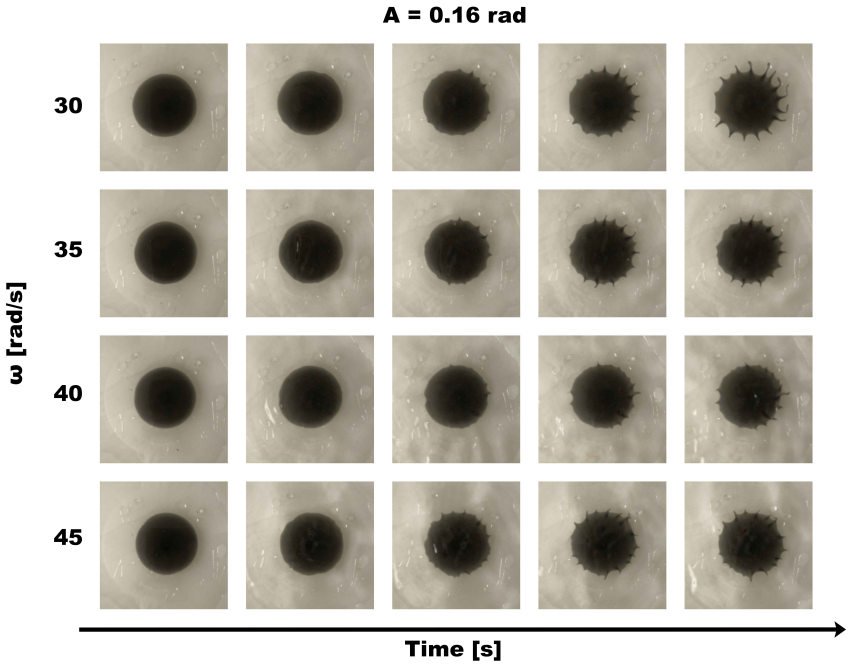

(b)

Figure 4.8. Hydrodynamic Fingers Instability: experimental snapshots. Top view of the PDMS fingers spatio-temporal evolution, growing in acetone bulk for several angular frequencies, ω, and **a)** $A = 0.1$ $[rad]$, and **b)**$A = 0.16$ $[rad]$

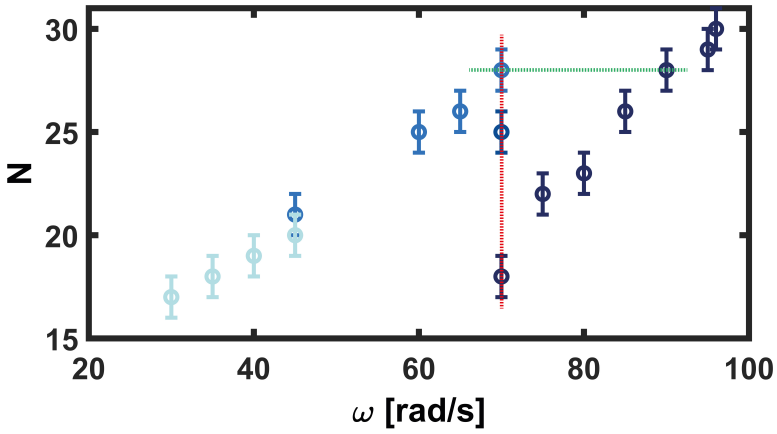

Figure 4.9. Number of Fingers. Number of fingers, N, for different angular frequency, ω, with $A = 0.05$ $[rad]$, $A = 0.07$ $[rad]$, $A = 0.1$ $[rad]$, and $A = 0.16$ $[rad]$.

ing MATLAB® code, detailed in Section 3.1.4. In Fig. 4.10a, a conventional spreading behavior on the glass substrate is evident, where the contact line of the layer maintains nearly axisymmetry. Moving on to Fig. 4.10b, a more pronounced radius increase is observed over time (light to dark gray curves). Following the acceleration of spreading induced by imposed oscillation, specific segments of the edge deviate from axisymmetry, forming small bumps that grow radially. Simultaneously, the edges between these bumps recede radially.

Experiments using PDMS with the same viscosity but colored differently, in the same configuration reported in Section 3.1.1, were conducted to qualitatively enhance the visualization of valleys and hills pattern, and radial flow, leading fingers formation. In Figure 4.11, three experimental snapshots depict the process' initial, intermediate, and final stages. By qualitatively assessing the intensity of colors in the leftmost image as a reference, varying color intensity corresponds to different heights in the PDMS layer. The color darkens as more material is present. Specifically, lighter colors indicate smaller heights, whereas darker colors signify larger heights. The varying intensity of colors, particularly the blue, confirms the wave pattern. Lighter blue indicates valleys, while darker blue signifies higher layer heights, defining waves. Color mixing occurs at the contact zone between the two PDMS, with azimuthal mixing due to fluid contact and radial mixing confirming the radial flow leading to finger formation. Figure 4.12 presents a 3D reconstruction of the experimental snapshot from Figure 4.11. The wave pattern is evident in both side (top image) and top views (bottom image). The radial flow of red PDMS in blue PDMS is highlighted by the disappearance of the circular line, present in the image denoted as T_0, indicating the contact between the two PDMS. The line blurs with time, suggesting radial mixing is occurring.

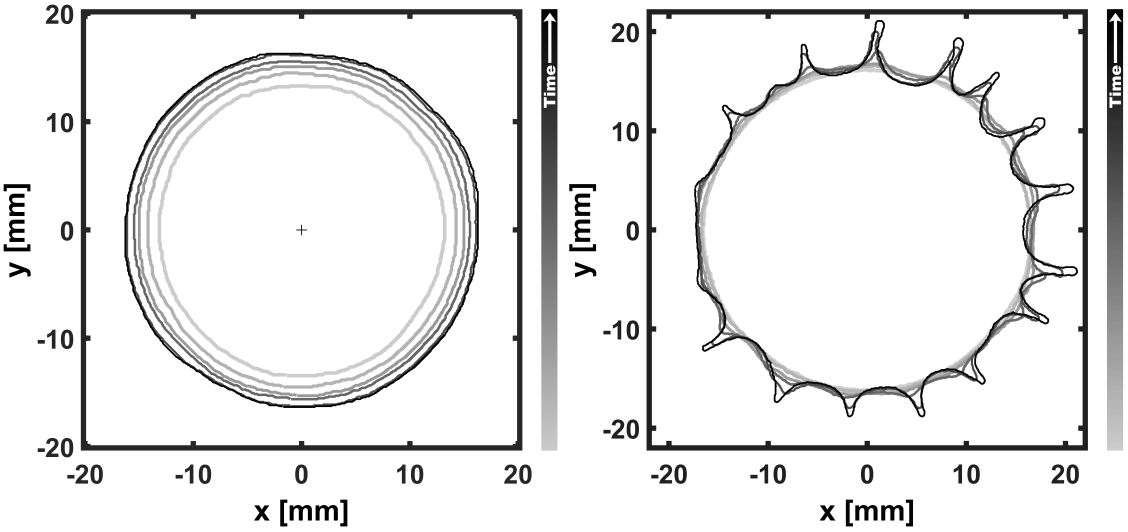

Figure 4.10. Contact Line evolution of PDMS layer. a) Spatio-temporal contact line evolution during the spreading phase. $t_{spreading} = 10$ $[min]$. PDMS volume $V = 1$ ml. The spreading phase is the same for all experimental runs. Curves at times of 0, 76, 146, 236, 476, and 600 s are represented. **b)** Spatio-temporal contact line evolution during destabilization. PDMS volume $V = 1$ ml, oscillation amplitude $A = 0.16$ rad, angular frequency $\omega = 30$ rad/s. Curves at times of 0, 12, 25, 41, 56, and 65 s are represented.

Following the formation of fingers, once they attain sufficient length, the better wettability of Acetone on the glass than PDMS facilitates fingers detachment from the substrate, allowing them to move akin to the flow of acetone (as depicted by the fingers within the yellow square in Fig. 4.13a). Throughout this progression, the fingers undergo a necking process, wherein their thickness diminishes significantly, ultimately creating tiny droplets that can be released from the tips of the fingers (as highlighted by the fingers within the red square in Fig. 4.13b).

In summary, the described phenomenon involves the evolution of a miscible interface subjected to oscillatory perturbations. Under these conditions, the horizontal region exhibits wave-like deformations, while the vertical region forms small bumps that elongate into fluid fingers. As documented in the literature [18, 17, 22, 102], the oscillatory perturbation induces different velocities in the two fluids, creating an azimuthal pressure gradient that results in an oscillatory shear flow. The shear stresses azimuthally acting on the horizontal interface region lead to the eventual formation of waves, a characteristic of the Oscillatory Kelvin-Helmholtz instability. Moreover, the observed relationship between the number of fingers, as illustrated in Fig. 4.9, and the oscillation amplitude and angular velocity aligns with the behavior of waves resulting from this instability. In literature, during the occurrence of Oscillatory Kelvin-Helmholtz, an observed increase in the number of waves formed, corresponding to an increase in both angular frequency and oscillation amplitude of the imposed motion, is documented. [17]. In qualitative terms, the progression of waves in an Oscillatory Kelvin-Helmholtz instability aligns with the development of fingers, both exhibiting

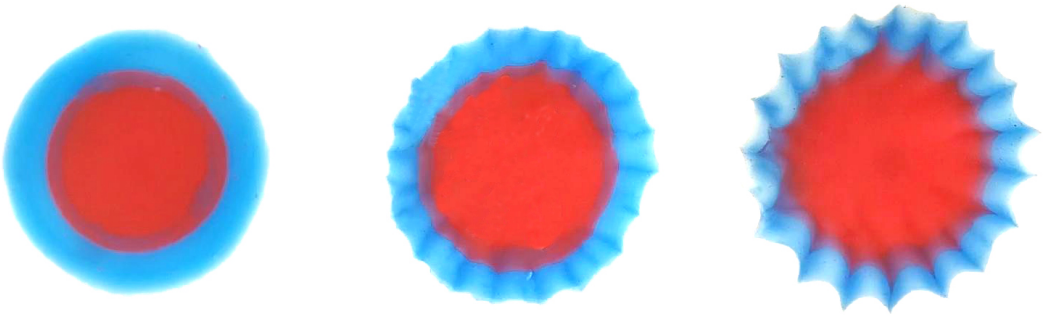

(a) (b) (c)

Figure 4.11. Hydrodynamic Fingers Instability: colored experimental snapshots A uniform layer of PDMS with consistent viscosity is utilized. Distinct colors highlight the topographical features of hills and valleys due to Oscillatory Kelvin-Helmholtz Instability and the radial flow induced by centrifugal force. The observational phases include the **a)** initial, **b)** intermediate, and **c)** final stages of the process.

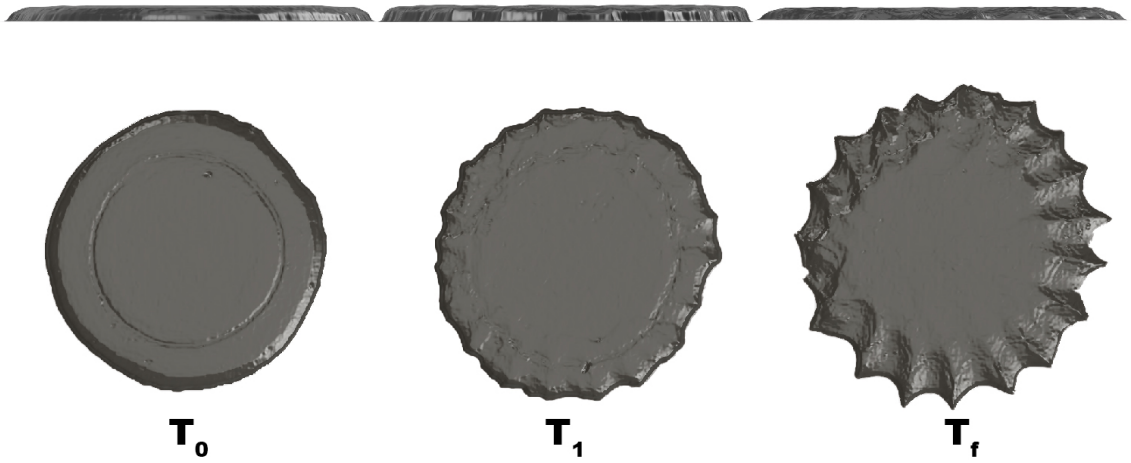

Figure 4.12. Hydrodynamic Fingers Instability: 3D reconstruction. *[top]* Lateral view, *[bottom]* top view.

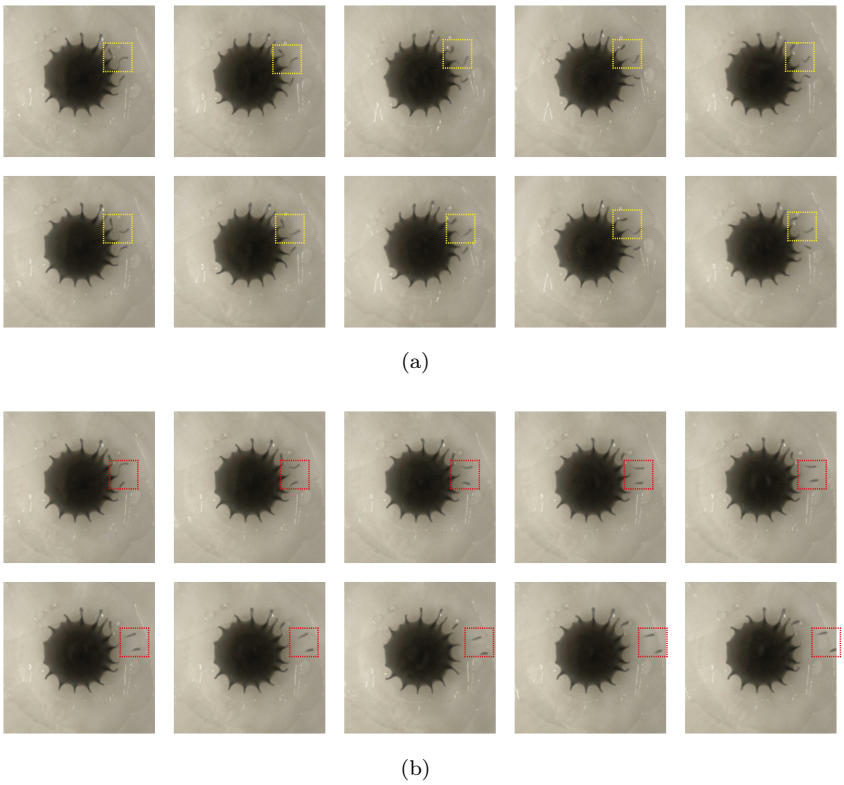

Figure 4.13. Hydrodynamic Fingers Instability: Drops formation a) When the fingers, highlighted within the yellow square, reach a sufficient length, they detach from the glass substrate due to acetone exhibiting better wettability on glass than on PDMS. Subsequently, they begin to move as acetone. **b)**. As the fingers move as acetone, their thickness gradually diminishes, akin to the phenomenon of necking observed in polymers. This reduction in thickness leads to the formation of small droplets that can be released from the tips of the fingers, as indicated by the red square.

a parallel evolution influenced by angular frequency and oscillation amplitude. This suggests a potential equivalence between the waves and the fingers, with the Oscillatory Kelvin-Helmholtz instability identified as the catalyst of the onset of new finger instabilities. The sinusoidal forcing prevents the waves from overturning, defining the initial condition for fingers growth. The radial expansion of fingers is suggested to result from a centrifugal effect. As the wave height attains a critical magnitude, the centrifugal force, oriented radially, becomes more prominent in regions where the PDMS layer is larger, influenced by the formation of waves, thereby contributing to the radial growth of fingers. In contrast, in the areas between these regions, where the cross-section has a smaller height, the centrifugal force is less pronounced.

This departure from conventional spreading processes, such as in spin coating, is notable because the centrifugal force acts non-uniformly along the azimuthal direction on the vertical interface due to the varying heights defined by the wave pattern. Additionally, during spin coating film thickness decreases, leading to swelling along the boundaries and, in the thicker region, fluid flow induces the formation of drops due to a capillary pressure gradient normal to the contact line. The centrifugal force then acts on these drops, causing them to move radially [35, 36]. In contrast, the

Hydrodynamic Fingers Instability observed here is attributed to the Oscillatory Kelvin-Helmholtz Instability, as discussed in Section 4.1.5. The role of centrifugal force in this phenomenon is further demonstrated in Section 4.1.6 through scaling analysis.

4.1.3 Initial Condition and Spreading Process

The quantitative analysis initiates with the spreading phase, which is crucial for minimizing fluid deposition-related issues. The PDMS layer is deposited on the glass substrate in an acetone environment as a sessile drop. During this phase, The PDMS layer spreads, maintaining its axisymmetric shape. Throughout this phase, the PDMS layer exhibits a reduction in height over time while its radius expands. Only the top view is available for analysis. Figure 4.14a illustrates a schematic representation of the system. The layer's perimeter can be determined by utilizing edges extracted from experimental snapshots, as mentioned in Section 4.1.2 and expounded upon in Section 3.1.4. Precisely, $p = f \sum_{i=1}^{N} g_i$, where each pixel (g) corresponds to a segment of the edge, defined as curves in a digital image where the brightness changes sharply or exhibits discontinuities, f is the conversion factor from pixel to millimeter and N is the total amount of pixel forming the perimeter. This information is obtained through a custom MATLAB® Image Processing procedure. With the inherent axisymmetry, the radius is calculated as that of a circumference, $R = p/2\pi$. Figure 4.14b depicts the temporal evolution of R for various experimental runs. Although the initial radius varies due to deposition challenges, the ultimate radius achieved after 10 minutes is consistently about the same. The difference is less than 4%, permitting an average radius $R_m = R/n$, where n is the number of runs, consistent across all experiments. The averaged radius is fitted by $R_{fit,m} = a\ exp(-bt) + c$, with $a = -3.3,\ b = 0.006$, and $c = 15.8$, as illustrated in Figure 4.14c.

To determine the initial height of the PDMS layer before imposing motion, spreading experiments employing lateral view were conducted. Assuming matching layer radii in both sets of experiments, the measured heights can be considered consistent during the spreading phase. This facilitates the determination of initial conditions before imposing motion. The duration of spreading in these experiments was consistently set at 10 minutes. Figure 4.15a presents a schematic of the system, defining h as the height of the PDMS layer at its center. To quantify these parameters, ImageJ was employed. Figures 4.15b-c depict temporal variations in h and R across different experimental runs. Figure 4.15d displays fitting curves for both parameters, where $h_{fit,L} = a'\ exp(-b't) + c'$ with parameters $a' = 1.2,\ b' = 0.008$, and $c' = 0.54$ while $R_{fit,L} = a''\ exp(-b''t) + c''$ with parameters $a'' = -3.3,\ b'' = 0.006$, and $c' = 16$. A comparison of the radius fitting curves from these experiments with those from experiments with top view reveals identical temporal evolution. This consistency leads to the assumption that the PDMS layer reaches the same height in both sets of experiments. The measured height from these spreading experiments and the previously determined radius are considered the initial conditions for subsequent perturbation experiments.

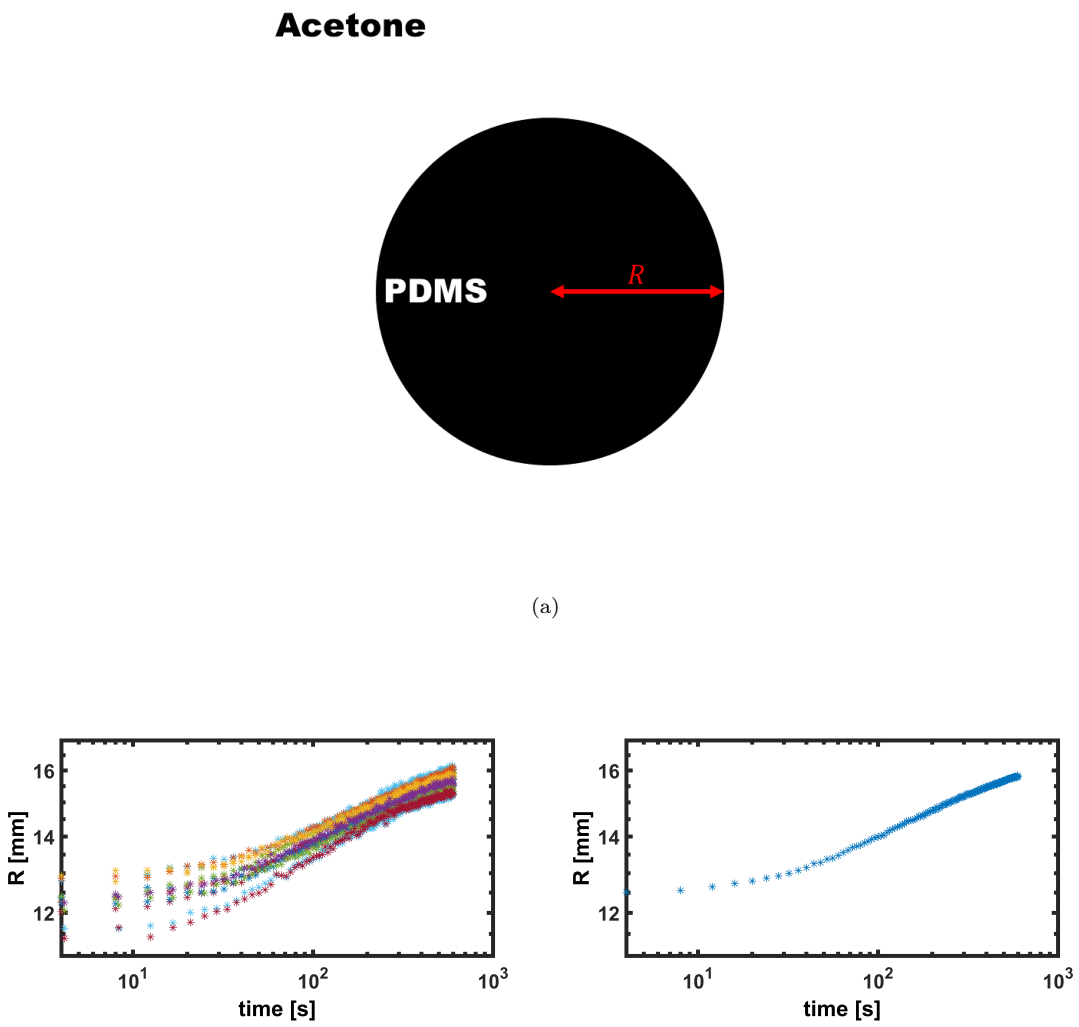

Figure 4.14. Spreading Phase: top view experiments. a) Schematic top view of the PDMS-Acetone system. $R = p/2\pi$, where p is the PDMS layer perimeter, is the PDMS layer radius. **b)** Temporal evolution of R for different experimental runs. **c)** The averaged radius temporal evolution. The last point defines the initial condition at which the perturbation starts. $t_{spreading} = 10\ [min]$. The curve is fitted as $R = a\ exp(-bt) + c$, with $a = -3.3$, $b = 0.006$ and $c = 15.8$.

To gain a more comprehensive insight into the dynamic spread of PDMS in an acetone environment on a glass substrate, the experimental images presented in Figure 4.16 reveal notable phases, particularly in the initial stages of spreading, characterized by the formation of a PDMS bridge. This occurrence is likely attributed to the fluid's deposition method. In all experiments, a PDMS layer is applied to a glass substrate, followed by filling the vessel with acetone, ensuring its level is as parallel as possible to the glass substrate. As the acetone level increases, a small central region of the PDMS interface mimics the ascent of the acetone interface. This occurrence bears resemblance to reported observations when a pendant drop of low-viscosity silicone oil is submerged in an environment of high-viscosity silicone oil [104, 105]. The phenomenon is likely attributable to

a draining flow causing the deformation of the PDMS sessile drop, leading to the formation of a bridge-like structure. After a certain duration, the deformation of the layer diminishes, possibly due to the restoring, even if small, *Effective Interfacial Tension*. The PDMS layer relaxes, as in an immiscible environment. This "instability" phenomenon warrants further investigation for a deeper understanding.

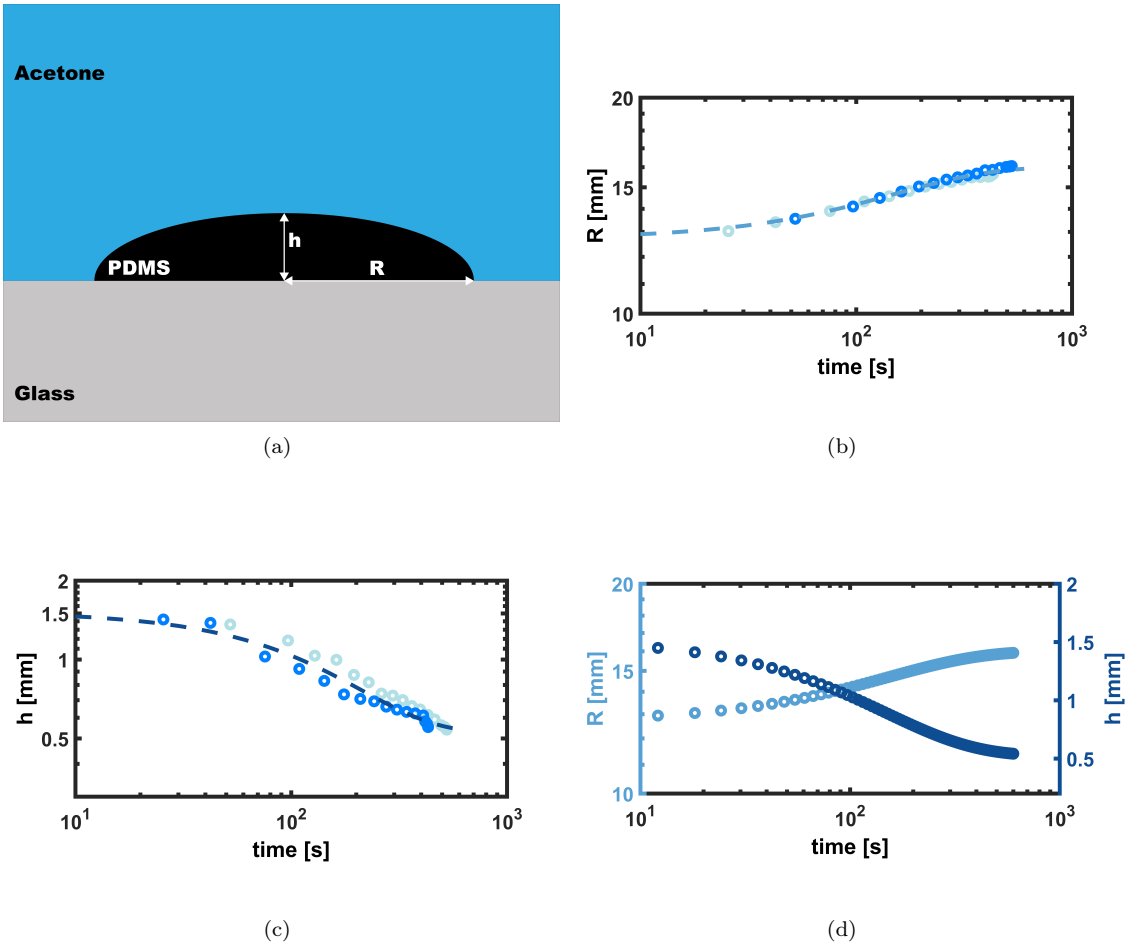

Figure 4.15. Initial Condition Definition: Lateral view experiments a) Sketch of the PDMS-Acetone system. h is the height of the PDMS layer at the center, and R is its radius. **b)** Temporal evolution of radius during the spreading phase. The dashed line defines the fitting curve $R_{fit,L} = a'' \; exp(-b''t) + c''$ for multiple experimental runs. $a'' = -3.3$, $b'' = 0.006$ and $c'' = 16$. **c)** Temporal evolution of height during the spreading phase. The dashed line defines the fitting curve $h_{fit,L} = a' \; exp(-b't) + c'$ for multiple experimental runs. $a' = 1.2$, $b' = 0.008$ and $c' = 0.54$. **d)** Initial condition of the PDMS-Acetone system. Temporal evolution of $h_{fit,L}$ and $R_{fit,L}$ during the spreading phase. $t_{spreading} = 10$ $[min]$.

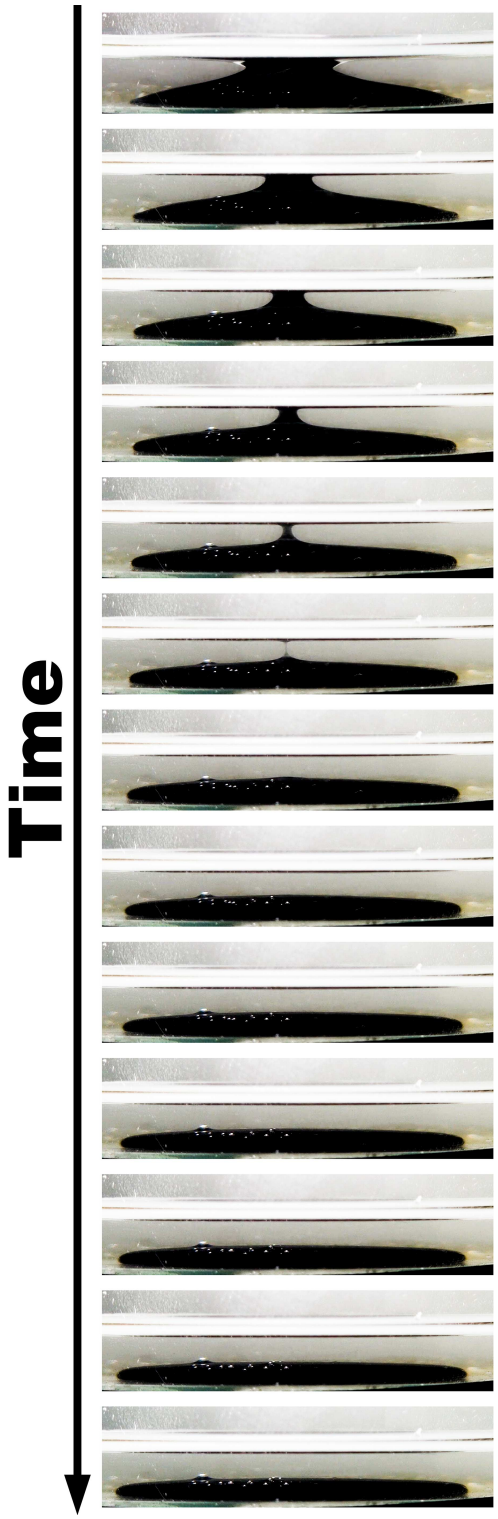

Figure 4.16. Spreading Phase . Experimental snapshots. Lateral view. The final images represent the initial condition at which the perturbation starts.

4.1.4 Oscillatory-Kelvin-Helmholtz Instability

As outlined in Section 4.1.2, the occurrence of finger instability is attributed to the Oscillatory Kelvin-Helmholtz instability. Consequently, this section presents qualitative evidence of frozen waves observed at the interface between PDMS and acetone. When two layered fluids flow, the interface between them may exhibit instability. In the case of oscillatory flows, this instability is called Oscillatory Kelvin–Helmholtz instability. As outlined in Section 3.1.3, PDMS, forming the lower fluid, covers the entire glass substrate, while acetone is the upper fluid. Experiments involve a vertically oriented cylindrical container, with relative oscillatory motion induced in the azimuthal direction by the shear force from the container sidewall and down wall. Such oscillatory shear penetrates in fluids over a depth of the order of the Stokes boundary layer thickness $\delta = \sqrt{2\mu/f\rho}$, where μ is the fluid viscosity, ρ its density and f the frequency of the sinusoidal imposed motion. The Stokes boundary layer thickness was determined for both fluids under various flow conditions applied throughout the experiments. δ_{PDMS} results in being bigger than the PDMS layer height and the radius, defining a PDMS layer that moves together with the vessel. In contrast, δ_{Ac} consistently remains smaller than the height and radius of the acetone layer, resulting in a restricted motion to thin boundary layers on the bottom and sides of the container, as well as at the interfaces with PDMS and air. Therefore, in this essential configuration, the PDMS layer shears a stationary acetone layer in an oscillatory manner. Applying such oscillatory sinusoidal motion induces a dynamic response of the interface [17, 22, 28, 102] (Fig. 4.17). Beyond a certain threshold of container rotation, a regular array of viscous waves is formed, growing into the low-viscosity fluid, developing along the periphery of the interface, fixed on the silicone oil layer. These waves exhibit sinusoidal shapes initially (Start Perturbation in Fig. 4.18), followed by growth in height during the evolution stage (middle stages in Fig 4.18). Upon eliminating the perturbation, the interface undergoes relaxation, displaying characteristics akin to an immiscible interface, and reverts to the unperturbed configuration (final stages in 4.18).

Establishing precise parameters within this system is essential, especially within the context of a miscible system where Kelvin-Helmholtz instability may occur. These parameters will be explicitly defined in Section 4.1.5. In this framework, the criteria for the emergence of a newly discovered secondary instability, outlined in Section 4.1.2 and coined as the "Hydrodynamic Fingers Instability, were established. It is essential to note that the Kelvin-Helmholtz instability serves as the underlying cause for the development of this new secondary phenomenon.

Figure 4.17. Oscillatory Kelvin-Helmholtz Instability snapshot. Experimental snapshot of frozen waves formation at PDMS-Acetone interface.

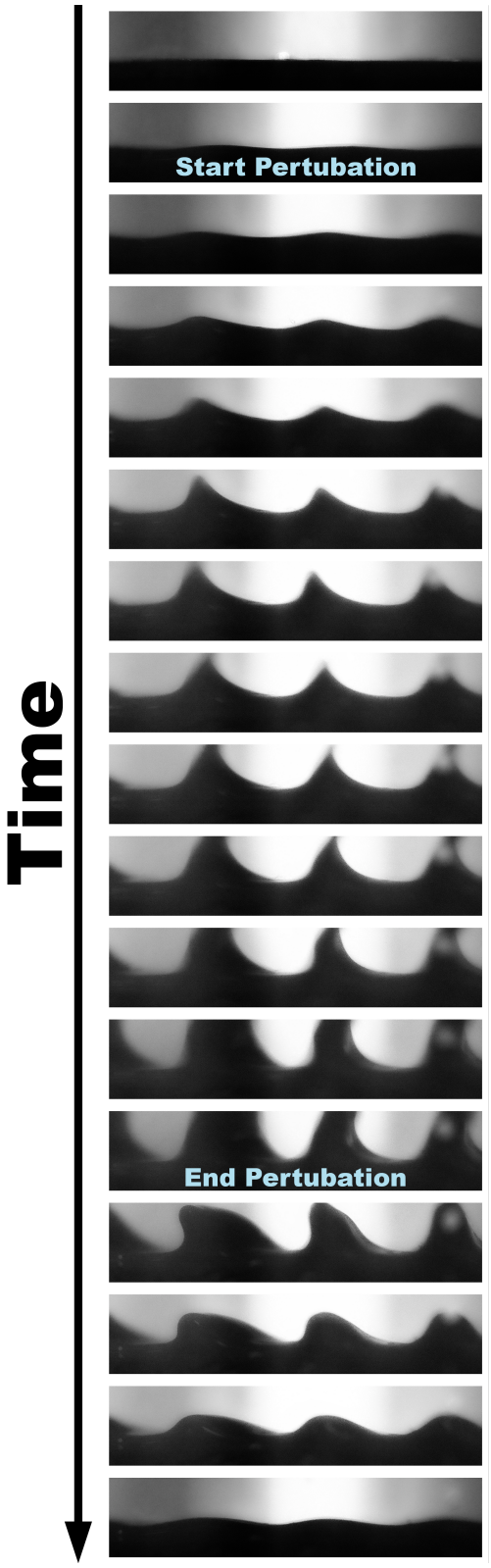

Figure 4.18. Oscillatory Kelvin-Helmholtz Instability evolution. Spatio-temporal evolution of the PDMS-Acetone interface when an oscillatory and sinusoidal perturbation forces the system.

4.1.5 Oscillatory Kelvin-Helmholtz Instability Inviscid Theory

The inviscid theory is applicable for modeling the Oscillatory Kelvin-Helmholtz instability, which is the fundamental mechanism underlying the emergence of the new fingers instability.

Kelly [26] and Lyubimov and Chereponov [27] developed inviscid theories that predict an instability characterized by a threshold in relative velocity between the two overlapped fluids and a most unstable wavenumber mode identical to the classical Kelvin-Helmholtz instability. The theory was initially formulated to address the interface between two immiscible fluids with comparable densities and supposed inviscid, overlapped within a vessel, and that experience disturbance due to horizontal vibrations [27]. This concept is reintroduced here in the context of miscible interfaces and oscillatory flow.

Considering the system reported in Figure 4.19a, the inviscid theory predicts, when a wave relief develops at the interface due to a vibration field with amplitude a and frequency f, the characteristic wavelength as

$$\lambda_{cap} = 2\pi\sqrt{\frac{\sigma}{(\rho_1 - \rho_2)g}} \tag{4.1}$$

namely the capillary wavelength, where σ is the interfacial tension, $\rho_1 - \rho_2$ the density difference between the to fluids and g the gravitational acceleration. Therefore, the most unstable inviscid wavenumber can be defined as

$$k_{cr,inv} = 2\pi/\lambda_{cap} \tag{4.2}$$

The marginal stability curve that predicts the limits for amplitude and frequency of vibration

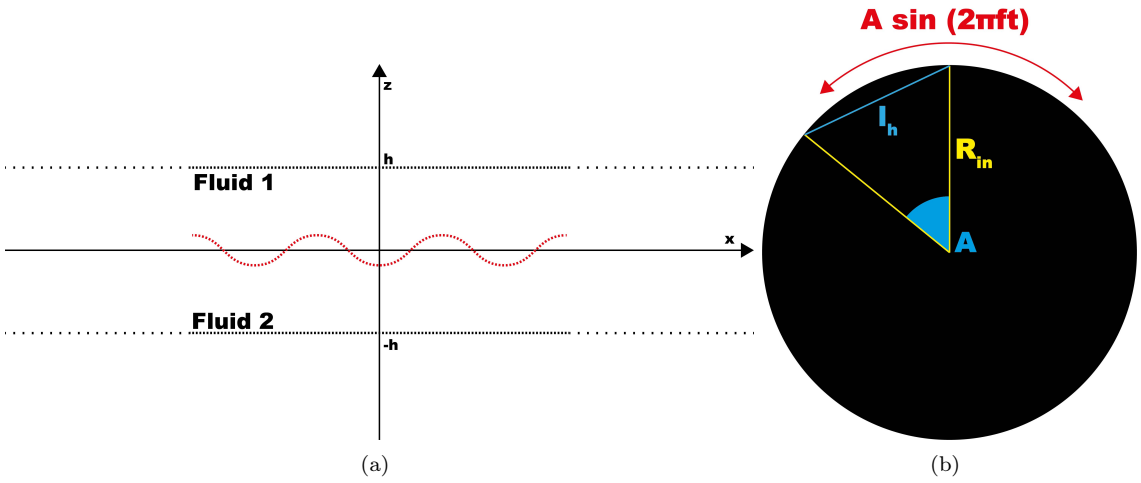

(a) (b)

Figure 4.19. Oscillatory Kelvin-Helmholtz Instability model sketch. Vibration flow in semi-infinite fluid layers. The two fluids are assumed to be inviscid and the configuration is gravitationally stable. **b)** The distance traveled along a curved trajectory and that along a linear trajectory ($l_h = 2R_{in}\ sin\ (A/2)$) differ by less than 0.1% due to the small amplitude of oscillation, A. This motion can be considered analogous to horizontal vibration.

rate is

$$(af)^2_{cr,inv} = \frac{(\rho_1+\rho_2)^3}{2\rho_1\rho_2(\rho_1-\rho_2)}\left[\frac{\sigma g}{(\rho_1-\rho_2)}\right]^{1/2} \tag{4.3}$$

The conditions for applying this theory are $f >> a\ L^2$ and $a << L$, where L is the characteristic length of the waves relief, and they are satisfied, assuming the amplitude of the vibrations small and the vibration frequency significant.

To facilitate a direct comparison between the vibrational field and the sinusoidal perturbation applied in this context, it is essential to compare the oscillatory flow with the horizontal flow.

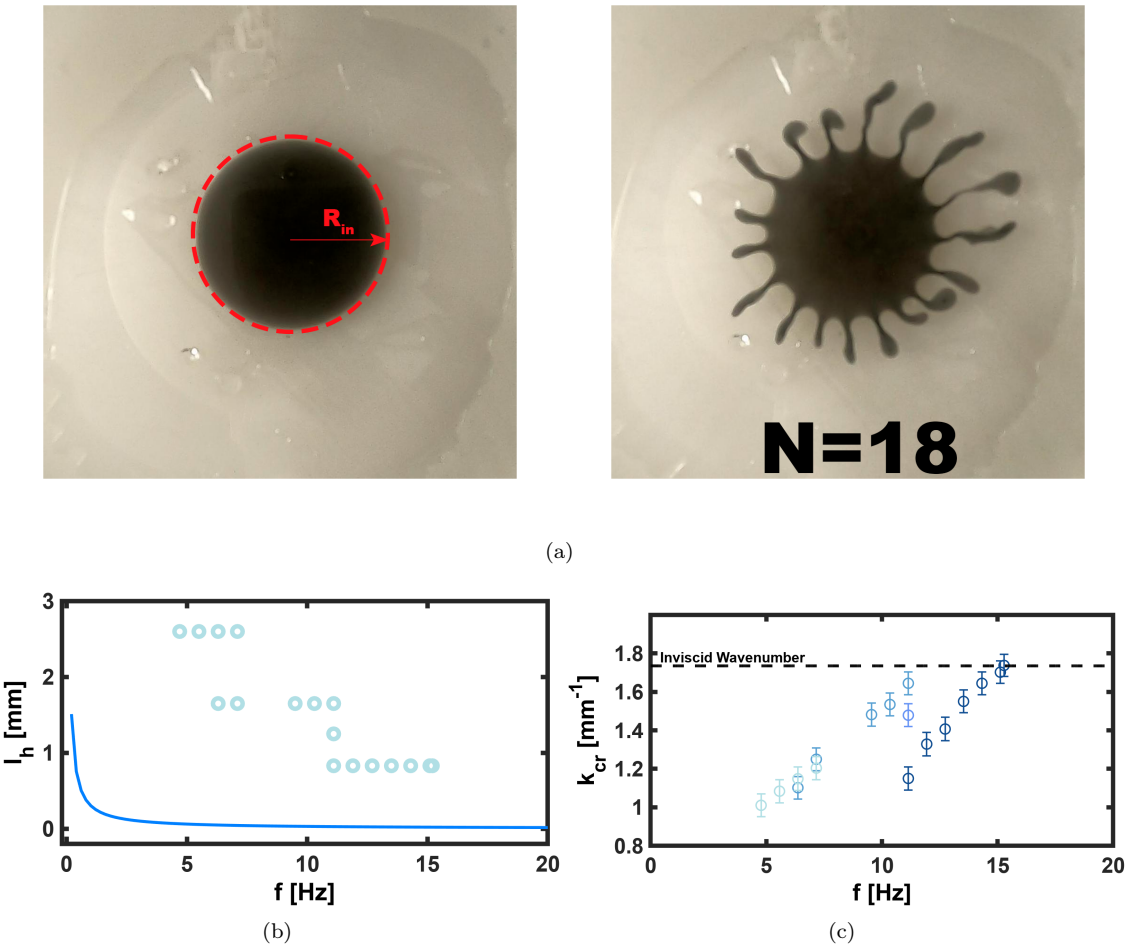

Figure 4.20. Oscillatory Kelvin-Helmholtz instability inviscid theory. a) The variable R represents the initial radius, which is the distance of the PDMS layer edge from its center (left). N stands for the number of fingers, corresponding to the count of waves formed during the occurrences of the Oscillatory Kelvin-Helmholtz instability (right). **b)** Stability diagram. *Legend:* $(l_h f)^2_{cr,inv} = \frac{(\rho_1+\rho_2)^3}{2\rho_1\rho_2(\rho_1-\rho_2)}\left[\frac{\sigma g}{(\rho_1-\rho_2)}\right]^{1/2}$, Experimental runs. **c)** Comparing the critical experimental wavenumber with the inviscid value. The critical experimental wavenumber is defined as $k_{cr,exp} = N/R_{in}\ [1/mm]$, while the critical inviscid wavenumber is $k_{cr,inv} = 2\pi/\lambda_{cap}\ [1/mm]$(dotted lined), where $\lambda_{cap} = 2\pi\sqrt{\sigma/(\rho_1-\rho_2)g}\ [mm]$. *Legend*: $k_{cr,exp}$ for $A = 0.05\ rad$, $A = 0.07\ rad$, $A = 0.1\ rad$, $A = 0.16\ rad$.

The sinusoidal motion $\Omega = A\ sin\ 2\pi ft$ can be compared to the horizontal motion under the assumption that the oscillation angles are small, ensuring that the distance traveled along a curved trajectory is comparable to that along a linear trajectory. Upon calculating the linear trajectory $l_h = 2R_{in}\ sin\ (A/2)$, where R_{in} is the radius of the PDMS layer when the perturbation starts (see Fig. 4.19b) and the curved trajectory as $l_c = A \cdot R_i n$, it is observed that the difference is less than 0.1%. Experimental values of the most unstable wavenumber and the critical velocity ($(l_h f)^2$) will be compared with theoretical values to assess the agreement between observed and predicted outcomes. The most unstable experimental wavenumber, $k_{cr,exp}$, can be expressed as the ratio of the number of fingers formed (Fig. 4.20a (right image)), N, to the initial radius of the PDMS layer (see Fig. 4.20a (left image)), R_{in}. The new Hydrodynamic Fingers Instability is assumed to be related to the Oscillatory Kelvin-Helmholtz instability, and the number of fingers is considered to be equivalent to the number of waves resulting from this Kelvin-Helmholtz instability. Therefore, the expression for the most unstable experimental wavenumber is given by $k_{cr,exp} = N/R_{in}$ [17].

For each combination of oscillation amplitude and frequency employed in the experiments (refer to Section 3.1.4), ensure that $(l_h f)^2/\lambda_{exp} << v = (l_h f)^2$, where $\lambda_{exp} = k_{cr,exp}/2\pi$ represents the characteristic experimental wavelength of the Oscillatory Kelvin-Helmholtz instability. In Figure 4.20b, the stability diagram displays experimental data points exclusively situated within the unstable region delineated by Equation 4.3. Figure 4.20c presents a comparison between theoretical and experimental values for the most unstable wavenumber. Notably, the inviscid theory remains applicable in actual systems characterized by high frequencies and diminishing oscillation amplitudes. In such circumstances, the wavenumber converges towards the inviscid value, as described by [28].

By assuming the equivalence between the number of fingers and waves and employing the inviscid theory for modeling, it is demonstrated that the Kelvin-Helmholtz instability serves as the foundational mechanism for the emerging Hydrodynamic Fingers Instability.

4.1.6 Centrifugal Effect

In the scenario where a new hydrodynamic instability originates from the Oscillatory Kelvin-Helmholtz instability, the formation of radial finger-like structures is explained by the centrifugal effect, which is influenced by mass, namely the section on which the centrifugal force is acting. In Newtonian mechanics, the centrifugal effect is an inertial effect that appears to act on all objects when viewed in a rotating, non-inertial frame of reference. It results from the object's inertia and acts in a direction away from the center of rotation. In fluid dynamics, the centrifugal effect defines an outward force experienced by a fluid particle in a rotating system. This effect is a consequence of the inertia of the fluid particle and its tendency to move in a straight line. When a fluid is in rotational motion, its particles experience centrifugal forces. These forces act radially outward from the axis of rotation. Similarly to rotational motion, the centrifugal effect can also be observed

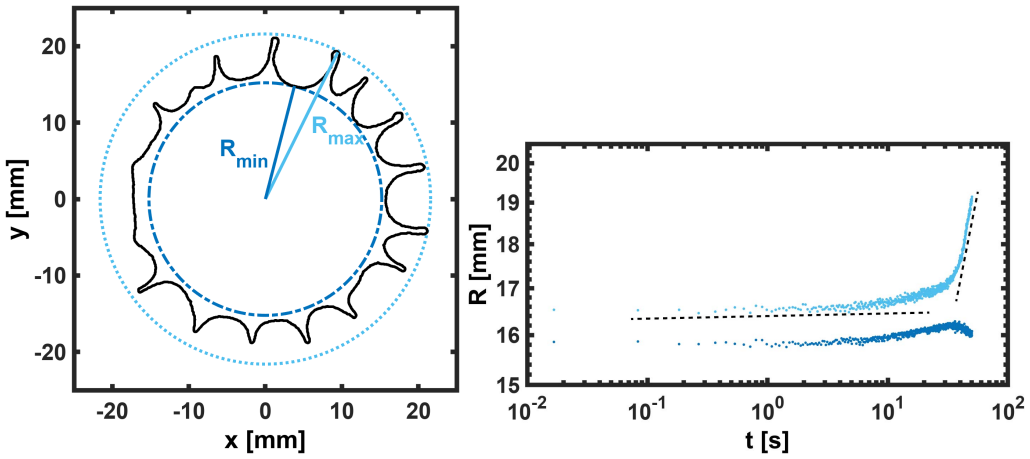

(a) (b)

Figure 4.21. Characteristic lengths for the Hydrodynamic Fingers Instability. a) The two radii, denoted as R_{max} and R_{min}, are defined as the distance from the PDMS layer center of the tip of the first finger formed and of the hollow between two subsequent fingers, respectively. The black line defines the PDMS layer edge. **b)** Radii evolution in time. As the radial size of the fingers increases, the region between them recedes radially. Oscillation amplitude $A = 0.05$ $[rad]$, angular frequency $\omega = 70$ $[rad/s]$. The dashed lines are a visual aid to indicate slopes. *Legend:* R_{max} $[mm]$, R_{min} $[mm]$.

in rotational oscillatory motion. The centrifugal effect manifests as a radial force experienced by fluid particles during the outward phase of the oscillation. The centrifugal force $F_c = f(m, \omega^2, r)$ is determined by the mass, m of the fluid it affects, the square of the angular frequency, ω^2, and the radial coordinate, r. The radial coordinate specifies the distance of the point at which the force is applied from the axis of rotation.

Herein, the centrifugal force exerted on the entire PDMS layer peaks at the radial coordinate of the contact line. Nevertheless, its impact is more significant in regions with larger waves, as the force is amplified by the greater mass of the fluid it acts upon. This gives rise to an azimuthal gradient of the centrifugal force, causing a net flow of PDMS in the radial direction and resulting in the formation and growth of finger-like structures.

To comprehend the phenomena occurring in PDMS-acetone systems, the growth of fingers is characterized by two specific lengths: the minimum and maximum radii. These radii, represented as R_{max} and R_{min} respectively, are defined as the distances from the center of the PDMS layer to the tip of the first formed finger and to the hollow between two successive fingers, as illustrated in Fig. 4.21a. Before the growth of fingers, R_{max} coincides with the radius of the circular PDMS layer, as explained in Section 4.1.3. Figure 4.21b provides an illustrative example of the typical evolution of both radii over time. As the radial dimensions of the fingers increase, the region between them retracts radially. This results in a more substantial impact of the centrifugal force on the tips of the formed fingers compared to the hollows between them, owing to the increasing radial coordinates of the finger tips.

In the context of dynamics, the maximum radius, R_{max}, changes its rate of increase due to

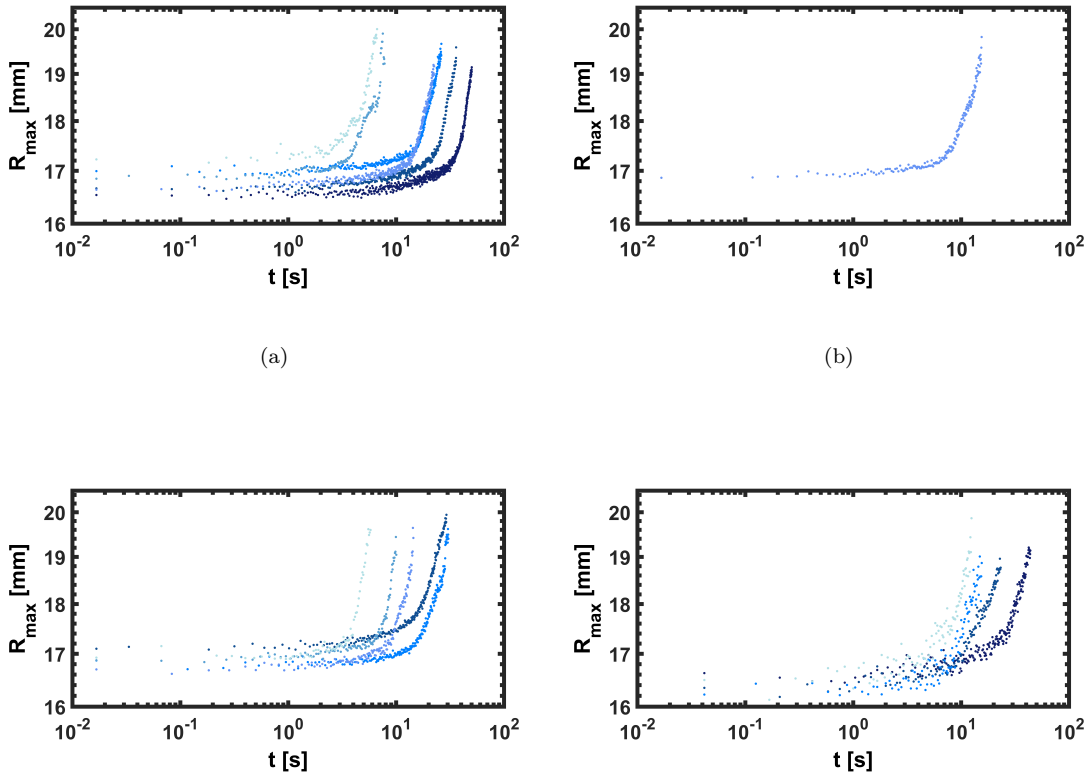

Figure 4.22. Dimensional temporal evolution of R_{max}: comparison at constant oscillation amplitude. Dimensional R_{max} as function of time for different oscillation amplitude: **a)** $A = 0.05$ $[rad]$ with $\omega = 70$ $[rad/s]$, $\omega = 75$ $[rad/s]$, $\omega = 80$ $[rad/s]$, $\omega = 85$ $[rad/s]$, $\omega = 95$ $[rad/s]$, $\omega = 96$ $[rad/s]$, **b)**$A = 0.07$ $[rad]$ with $\omega = 70$ $[rad/s]$, **c)** $A = 0.1[rad]$ with $\omega = 40$ $[rad/s]$, $\omega = 45$ $[rad/s]$, $\omega = 60$ $[rad/s]$, $\omega = 65$ $[rad/s]$, $\omega = 70$ $[rad/s]$ and **d)** $A = 0.16$ $[rad]$ with $\omega = 30$ $[rad/s]$, $\omega = 35$ $[rad/s]$, $\omega = 40$ $[rad/s]$, $\omega = 45$ $[rad/s]$.

two distinct processes outlined in Section 4.1.2. Initially, the first process involves a spreading phenomenon without forming fingers. During this phase, waves develop on the horizontal interface between PDMS and acetone. Subsequently, the maximum radius experiences accelerated growth due to increased influence from the centrifugal force acting on the tips of the formed fingers (dashed line in Fig. 4.21b). The alteration in slope is attributed to both the centrifugal effect and the change in the section on which the centrifugal force acts, resulting from the formation of waves. This departure is distinct from conventional spreading processes, like in spin coating, where centrifugal force uniformly acts on the entire vertical interface. In this scenario, a gradient in centrifugal force exists along the azimuthal direction. Hence, the slopes depend significantly on the angular frequency ω.

In Figure 4.22 and 4.23, the maximum radius is depicted as a function of time for various angular

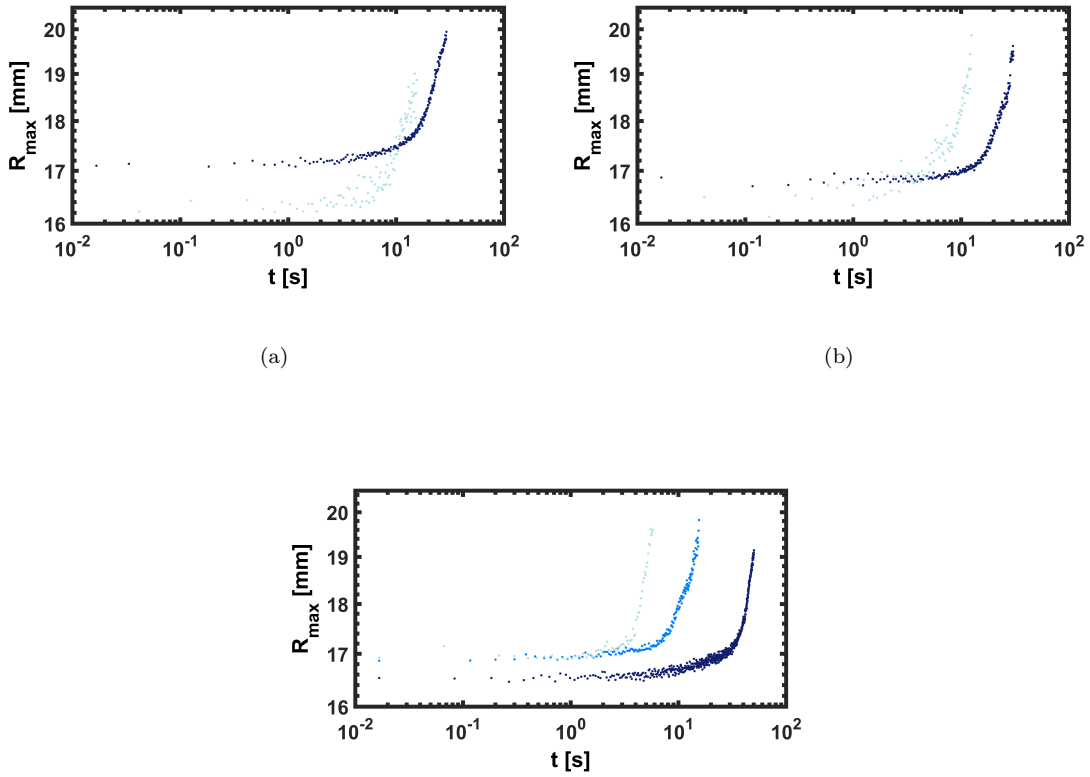

Figure 4.23. Dimensional temporal evolution of R_{max}: comparison at constant oscillation angular frequency. Dimensional R_{max} as function of time for different angular frequency: **a)** $\omega = 40\ [rad/s]$ with $A = 0.05\ [rad]$, $A = 0.16\ [rad/s]$, **b)** $\omega = 45[rad/s]$ with $A = 0.1\ [rad]$, $A = 0.16\ [rad/s]$, and **c)** $\omega = 70\ [rad/s]$ with $A = 0.05\ [rad]$, $A = 0.07\ [rad/s]$, $A = 0.1\ [rad/s]$.

frequencies and oscillation amplitude. The initial radius is held constant by carefully controlling the spreading phase before the perturbation initiation, as Section 4.1.3 outlines. Furthermore, the experimental error associated with the initial radius is limited to less than 5%, avoiding any effect of the initial condition. Observing the influence of changes in angular frequency while keeping the oscillation amplitude A constant reveals that the formation of waves and the growth of fingers occur more rapidly with an increase in angular frequency (Fig. 4.22a-b-c-d). The heightened angular velocity produces amplified shear stresses on the horizontal interface, making the wave formation quicker. Consequently, the centrifugal force also intensifies. As for alterations in oscillation amplitude, a similar effect to increasing angular velocity is observed, as indicated in Figure 4.23a-b-c. When the oscillation amplitude increases, the waves' formation and finger growth occur more rapidly.

Dimensionless parameters are required to account for the influence of centrifugal force. The

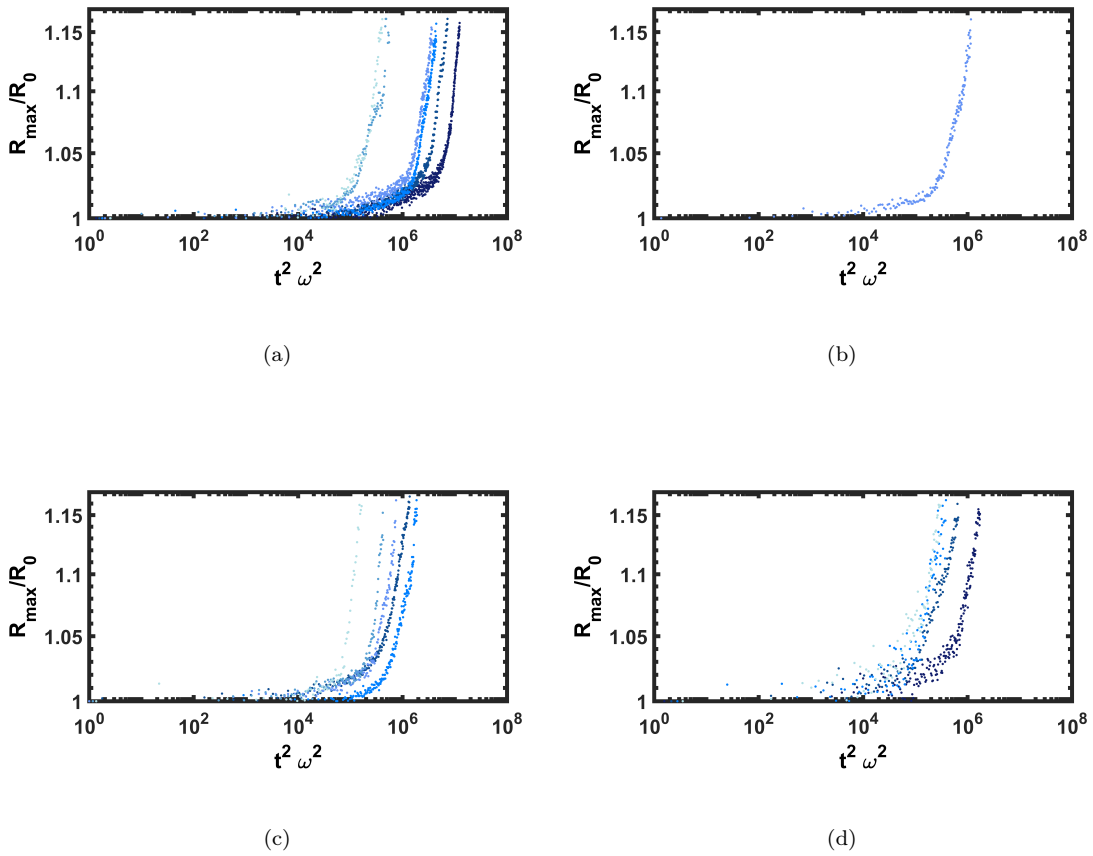

Figure 4.24. Dimensionless temporal evolution of R^*_{max}: comparison at constant oscillation amplitude. Dimensionless $R^*_{max} = R_{max}/R_0$, where R_0 is the PDMS layer radius when the perturbation starts, as a function of the square of the dimensionless time $t^{*2} \sim t^2\omega^2$ for different oscillation amplitude: **a)** $A = 0.05$ $[rad]$ with $\omega = 70$ $[rad/s]$, $\omega = 75$ $[rad/s]$, $\omega = 80$ $[rad/s]$, $\omega = 85$ $[rad/s]$, $\omega = 95$ $[rad/s]$, $\omega = 96$ $[rad/s]$, **b)** $A = 0.07[rad]$ with $\omega = 70$ $[rad/s]$, **c)** $A = 0.1$ $[rad]$ with $\omega = 40$ $[rad/s]$, $\omega = 45$ $[rad/s]$, $\omega = 60$ $[rad/s]$, $\omega = 65$ $[rad/s]$, $\omega = 70$ $[rad/s]$, and **d)** $A = 0.16$ $[rad]$ with $\omega = 30$ $[rad/s]$, $\omega = 35$ $[rad/s]$, $\omega = 40$ $[rad/s]$, $\omega = 45$ $[rad/s]$.

initial radius, R_0, serves as the characteristic length, while the characteristic time, determined by the imposed perturbation, corresponds to $1/\omega$, representing the period of oscillation (ignoring a 2π factor that does not impact the analysis). Consequently, the dimensionless maximum radius is denoted as $R^*_{max} = R_{max}/R_0$, and due to the dependence of centrifugal force on ω^2, the square of dimensionless time is represented by $t^{*2} \sim t^2\omega^2$.

As reported in Figs. 4.24 and 4.25, in dimensionless form, the negligible influence of initial conditions is wholly eliminated, and the scaled time renders all curves parallel. The slopes of each curve, whether representing spreading or finger growth, become identical, allowing the determination of the primary influence on finger growth and spreading phases attributable to centrifugal force.

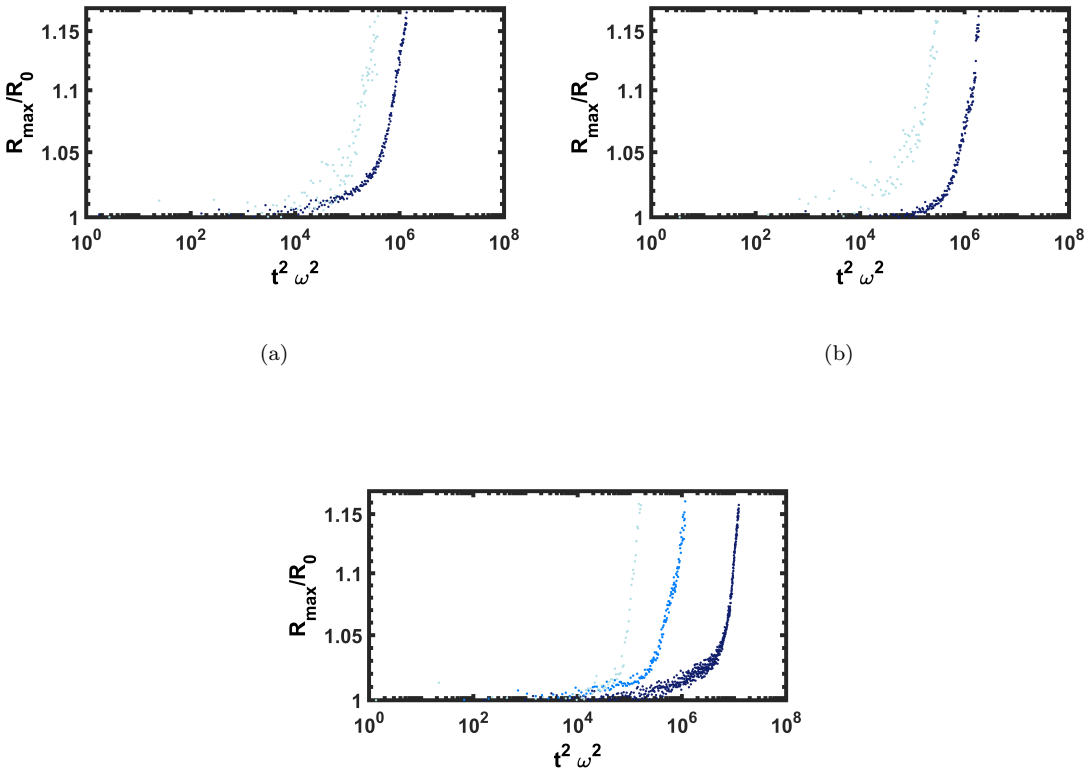

(a)

(b)

(c)

Figure 4.25. Dimensionless temporal evolution of R_{max}: comparison at constant oscillation angular frequency. Dimensionless $R^*_{max} = R_{max}/R_0$, where R_0 is the PDMS layer radius when the perturbation starts, as function of the square of dimensionless time $t^{*2} \sim t^2\omega^2$ for different angular frequency: **a)** $\omega = 40$ $[rad/s]$ with $A = 0.05$ $[rad]$, $A = 0.16$ $[rad/s]$, **b)** $\omega = 45$ $[rad/s]$ with $A = 0.1$ $[rad]$, $A = 0.16$ $[rad/s]$, and **c)** $\omega = 70$ $[rad/s]$ with $A = 0.05$ $[rad]$, $A = 0.07$ $[rad/s]$, $A = 0.1$ $[rad/s]$.

4.2 Thin Film Drainage

4.2.1 Surface Tension, Contact Angles and Bulk Viscosity Measurements

In the context of the experimental campaign, a comprehensive characterization of the systems was undertaken, encompassing the determination of equilibrium contact angles, surface tension, and bulk viscosity for water and aqueous suspensions of polystyrene particles. The equilibrium contact angles for water and the colloidal suspension on a glass substrate were quantified as $19.1 \pm 0.8°$ and $21.25 \pm 0.55°$, respectively. Notably, minimal variations in contact angle were observed in the presence of particles. The surface tension of the colloidal suspension, found to be $70.77 \pm 0.23\ mN/m$, exhibited similarity to the surface tension of water, irrespective of particle size and concentration. Additionally, the bulk viscosity of the polystyrene suspension was measured as $10^{-3}\ Pa \cdot s$, a crucial parameter for the evaluation of the global Reynolds number during the rising of bubbles.

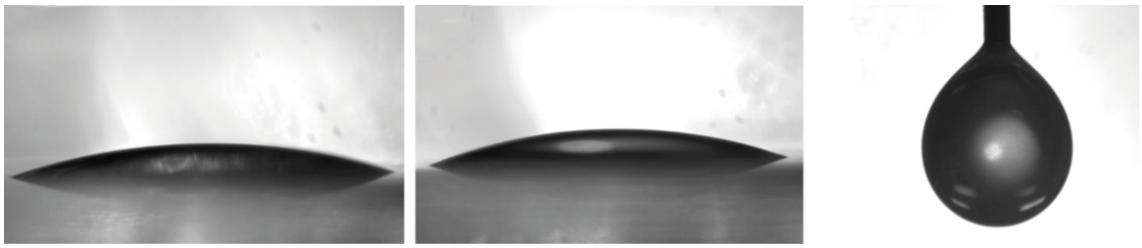

Figure 4.26. Contact Angle and Surface Tension. The equilibrium contact angle on glass substrate of *[left]* water, *[center]* suspension of PS and *[right]* surface tension of PS suspension.

4.2.2 Thin Film Drainage and Viscoelasticity

The discussion focuses on the dynamics of film drainage when bubbles collide with a glass substrate. The bubble's approach velocity V_a towards the solid surface in an aqueous medium was determined to be approximately $42.23\ mm/s$ through the analysis of captured side videos. The average radius R of the bubble was measured at $1.23\ mm$. The resulting approach velocity yields a global Reynolds number $Re = 2\rho R V_a/\eta$ of approximately 100, where $\rho = 1000\ kg/m^3$ is the density and $\eta = 10^{-3}\ Pa \cdot s$ is the dynamic viscosity of water. In polystyrene suspensions, the bubble approach velocity was slightly lower than that in the aqueous medium, measuring $38.08\ mm/s$. The collision between a bubble and a solid surface is characterized by the global Reynolds number [115, 118], contrasting with the film drainage analysis, which is appropriately characterized by the film Reynolds number $Re_f = \rho h_f V_f/\eta < 1$ [118]. Here, h_f is the characteristic film thickness, and V_f is the velocity of the film drainage. Notably, the film Reynolds number is considerably smaller than the global Reynolds number, making lubrication theory applicable to the analysis of

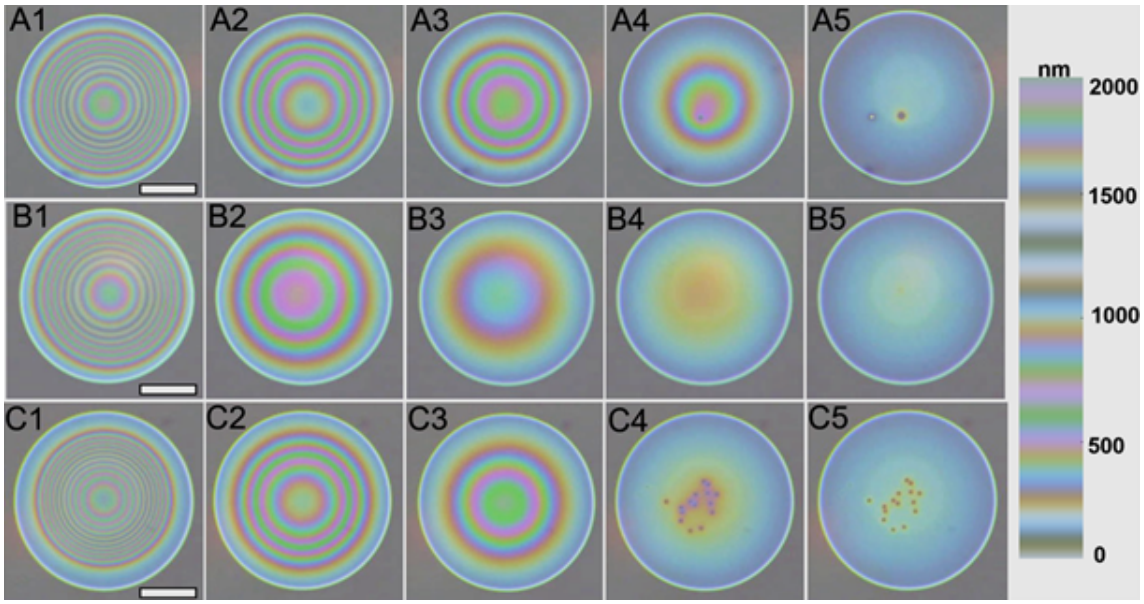

Figure 4.27. Experimental interferograms. The evolution of the film thickness during drainage was measured by analyzing the sequence of interferograms. Typical sequence of evolution of interferometric fringes (observed due to progression of drainage) for different experimental conditions; in water **(A1-A5)** and PS suspensions (0.15 mg/ml with two different diameters of 3 μm **(B1-B5)** and 0.6 μm **(C1-C5)**. Scale bar 100 μm.

film drainage. This approach reveals the spatial-temporal changes in film thickness over time.

The phenomenon of increasing pressure within an entrapped thin film as a rising bubble approaches a solid substrate is well-known. This process leads to the formation of a "dimple" resulting from the inversion of bubble curvature, where the pressure within the film begins to scale similarly to the internal pressure of the bubble $2\gamma/R$, where γ is the surface tension. The series of interferograms presented in Figure 4.27 illustrates the gradual drainage of the film and the corresponding changes in dimple thickness. These observations were made in water (A1-A5), as well as in PS suspensions (0.15 mg/ml) with two distinct particle diameters of 3 μm (B1-B5) and 0.6 μm (C1-C5) Notably, initially, slightly asymmetric films were formed due to the bubble's initial bouncing behavior, making it challenging to track the dimple formation. Therefore, Figure 4.27 depicts the spatial-temporal evolution of the entrapped film after the dimple's formation.

In Figure 4.28, the evolution of film profiles during film drainage are compared for different medium, as water (Figure 4.28a) and in polystyrene suspensions with different particle diameters, namely 3 μm(Figure 4.28b) and 0.6 μm (Figure 4.28c). The film thickness at the dimple center h_D and barrier ring h_{eq} of the bubbles in water and the two PS suspensions is presented in Figure 4.29. Figures 4.29a-c illustrate that the dimple thickness at the center decreases exponentially over time for various experimental conditions. Notably, the thickness at the barrier ring remains almost constant at approximately 150 nm throughout the drainage process for each experiment. Figure 4.29d depicts the film drainage at the center in different media, revealing that drainage occurs much faster in PS suspensions than in water. For instance, in water, it takes approximately 506

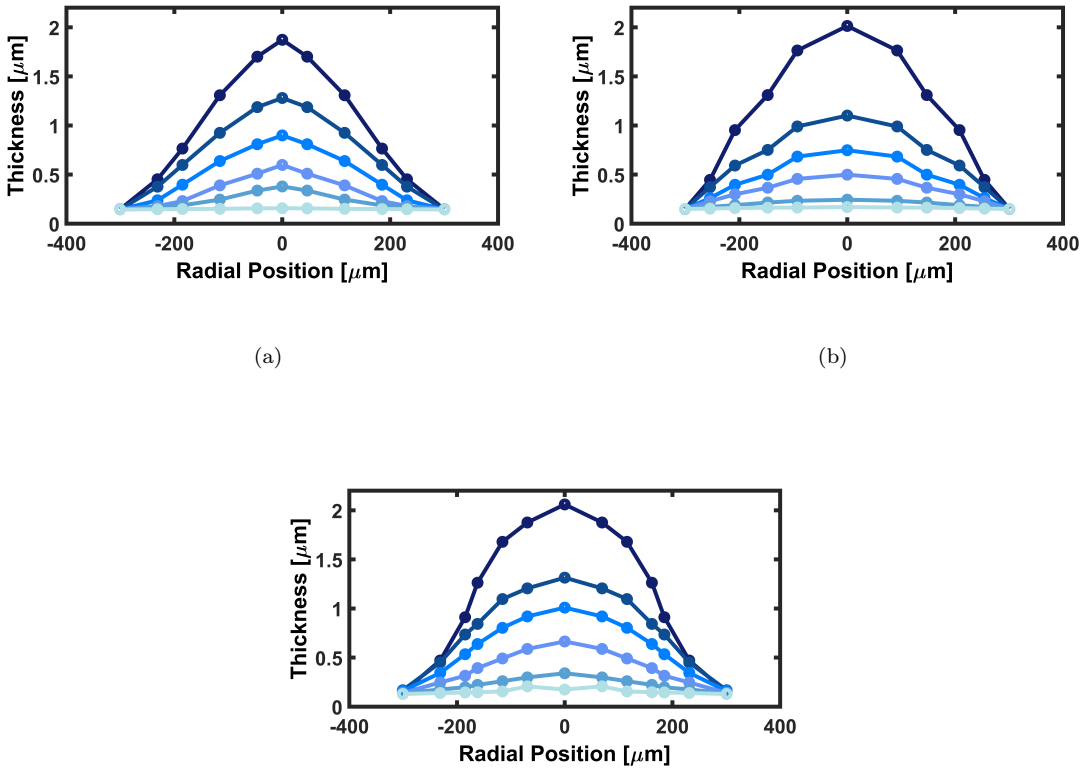

Figure 4.28. Dimple profile. The evolution of the axisymmetric shape of draining film thickness as a function of radial position in **a)** water, and suspension of PS particles (0.15 mg/ml) with diameters of **b)** 3 μm, and **c)** 0.6 μm.

seconds for the film (dimple) to become flat and reach equilibrium thickness. In PS suspensions with particle diameters of 3 μm and 0.6 μm, it takes approximately 275 seconds and 335 seconds, respectively. Interestingly, film drainage in the PS suspension with 0.6 μm particles is relatively slower than that for 3 μm particles, taking longer to reach equilibrium thickness. This may be attributed to the entrapment of smaller particles within the dimpled film. Figures 4.27 C4-C5 provide evidence that entrapped particles remain at the same location, sandwiched between the glass substrate and air-liquid interface, thereby slowing down film drainage in PS suspensions with smaller particles. In contrast, larger particles, with diameters exceeding the dimple thickness, are excluded from the dimple region.

The drainage dynamics are widely recognized to be influenced by hydrodynamic boundary conditions at both the glass surface and the air-liquid interface. At the glass surface $z = 0$, a no-slip boundary condition prevails, with the fluid velocity $v_r(z = 0, t$ being zero (immobile interface). Conversely, the boundary condition at the air-liquid interface varies depending on experimental factors. It may be either tangentially immobile, fully mobile (where the tangential

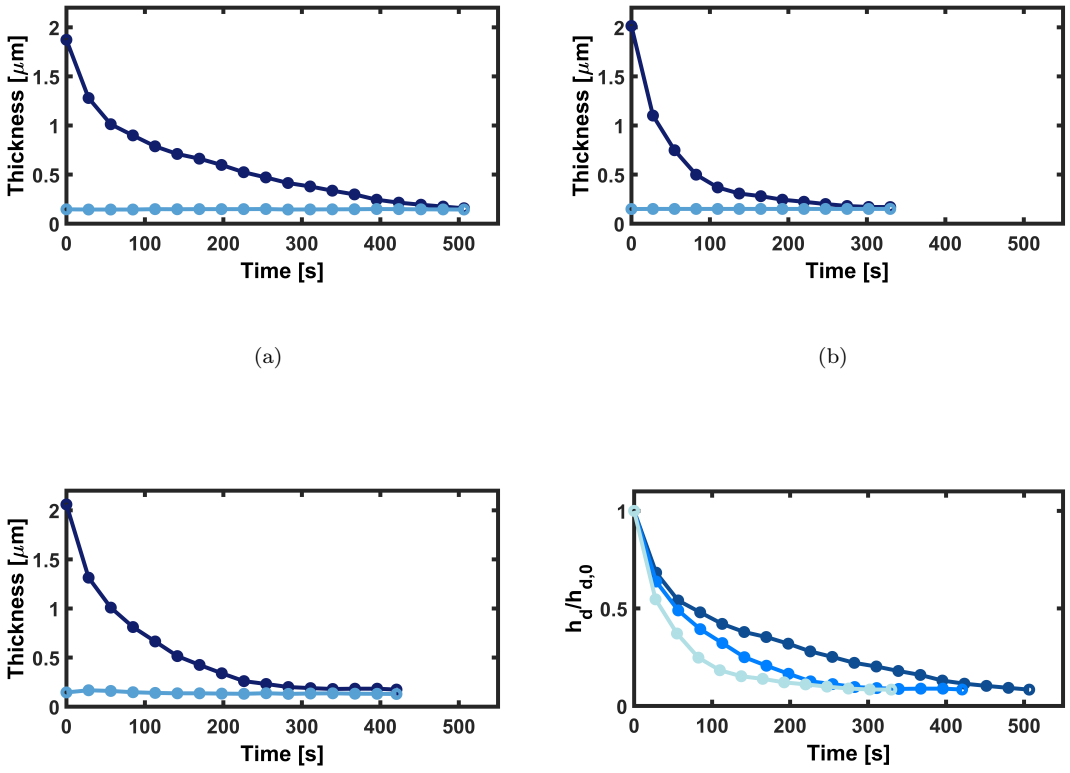

Figure 4.29. Temporal Evolution of thickness at the center and at the barrier ring. The evolution of the wetting film thickness at the center h_d and at the barrier rim h_{eq} as functions of time in different mediums **a)** water, and PS suspensions (0.15 mg/ml) with different diameters **b)** 3 μm, and **c)** 0.6 μm. **d)** The graph shows the comparison of film drainage at the center for different experimental conditions *Legend:* water, PS suspension with diameters of 3 μm and 0.6 μm

surface shear stress vanishes), or fall somewhere in between these extremes. Studies indicate that in the presence of surface contamination, the boundary at the bubble-water interface can become immobile, leading to a slow drainage of the water film [118, 136]. The small dot observed in Figure 4.27 A5 is attributed to impurities in the water, justifying the observed slow drainage. This observation aligns with previous studies. The intermediate or partially mobile boundary condition at the air-liquid interface is a result of surface elasticity or the presence of surface-active species [136]. Prior research has confirmed that film drainage becomes faster when a mobile boundary condition (zero tangential stress) operates at the bubble-liquid interface [118, 136]. In this study, a faster drainage in the PS suspensions was observed, attributing this to a shift in boundary conditions at the bubble-liquid interface.

Several previous theoretical and experimental studies have extensively explored the intricate behavior of film drainage, elucidating distinct effects through suitable assumptions. Notably, some

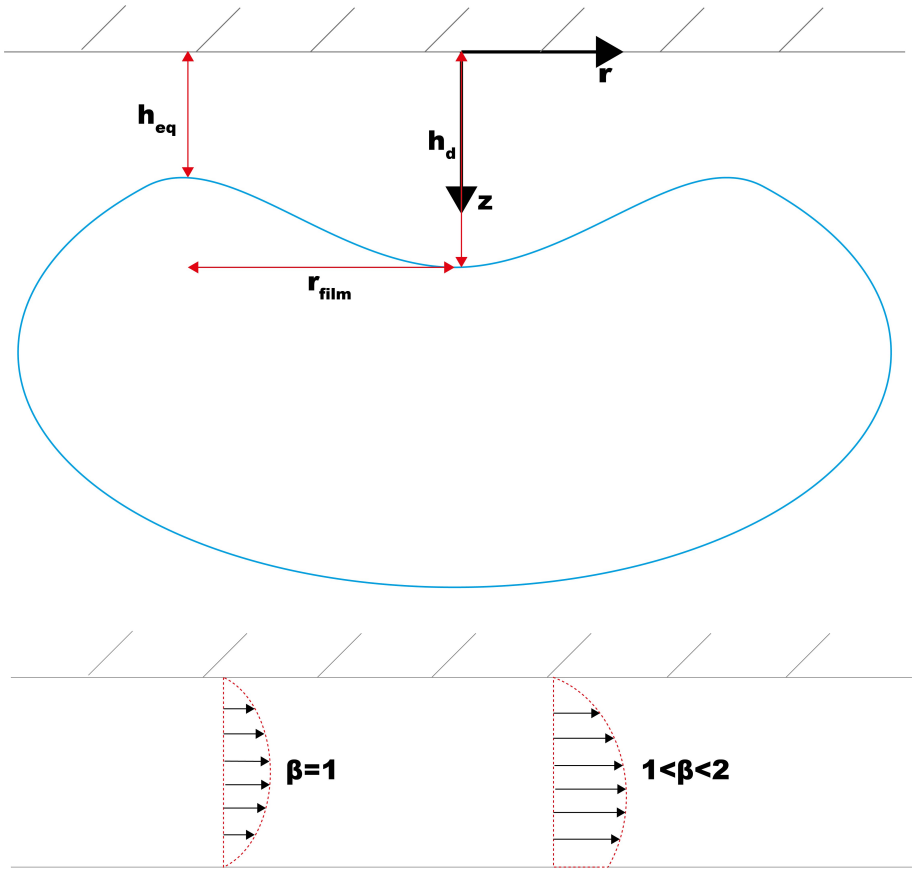

Figure 4.30. Dimple Sketch. Schematic of a dimple region of entrapped film between air bubble and glass substrate with different theoretical parameters; thickness at the center h_d, at the barrier ring h_{eq}, radius of the film r_{film}.

studies have focused on specific aspects, such as neglecting capillary pressure within a limited film thickness range [154, 155] or excluding the disjoining pressure [156, 157]. In Section 2.3.2 accurate equations by isolating the impact of film geometry from disjoining or capillary pressure are reported [149]. It is crucial to emphasize that the dimple's geometry is contingent upon the initial experimental conditions. The experimental findings previously reported, illustrating the exponential relaxation of the film (dimple) with a constant barrier film thickness, aligning with literature, particularly concerning the mixed regime of drainage dynamics [149]. In this mixed regime, film drainage at the edge (thinnest part) and at the center (thickest part) involves distinct effects—namely, disjoining and capillary pressure. Hence, the equations derived for film drainage in Section 2.3.2, within the background of the augmented Young-Laplace equation and lubrication approximation [140, 149], offer valuable insights into understanding the individual roles of capillary or disjoining pressure.

The film drainage has been categorized into three distinct regimes, each governed by different factors influencing film thickness. In the initial stage, referred to as the capillary regime, capillary pressure drives the drainage process as the film thickness is substantial, rendering the disjoining pressure negligible. Transitioning to the intermediate stage, known as the mixed regime, disjoining

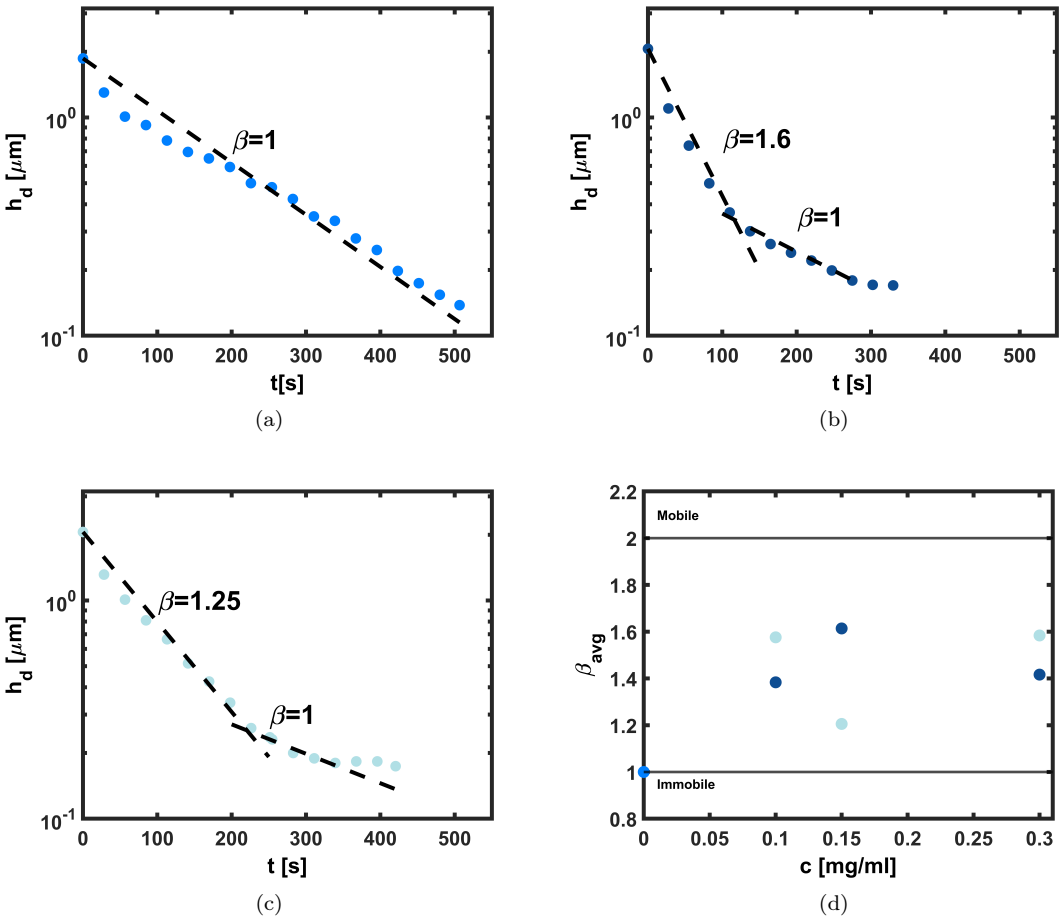

Figure 4.31. Dimple thickness temporal evolution. Semi-log plots show the change of film thickness at the dimple center h_d with time progression within different liquid mediums **a)** water, and in PS suspensions with different particle diameters; **b)** 3 μm and **c)** 0.6 μm. **d)** Average β_{avg} for different concentrations and diameters of PS particles, i.e., water, PS 3 μm and PS 0.6 μm.

pressure dominates at the thinnest section of the film (barrier ring), while capillary pressure controls the central region. In the final stage, as the film thickness and curvature reduce significantly, the drainage is primarily dictated by the disjoining pressure. Notably, our observations align with the mixed regime, where the central thick film diminishes exponentially over time, while the barrier rim maintains equilibrium film thickness (Figure 4.29). In the current study, the model reported in Section 2.3.2 for the mixed regime of drainage was employed to determine the parameter β that establishes the boundary condition at the air-liquid interface [149]. The dimple thickness temporal evolution for the system reported in Figure 4.30

$$h_d = h_{d,0} exp\left(-\frac{4}{9}\frac{\gamma h_{eq}^2}{\eta r_{film}^2}(3\beta - 2)t\right) \tag{4.4}$$

where $h_{d,0}$ is the initial dimple height and h_{eq} is the equilibrium thickness. At the barrier rim, $r = r_{film}$, the drainage process is predominantly influenced by the disjoining pressure. Equation

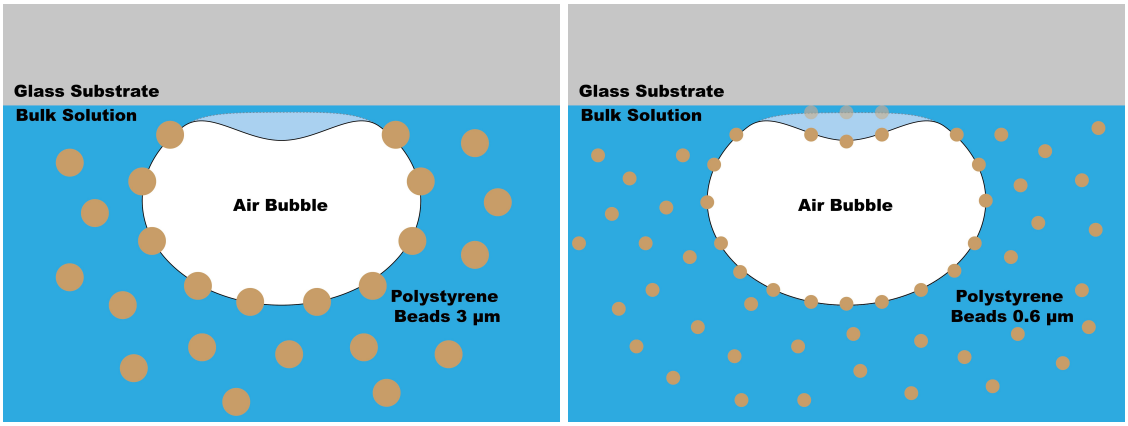

(a) (b)

Figure 4.32. Particles attachment. Schematic representation for decoration of PS particles on the surface of the bubble with different particle diameters; **a)** 3 μm (excluded from the dimple region), **b)** 0.6 μm (entrapped and sandwiched within the dimple). In lighter white, the equilibrium condition after film drainage.

4.4, utilized to quantify the parameter β, establishes the connection between the thickness at the center and its time derivative during the mixed regime of drainage [149].

In Figures 4.31, semi-log plots illustrate the evolution of film thickness at the center over time. To determine the parameter β, the experimental data were fitted using Eq. 4.4, with values of 1 and 2 indicating immobile and mobile boundaries at the air-liquid interface, respectively. The velocity profile shape for both cases is reported in Figure 4.30. In the absence of particles, film drainage in water reveals a tangentially immobile air-liquid interface (Fig. 4.31a), attributed to the development of Marangoni stresses induced by contaminants. Figures 4.31b-c depict calculated β values for film drainage in aqueous polystyrene suspensions (0.15 mg/ml) with particle diameters of 3 μm and 0.6 μm, respectively. The results show a transition from partially mobile to immobile behavior as particles are introduced, explaining the accelerated drainage with particle addition. Figure 4.31d presents the average β_{avg} for different PS particle concentrations and diameters, consistently falling within the range $1 < \beta_{avg} < 2$, confirming a partially mobile boundary at the air-liquid interface in PS suspensions.

The mobility of the boundary nature at the air-liquid interface in polystyrene suspensions, which becomes decorated with PS particles as sketched in Figure 4.32, as opposed to its immobility in water, prompts an investigation into the interfacial rheology. Previous studies have established that hydrophobic PS particles tend to accumulate at the air-water interface, forming an organized layer [146, 148]. An increase in surface elasticity as the coverage of the PS monolayer intensified, attributing this to the transition from weak electrostatic interactions (low coverage, low elasticity) to strong hydrophobic attraction (high coverage, high elasticity) at the interface, were observed [158]. Film drainage dynamics are significantly influenced by surface viscoelasticity, which renders the interface mobile until a certain point, which becomes immobile due to viscous effects [134]. In

the PS suspension experiments reported here, the migration and layering of PS particles on the bubble's surface alter the air-liquid interface's rheological properties, introducing elasticity and inducing a mobile behavior, resulting in faster drainage. Figure 4.31a-b illustrates an exponential decay of film thickness at the center over time, with two distinct regimes of drainage. The initial, faster drainage corresponds to the partially mobile boundary ($1 < \beta < 2$), possibly due to the initial elastic nature of the particle-decorated bubble surface. The subsequent slow drainage regime is attributed to the re-establishment of viscous effects, leading to an immobile boundary at the air-liquid interface ($\beta = 1$). The measurement of surface tension in the presence of PS particles, which was found to be the same as that of water, suggests the presence of low Marangoni stresses at the air/liquid interface, with the effect of Gibbs elasticity excluded. Notably, film drainage is comparatively slower in PS suspensions with smaller particles due to particle entrapment within the dimple, while larger particles are excluded from the entrapped film, resulting in faster drainage.

Conclusion

The investigation presented herein pertains to the examination of two limit cases, particularly within the context of miscible fluid dynamics. A novel destabilization scenario leading to the formation of fingers in a layered system comprising PDMS and acetone has been discovered. This destabilization arises from shear stresses induced by the imposition of sinusoidal rotational forces, resulting in an oscillatory Kelvin-Helmholtz-type instability. The observed phenomenon manifests as a distinctive dynamic wherein, as the pattern of waves attains a critical height, centrifugal forces give rise to protrusions along the contact line of the PDMS. This process leads to a loss of axial symmetry. Due to variations in the film's cross-sectional profile, an azimuthal gradient of centrifugal force emerges. The centrifugal force attains a greater magnitude where wave height is increased, fostering the growth of protrusions and ultimately forming fingers. In the context of miscible systems, the dissertation contributes new evidence supporting the importance of interfacial phenomena. This dynamic represents a hitherto unreported scenario in the scientific literature, constituting a significant contribution to the limited body of knowledge surrounding miscible interfaces.

Furthermore, the investigation delves into the realm of thin film drainage, reporting a comparative analysis of the drainage dynamics of liquid films confined between a glass substrate and an air bubble in both water and hydrophobic polystyrene (PS) colloidal suspensions. Notably, the drainage process is found to be more rapid in PS colloid suspensions when compared to water. The efficiency of film drainage is strongly influenced by the characteristics of the interfaces involved. A mobile interface facilitates faster drainage, contrasting with the slower drainage observed in tangentially immobile interfaces. In the case of water, surface contaminations render the air-water interface immobile, contributing to the deceleration of film drainage. Conversely, in PS colloidal suspensions, the air-liquid interface becomes partially mobile, leading to an accelerated film drainage process. The transition from an immobile to a partially mobile interface at the air-liquid boundary is attributed to surface elasticity. The presence of a layer of hydrophobic polystyrene particles on the bubble surface imparts elastic properties, rendering the air-liquid interface tangentially mobile and facilitating faster drainage. Significantly, the study demonstrates that the formation of a PS particle layer at the bubble surface transforms the interface into an elas-

tic state, promoting tangential mobility and expediting drainage. Intriguingly, the film drainage process is also influenced by the particle diameter of the PS suspensions. Films in PS suspensions with smaller particles exhibit a relatively slower flattening of dimpled films compared to their counterparts with larger particles. This delay is attributed to the entrapment of smaller particles within the dimple, holding liquid and impeding the drainage process. This dissertation introduces a further exploration into factors influencing the drainage of a film, contributing a pivotal piece to the comprehension of the physics underlying bubble-particle interactions.

In both projects, robust experimental control of the studied dynamics has been achieved, yielding data consistent with existing theoretical models. Naturally, there is room for improvement; specifically, for miscible fluids, a theory accounting for the viscosity difference between the two fluids or confinement within a container could be employed, although the inviscid theory provides sufficient evidence. Regarding thin films, the analysis could be extended to the bouncing phase before the establishment of a stationary dimple, enhancing the experimental setup using a high-speed camera to capture the rapid event.

Concluding, this dissertation thus not only expands the current understanding of miscible interfaces but also sets the stage for a new research paradigm exploring the application of hydrodynamic instability in diverse contexts, such as drop formation. These findings highlight the pivotal influence of interfacial features across diverse phenomena and length scales, enriching our understanding of fundamental principles and offering insights with practical implications in numerous fields.

Appendix

A.1 Rotational sinusoidal motion: Arduino Code for Stepper Motor

```
int dirpin = 10;
int steppin = 9;
static int current_position = 0 ;
int intended_position = 0;
int A=400;
int omega=50;
void setup()

{
  Serial.begin(115200);

  pinMode(dirpin, OUTPUT);
  pinMode(steppin, OUTPUT);
}
void loop ()
{
  intended_position =   (round (A * sin (omega*millis() / 1000.0)))
      ;

  while (intended_position != current_position)
  {
    bool direction = intended_position > current_position ;
    digitalWrite (dirpin, direction) ;
    digitalWrite (steppin, HIGH) ;
```

```
24      delayMicroseconds (1) ;
25      digitalWrite (steppin, LOW) ;
26      current_position += direction ? +1 : -1 ;
27    }
28 }
```

A.2 Image Processing and Edge Detection: MATLAB® Code

```
clear all
clc

%images upload on matlab
directoryRead = 'folder';
files = dir([directoryRead '/*.jpg']);
for i=1:length(files)
images{i} = imread([directoryRead '/' files(i).name]);  %array with
    images original
end

%images cropping
for i=1:length(images)
[ny(i),nx(i),dim(i)]=size(images{i});
deltaCrop=500;
C = round([nx(i) ny(i) ]/2);
Images{i}=imcrop(images{i},[C(1)-deltaCrop C(2)-deltaCrop 2*
   deltaCrop 2*deltaCrop]);
end

%Reading Background Image (for linear filter)
directory = 'folder';
files = dir([directory '/*.jpg']);
I=imread([directory '/' files.name]);

%Opening background
se = strel('disk',100);
background = imopen(I,se);
bwBackground = rgb2gray(background);
```

```
%Image Processing

for i=1:length(Images)

%RGB to Grayscale
grayImages{i}=rgb2gray(Images{i});

%Linear filter
minusImages{i}=grayImages{i}-0.5*bwBackground;

%Contrast Enhancement
conImages{i} = imadjust(minusImages{i},[0.01 0.35]);

%Binarization
binImages{i}=imbinarize(conImages{i},"adaptive",'ForegroundPolarity
    ','dark');

%Complement Images
binImages_com{i}=imcomplement(binImages{i});

%Images Opening
se=strel('disk',3);
binImages_open{i}= imopen(binImages_com{i},se);

%Area filtering to keep only black spot region
binImages_final{i}=bwareafilt(binImages_open{i},1);
end

%Edge Detection
for i=1:length(Images)
border{i} = edge(binImages_final{i},'Sobel');
overlappedImages{i}=imoverlay(ImagesO{i},border{i},[.3 1 .3]);
end
```

A.3 3D-Printed setup components CAD

Figure A.1. CAD. Optical table rod.

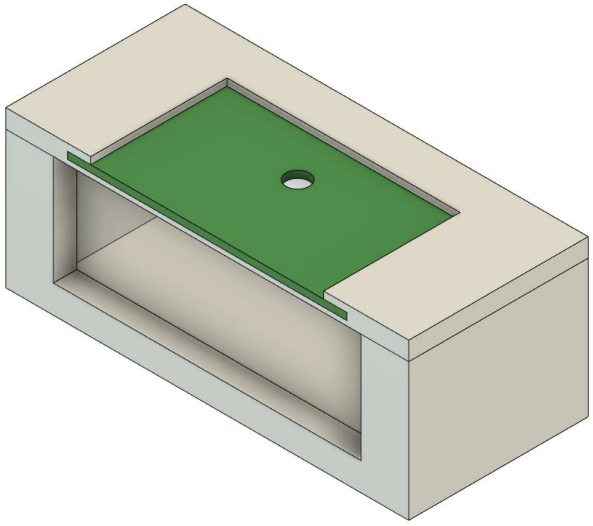

Figure A.2. CAD. Chamber for two fluids in Pendant Drop Method setup.

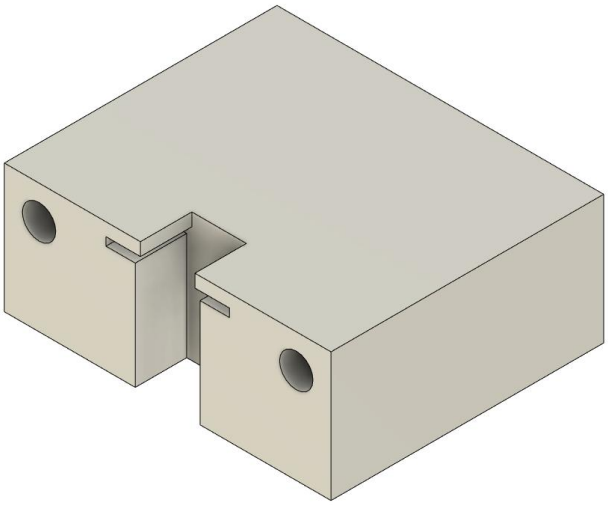

Figure A.3. CAD. Syringe holder for Pendant Drop Method setup

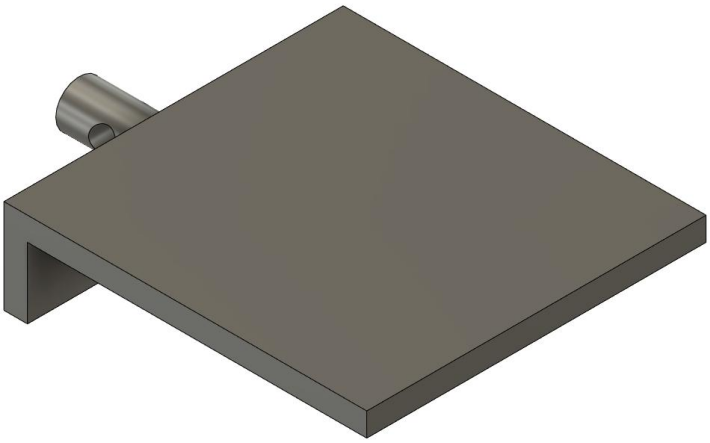

Figure A.4. CAD. Support for the anti-vibration system.

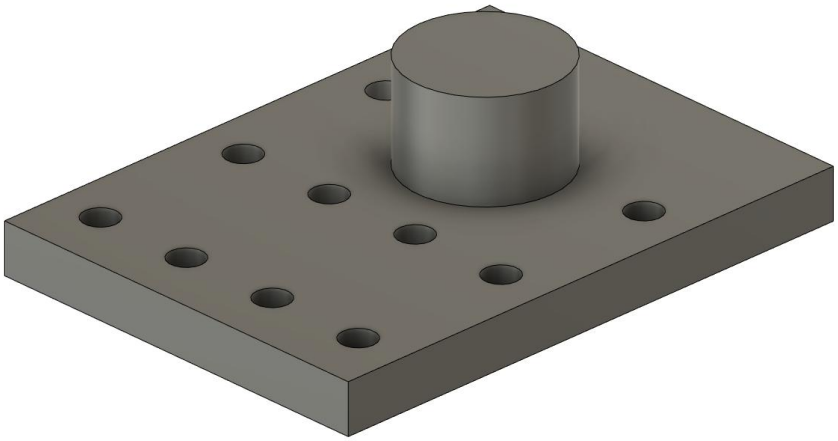

Figure A.5. CAD. Generic support.

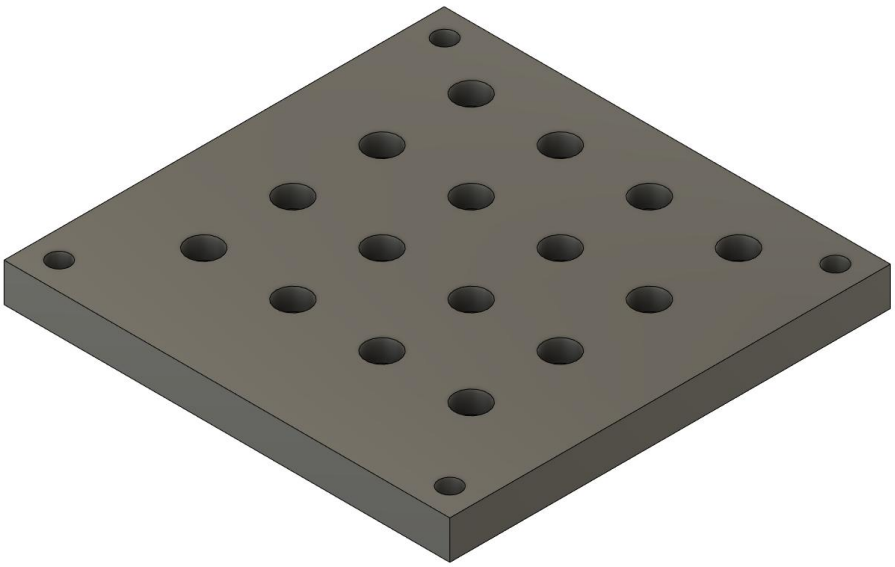

Figure A.6. CAD. Generic support.

Figure A.7. CAD. Support for integral camera.

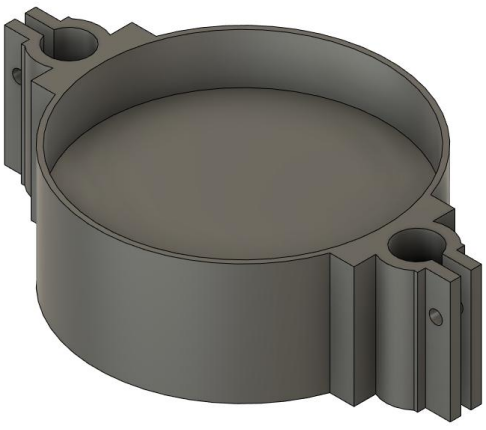

Figure A.8. CAD. Support for glass enclosure connection with stepper motor.

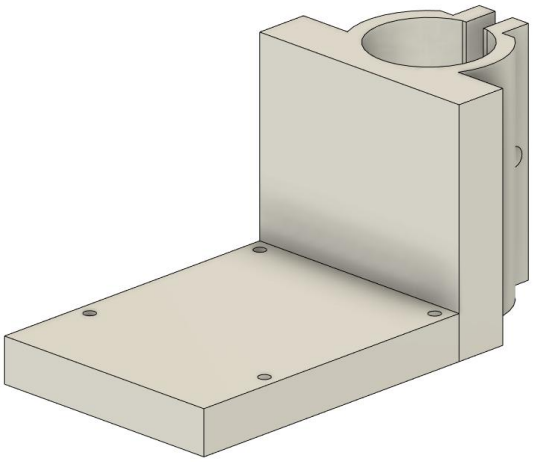

Figure A.9. CAD. Generic holder.

Bibliography

[1] Rowlinson J. S. "Translation of J. D. van der Waals' "The thermodynamik theory of capillarity under the hypothesis of a continuous variation of density"". In: *Journal of Statistical Physics* 20 (1979), pp. 197–200. DOI: 10.1007/BF01011513.

[2] Lord Rayleigh. "XX. On the theory of surface forces. —II. Compressible fluids". In: *The London, Edinburgh, and Dublin Philosophical Magazine and Journal of Science* 33 (201 Feb. 1892), pp. 209–220. DOI: 10.1080/14786449208621456.

[3] John W. Cahn and John E. Hilliard. "Free Energy of a Nonuniform System. I. Interfacial Free Energy". In: *The Journal of Chemical Physics* 28 (2 1958), pp. 258–267. DOI: 10.1063/1.1744102.

[4] Domenico Truzzolillo and Luca Cipelletti. *Off-equilibrium surface tension in miscible fluids*. 2017. DOI: 10.1039/C6SM01026A.

[5] Josiah Willard Gibbs. "On the equilibrium of heterogeneous substances". In: *American Journal of Science and Arts* s3-16 (1878), pp. 441–458. DOI: 10.2475/ajs.s3-16.96.441.

[6] Pierre-Gilles de Gennes, Françoise Brochard-Wyart, and David Quéré. *Capillarity and Wetting Phenomena*. Springer New York, 2004. DOI: 10.1007/978-0-387-21656-0.

[7] Vladimir S Ajaev. *Interfacial Fluid Mechanics: A Mathematical Modeling Approach*. Springer, 2012. DOI: 10.1007/978-1-4614-1341-7.

[8] Dominique Langevin. *Emulsions, Microemulsions and Foams*. Springer, 2020. DOI: 10.1007/978-3-030-55681-5.

[9] Arthur. W. Adamson and Gast. Alice. P. *Physical chemistry of surfaces*. 6th Edition. Interscience publishers New York, 1997. ISBN: 978-0-471-14873-9.

[10] Sina Ebnesajjad. "Surface tension and its measurement". In: *Handbook of adhesives and surface preparation*. Elsevier, 2011, pp. 21–30.

[11] J. Porter et al. "A review of fluid instabilities and control strategies with applications in microgravity". In: *Mathematical Modelling of Natural Phenomena* 16 (2021). ISSN: 17606101. DOI: 10.1051/mmnp/2021020.

[12] Helmholtz. "XLIII. On discontinuous movements of fluids". In: *The London, Edinburgh, and Dublin Philosophical Magazine and Journal of Science* 36.244 (1868), pp. 337–346. DOI: 10.1080/14786446808640073.

[13] William Thomson. "XLVI. Hydrokinetic solutions and observations". In: *The London, Edinburgh, and Dublin Philosophical Magazine and Journal of Science* 42.281 (1871), pp. 362–377. DOI: 10.1080/14786447108640585.

[14] Subrahmanyan Chandrasekhar. *Hydrodynamic and hydromagnetic stability*. Courier Corporation, 2013.

[15] E E Meshkov. "Instability of the interface of two gases accelerated by a shock wave". In: *Fluid Dynamics* 4 (1969), pp. 101–404. DOI: 10.1007/BF01015969.

[16] Robert D. Richtmyer. "Taylor instability in shock acceleration of compressible fluids". In: *Communications on Pure and Applied Mathematics* 13.2 (1960), pp. 297–319. DOI: 10.1002/cpa.3160130207.

[17] Harunori N. Yoshikawa and José Eduardo Wesfreid. "Oscillatory Kelvin-Helmholtz instability. Part 2. An experiment in fluids with a large viscosity contrast". In: *Journal of Fluid Mechanics* 675 (May 2011), pp. 249–267. ISSN: 14697645. DOI: 10.1017/S0022112011000152.

[18] "Oscillatory Kelvin-Helmholtz instability. Part 1. A viscous theory". In: *Journal of Fluid Mechanics* 675 (May 2011), pp. 223–248. ISSN: 14697645. DOI: 10.1017/S0022112011000140.

[19] A A Ivanova, V G Kozlov, and P Evesque. "Interface Dynamics of Immiscible Fluids under Horizontal Vibration". In: *Fluid Dynamivs* 36 (3 2001), pp. 28–35. DOI: 10.1023/A:1019223732059.

[20] Z Alterman. "Effect of surface tension on the Kelvin-Helmholtz instability of two rotating fluids". In: *Proceedings of the National Academy of Sciences* 47 (2 1961), pp. 224–227. DOI: 10.1073/pnas.47.2.224.

[21] Shreyas V. Jalikop and Anne Juel. "Steep capillary-gravity waves in oscillatory shear-driven flows". In: *Journal of Fluid Mechanics* 640 (2009), pp. 131–150. ISSN: 14697645. DOI: 10.1017/S0022112009991509.

[22] Emma Talib, Shreyas V. Jalikop, and Anne Juel. "The influence of viscosity on the frozen wave instability: Theory and experiment". In: *Journal of Fluid Mechanics* 584 (2007), pp. 45–68. ISSN: 14697645. DOI: 10.1017/S0022112007006283.

[23] D. V. Lyubimov et al. "Viscosity effect on the longwave instability of a fluid interface subjected to horizontal vibrations". In: *Journal of Fluid Mechanics* 814 (Mar. 2017), pp. 24–41. ISSN: 14697645. DOI: 10.1017/jfm.2017.28.

[24] Linfeng Piao and Hyungmin Park. "Interfacial instability for droplet formation in two-layer immiscible liquids under rotational oscillation". In: *Journal of Fluid Mechanics* 924 (2021). ISSN: 14697645. DOI: 10.1017/jfm.2021.628.

[25] C K Shyh and B R Munson. "Interfacial Instability of an Oscillating Shear Layer". In: *Journal of Fluids Engineering* 108 (89 1986), pp. 89–92.

[26] R E Kelly. "The stability of an unsteady Kelvin-Helmholtz flow". In: *Journal of Fluid MEchanics* 22 (3 1965), pp. 547–560. DOI: 10.1017/S0022112065000964.

[27] D Vo Lyubimov and A A Cherepanov. "Development of a steady relief at the interface of fluids in a vibrational field". In: *Fluid Dynamics* 21 (6 1986), pp. 849–854. DOI: 10.1007/BF02628017.

[28] Y. A. Gaponenko et al. "Dynamics of the interface between miscible liquids subjected to horizontal vibration". In: *Journal of Fluid Mechanics* 784 (Nov. 2015), pp. 342–372. ISSN: 14697645. DOI: 10.1017/jfm.2015.586.

[29] E J Hinch. "A note on the mechanism of the instability at the interface between two shearing fluids". In: *J. Fluid Mech* 144 (1984), pp. 463–465. DOI: 10.1017/S0022112084001695.

[30] Régis Wunenburger et al. "Frozen wave induced by high frequency horizontal vibrations on a CO 2 liquid-gas interface near the critical point". In: *Physical review E* 59.5 (1999), p. 5440. DOI: doi.org/10.1103/PhysRevE.59.5440.

[31] V. G. Kozlov et al. "Stability of interface between liquids with high viscosity contrast in unevenly rotating cavity". In: *Journal of Physics: Conference Series* 1809 (1 Feb. 2021). ISSN: 17426596. DOI: 10.1088/1742-6596/1809/1/012022.

[32] P g Saffman. "Viscous fingering in Hele-Shaw cells". In: *Journal of Fluid Mechanics* 173 (1986), pp. 73–94. DOI: 10.1017/S0022112086001088.

[33] D A Reinelt and P G Saffman. "The penetration of a finger into a viscous fluid in a channel and tube". In: *SIAM Journal on Scientific and Statistical Computing* 6 (3 1985), pp. 542–561. DOI: 10.1137/0906038.

[34] Akhileshwar Singh, Yogesh Singh, and Krishna Murari Pandey. "Viscous fingering instabilities in radial Hele-Shaw cell: A review". In: *Materials Today: Proceedings* 26 (2019), pp. 760–762. ISSN: 22147853. DOI: 10.1016/j.matpr.2020.01.022.

[35] F. Melo, J. F. Joanny, and S. Fauve. "Fingering instability of spinning drops". In: *Physical Review Letters* 63 (18 1989), pp. 1958–1961. ISSN: 00319007. DOI: 10.1103/PhysRevLett.63.1958.

[36] Nathalie Fraysse and George M Homsy. "An experimental study of rivulet instabilities in centrifugal spin coating of viscous Newtonian and non-Newtonian fluids". In: *Physics of Fluids* 6 (4 1994), pp. 1491–1504. DOI: 10.1063/1.868263.

[37] Kristi E. Holloway et al. "Spreading and fingering in spin coating". In: *Physical Review E - Statistical, Nonlinear, and Soft Matter Physics* 75 (4 Apr. 2007). ISSN: 15393755. DOI: 10.1103/PhysRevE.75.046308.

[38] S m Troian et al. "Fingering Instabilities of Driven Spreading Films". In: *Europhysics Letters* 10 (1 1989), pp. 25–30. DOI: 10.1209/0295-5075/10/1/005.

[39] A. McIntyre and L. N. Brush. "Spin-coating of vertically stratified thin liquid films". In: *Journal of Fluid Mechanics* 647 (Mar. 2010), pp. 265–285. ISSN: 14697645. DOI: 10.1017/S002211200999259X.

[40] Subhadarshinee Sahoo, Akash Arora, and Pankaj Doshi. "Two-layer spin coating flow of Newtonian liquids: A computational study". In: *Computers and Fluids* 131 (June 2016), pp. 180–189. ISSN: 00457930. DOI: 10.1016/j.compfluid.2016.03.016.

[41] Subhadarshinee Sahoo, Ashish V. Orpe, and Pankaj Doshi. "Spreading dynamics of superposed liquid drops on a spinning disk". In: *Physics of Fluids* 30 (1 Jan. 2018). ISSN: 10897666. DOI: 10.1063/1.5002601.

[42] Mayuresh Kulkarni et al. "Fingering instability of a suspension film spreading on a spinning disk". In: *Physics of Fluids* 28 (6 June 2016), pp. 1–8. DOI: 10.1063/1.4953174.

[43] Akhileshwar Singh, Yogesh Singh, and Krishna Murari Pandey. "Viscous fingering instabilities in radial Hele-Shaw cell: A review". In: *Materials Today: Proceedings* 26 (2020). 10th International Conference of Materials Processing and Characterization, pp. 760–762. DOI: https://doi.org/10.1016/j.matpr.2020.01.022.

[44] Diederick Johannes Korteweg. "Sur la forme que prennent les equations du mouvement des fluids si l'on tient compte des forces capillaires causees par des variations de densite". In: *Archives Neerlandaises des Sciences exactes et naturelles* 6 (1901), pp. 1–24.

[45] Joseph John Thomson, Hugh Frank, and Newall. "V. On the formation of vortex rings by drops falling into liquids, and some allied phenomena". In: *Proceedings of the royal society of London* 39 (1886), pp. 416–436. DOI: 10.1098/rspl.1885.0034.

[46] H Freundlich and HS Hatfield. "Colloid and capillary chemistry, Methuen and Co". In: *Ltd., London* (1926), pp. 110–114. DOI: 10.1126/science.65.1672.40..

[47] Anatoliy Vorobev. "Dissolution dynamics of miscible liquid/liquid interfaces". In: *Current Opinion in Colloid and Interface Science* 19 (4 Aug. 2014), pp. 300–308. ISSN: 18790399. DOI: 10.1016/j.cocis.2014.02.004.

[48] LD Landau and EM Lifshitz. "Fluid Mechanics. Pergamon Press, Oxford". In: *Section 92, problem* 2 (1959).

[49] Signe Kjelstrup and Dick Bedeaux. *Non-Equilibrium Thermodynamics of Heterogeneous Systems*. World Scientific, 2008. DOI: 10.1142/9789811216770_0001.

[50] Ya B Zeldovich. "About surface tension of a boundary between two mutually soluble liquids". In: *Zhur. Fiz. Khim* 23 (1949), pp. 931–935.

[51] I Roušar and EB Nauman. "A continuum analysis of surface tension in nonequilibrium systems". In: *Chemical Engineering Communications* 129.1 (1994), pp. 19–28. DOI: 10.1080/00986449408936247.

[52] P.G. Smith, T. G. Ven de Ven, and S.G. Mason. "The Transient Interfacial Tension between Two Miscible Fluids". In: *Journal of Colloid and Interface Science* 80 (1 1981). DOI: 10.1016/0021-9797(81)90186-7.

[53] N Bessonov, John A Pojman, and Vitaly Volpert. "Modelling of diffuse interfaces with temperature gradients". In: *Journal of Engineering Mathematics* 49 (2004), pp. 321–338. DOI: 10.1023/B:ENGI.0000032668.19038.4d.

[54] Ilya Kostin et al. "Modelling of miscible liquids with the Korteweg stress". In: *Mathematical Modelling and Numerical Analysis* 37 (5 Sept. 2003), pp. 741–753. ISSN: 0764583X. DOI: 10.1051/m2an:2003042.

[55] Wen-Jong Ma et al. "Dynamical relaxation of the surface tension of miscible phases". In: *Physical Review Letters* 71 (21 1993), p. 3465. DOI: 10.1103/PhysRevLett.71.3465.

[56] John A. Pojman et al. "Numerical simulations of convection induced by Korteweg stresses in a miscible polymer-monomer system: Effects of variable transport coefficients, polymerization rate and volume changes". In: *Microgravity Science and Technology* 21 (3 July 2009), pp. 225–237. ISSN: 09380108. DOI: 10.1007/s12217-008-9071-y.

[57] G Quincke. "III. Die oberflächenspannung an der grenze von alkohol mit wässerigen salzlösungen. Bildung von zellen, sphärokrystallen und krystallen". In: *Annalen der Physik* 314.9 (1902), pp. 1–43.

[58] Brian Zoltowski et al. "Evidence for the existence of an effective interfacial tension between miscible fluids. 2. Dodecyl acrylate-poly(dodecyl acrylate) in a spinning drop tensiometer". In: *Langmuir* 23 (10 May 2007), pp. 5522–5531. ISSN: 07437463. DOI: 10.1021/la063382g.

[59] Alessandro Carbonaro, Luca Cipelletti, and Domenico Truzzolillo. "Spinning Drop Dynamics in Miscible and Immiscible Environments". In: *Langmuir* 35 (35 Sept. 2019), pp. 11330–11339. ISSN: 15205827. DOI: 10.1021/acs.langmuir.9b02091.

[60] Alessandro Carbonaro, Luca Cipelletti, and Domenico Truzzolillo. "Ultralow effective interfacial tension between miscible molecular fluids". In: *Physical Review Fluids* 5 (7 July 2020). ISSN: 2469990X. DOI: 10.1103/PhysRevFluids.5.074001.

[61] John A. Pojman et al. "Evidence for the existence of an effective interfacial tension between miscible fluids: Isobutyric acid - Water and 1-butanol- water in a spinning-drop tensiometer". In: *Langmuir* 22 (6 Mar. 2006), pp. 2569–2577. ISSN: 07437463. DOI: 10.1021/la052111n.

[62] Ching Yao Chen and Eckart Meiburg. "Miscible displacements in capillary tubes. Part 2. Numerical simulations". In: *Journal of Fluid Mechanics* 326 (Nov. 1996), pp. 57–90. ISSN: 00221120. DOI: 10.1017/S0022112096008245.

[63] Bernard Vonnegut. "Rotating bubble method for the determination of surface and interfacial tensions". In: *Review of Scientific Instruments* 13 (1 1942), pp. 6–9. ISSN: 00346748. DOI: 10.1063/1.1769937.

[64] Laurent Lacaze et al. "Transient surface tension in miscible liquids". In: *Physical Review E - Statistical, Nonlinear, and Soft Matter Physics* 82 (4 Oct. 2010). ISSN: 15502376. DOI: 10.1103/PhysRevE.82.041606.

[65] S E May and J V Maher. "Capillary-Wave Relaxation for a Meniscus between Miscible Liquids". In: *Physical Review Letters* 67 (15 1991). DOI: 10.1103/PhysRevLett.67.2013.

[66] D H Vlad and J V Maher. "Dissolving interfaces in the presence of gravity". In: *Physical Review E* 59 (1 1999), p. 476. DOI: 10.1103/PhysRevE.59.476.

[67] Pietro Cicuta, Alberto Vailati, and Marzio Giglio. "Equilibrium and nonequilibrium fluctuations at the interface between two fluid phases". In: *Physical Review E* 62 (4 2000), p. 4920. DOI: 10.1103/PhysRevE.62.4920.

[68] Pietro Cicuta, Alberto Vailati, and Marzio Giglio. "Capillary-to-bulk crossover of nonequilibrium fluctuations in the free diffusion of a near-critical binary liquid mixture". In: *Applied Optics* 40 (24 2001), pp. 4140–4145. DOI: 10.1364/AO.40.004140.

[69] D. Chatenay, D. Langevin, and J. Meunier. "Measurement of Low Interfacial Tension. Comparison Between a Light Scattering Technique and the Spinning Drop Technique". In: *Journal of Dispersion Science and Technology* 3 (3 Jan. 1982), pp. 245–260. ISSN: 15322351. DOI: 10.1080/01932698208943640.

[70] H. M. Princen, I. Y. Z. Zia, and S. G. Mason. "Measurement of interfacial tension from the shape of a rotating drop". In: *Journal of Colloid and Interface Science* 23 (1 1967), pp. 99–107. DOI: 10.1016/0021-9797(67)90090-2.

[71] Daniel Antrim et al. "Measuring the mutual diffusion coefficient for dodecyl acrylate in low molecular weight poly(dodecyl acrylate) with laser line deflection (Wiener's method) and the fluorescence of pyrene". In: *Journal of Physical Chemistry B* 109 (23 June 2005), pp. 11842–11849. ISSN: 15206106. DOI: 10.1021/jp0502609.

[72] P Petitjeans. *A surface tension for miscible fluids*. May 1996.

[73] Gloria Viner and John A. Pojman. "Studying diffusion of partially miscible and systems near their consolute point by laser line deflection". In: *Optics and Lasers in Engineering* 46 (12 Dec. 2008), pp. 893–899. ISSN: 01438166. DOI: 10.1016/j.optlaseng.2008.04.002.

[74] Philippe Petitjeans. "Une tension de surface pour les fluides miscibles". In: *Comptes rendus de l'Académie des sciences. Série II, Mécanique, physique, chimie, astronomie* 322.9 (1996), pp. 673–679.

[75] N Rashidnia et al. "Measurement of the Diffusion Coefficient of Miscible Fluids Using Both Interferometry and Wiener's Method". In: *International Journal of Thermophysics* 22 (2 2001), pp. 547–555. DOI: 10.1023/A:1010735117408.

[76] R. Borcia et al. "Delayed coalescence of droplets with miscible liquids: Lubrication and phase field theories". In: *European Physical Journal E* 34 (3 Mar. 2011). ISSN: 12928941. DOI: 10.1140/epje/i2011-11024-9.

[77] Stefan Karpitschka and Hans Riegler. "Quantitative experimental study on the transition between fast and delayed coalescence of sessile droplets with different but completely miscible liquids". In: *Langmuir* 26 (14 July 2010), pp. 11823–11829. ISSN: 07437463. DOI: 10.1021/la1007457.

[78] Stefan Karpitschka and Hans Riegler. "Noncoalescence of sessile drops from different but miscible liquids: Hydrodynamic analysis of the twin drop contour as a self-stabilizing traveling wave". In: *Physical Review Letters* 109 (6 Aug. 2012). ISSN: 00319007. DOI: 10.1103/PhysRevLett.109.066103.

[79] Hans Riegler and Paul Lazar. "Delayed coalescence behavior of droplets with completely miscible liquids". In: *Langmuir* 24 (13 July 2008), pp. 6395–6398. ISSN: 07437463. DOI: 10.1021/la800630w.

[80] Masami Kojima, E. J. Hinch, and Andreas Acrivos. "The formation and expansion of a toroidal drop moving in a viscous fluid". In: *Physics of Fluids* 27 (1 1984), pp. 19–32. ISSN: 10706631. DOI: 10.1063/1.864511.

[81] F T Arecchi et al. "An Experimental Investigation of the Break-up of a Liquid Drop Falling in a Miscible Fluid". In: *EUROPHYSics Letters* 9 (4 1989), pp. 333–338. DOI: 10.1209/0295-5075/9/4/006.

[82] F T Arecchi et al. "Fragmentation of a drop as it falls in a lighter miscible fluid". In: *Physical Review E* 54 (1 1996), p. 242. DOI: 10.1103/PhysRevE.54.424.

[83] P. Petitjeans and T. Maxworthy. "Miscible displacements in capillary tubes. Part 1. Experiments". In: *Journal of Fluid Mechanics* 326 (Nov. 1996), pp. 37–56. ISSN: 00221120. DOI: 10.1017/S0022112096008233.

[84] M. S.P. Stevar and A. Vorobev. "Shapes and dynamics of miscible liquid/liquid interfaces in horizontal capillary tubes". In: *Journal of Colloid and Interface Science* 383 (1 Oct. 2012), pp. 184–197. ISSN: 00219797. DOI: 10.1016/j.jcis.2012.06.053.

[85] Jun Kuang, Tony Maxworthy, and Philippe Petitjeans. "Miscible displacements between silicone oils in capillary tubes". In: *European Journal of Mechanics, B/Fluids* 22 (3 May 2003), pp. 271–277. ISSN: 09977546. DOI: 10.1016/S0997-7546(03)00035-9.

[86] J. Kuang, P. Petitjeans, and T. Maxworthy. "Velocity fields and streamline patterns of miscible displacements in cylindrical tubes". In: *Experiments in Fluids* 37 (2 2004), pp. 301–308. ISSN: 07234864. DOI: 10.1007/s00348-004-0824-0.

[87] R. Balasubramaniam et al. "Instability of miscible interfaces in a cylindrical tube". In: *Physics of Fluids* 17 (5 2005), pp. 1–11. ISSN: 10706631. DOI: 10.1063/1.1884645.

[88] Ching Yao Chen and Eckart Meiburg. "Miscible displacements in capillary tubes: Influence of Korteweg stresses and divergence effects". In: *Physics of Fluids* 14 (7 2002), pp. 2052–2058. ISSN: 10706631. DOI: 10.1063/1.1481507.

[89] S. H. Vanaparthy and E. Meiburg. "Variable density and viscosity, miscible displacements in capillary tubes". In: *European Journal of Mechanics, B/Fluids* 27 (3 May 2008), pp. 268–289. ISSN: 09977546. DOI: 10.1016/j.euromechflu.2007.06.003.

[90] M. d'Olce et al. "Pearl and mushroom instability patterns in two miscible fluids' core annular flows". In: *Physics of Fluids* 20 (2 2008). ISSN: 10706631. DOI: 10.1063/1.2838582.

[91] M. D'Olce et al. "Convective/absolute instability in miscible core-annular flow. Part 1: Experiments". In: *Journal of Fluid Mechanics* 618 (2009), pp. 305–322. ISSN: 14697645. DOI: 10.1017/S0022112008004230.

[92] Lincoln Paterson. "Fingering with miscible fluids in a Hele Shaw cell". In: *Physics of Fluids* 28 (1 1985), pp. 26–30. ISSN: 10706631. DOI: 10.1063/1.865195.

[93] Irmgard Bischofberger, Radha Ramachandran, and Sidney R. Nagel. "Fingering versus stability in the limit of zero interfacial tension". In: *Nature Communications* 5 (2014). ISSN: 20411723. DOI: 10.1038/ncomms6265.

[94] Eric Lajeunesse et al. "3D Instability of Miscible Displacements in a Hele-Shaw Cell". In: *Physical Review Letters* 79 (26 1997), p. 5254. DOI: 10.1103/PhysRevLett.79.5254.

[95] J.-D Chen. "Radial viscous fingering patterns in Hele-Shaw cells". In: *Experiments in Fluids* 5 (6 1987), pp. 363–371. DOI: 10.1007/BF00264399.

[96] Chen Hua Chen and Ching Yao Chen. "Fingering patterns on an expanding miscible drop in a rotating Hele-Shaw cell". In: *International Journal for Numerical Methods in Fluids* 54 (10 Aug. 2007), pp. 1201–1214. ISSN: 02712091. DOI: 10.1002/fld.1426.

[97] Wen Song, Natarajan N. Ramesh, and Anthony R. Kovscek. "Spontaneous fingering between miscible fluids". In: *Colloids and Surfaces A: Physicochemical and Engineering Aspects* 584 (Jan. 2020). ISSN: 18734359. DOI: 10.1016/j.colsurfa.2019.123943.

[98] Thomas K. Perkins, Orville Johnston, and robert N. Hoffman. "Mechanics of Viscous Fingering in Miscible Systems". In: *Society of Petroleum Engineers Journal* 5 (4 1965), pp. 301–317. DOI: 10.2118/1229-PA.

[99] P Garik et al. "Interfacial Cellular Mixing and a Conjecture on Global Deposit Morphology". In: *Physical Review Letters* 66 (12 1991). DOI: 10.1103/PhysRevLett.66.1606.

[100] S M Troian, X l Wu, and S A Safran. "Fingering Instability in thin wetting films". In: *Physical Review Letters* 62 (13 1989), pp. 1496–1500. DOI: 10.1103/PhysRevLett.62.1496.

[101] Yuri Gaponenko et al. "Interfacial pattern selection in miscible liquids under vibration". In: *Soft Matter* 11.42 (2015), pp. 8221–8224. DOI: 10.1039/C5SM02110C.

[102] Marc Legendre, Philippe Petitjeans, and Pascal Kurowski. "Instabilités à l'interface entre fluides miscibles par forçage oscillant horizontal". In: *Comptes Rendus - Mecanique* 331 (9 2003), pp. 617–622. ISSN: 16310721. DOI: 10.1016/S1631-0721(03)00127-X.

[103] Domenico Truzzolillo et al. "Nonequilibrium interfacial tension in simple and complex fluids". In: *Physical Review X* 6 (4 2016). ISSN: 21603308. DOI: 10.1103/PhysRevX.6.041057.

[104] Daniel J. Walls et al. "Spreading of miscible liquids". In: *Physical Review Fluids* 1 (1 May 2016). ISSN: 2469990X. DOI: 10.1103/PhysRevFluids.1.013904.

[105] Daniel J. Walls, Eckart Meiburg, and Gerald G. Fuller. "The shape evolution of liquid droplets in miscible environments". In: *Journal of Fluid Mechanics* 852 (Oct. 2018), pp. 422–452. ISSN: 14697645. DOI: 10.1017/jfm.2018.535.

[106] N. Didden and T. Maxworthy. "The viscous spreading of plane and axisymmetric gravity currents". In: *Journal of Fluid Mechanics* 121 (1982), pp. 27–42. ISSN: 14697645. DOI: 10.1017/S0022112082001785.

[107] Herbert E. Huppert. "The propagation of two-dimensional and axisymmetric viscous gravity currents over a rigid horizontal surface". In: *Journal of Fluid Mechanics* 121 (1982), pp. 43–58. ISSN: 14697645. DOI: 10.1017/S0022112082001797.

[108] G. I. Taylor. "Deposition of a viscous fluid on the wall of a tube". In: *Journal of Fluid Mechanics* 10 (2 1961), pp. 161–165. ISSN: 14697645. DOI: 10.1017/S0022112061000159.

[109] J E Mungall. "Interfacial Tension in Miscible Two-Fluid Systems with Linear Viscoelastic Rheology". In: *Physical Review Letters* 73 (2 1994), p. 288. DOI: 10.1103/PhysRevLett.73.288.

[110] Daniel Joseph and Renardy Yuriko. *Fundamentals of Two-Fluid Dynamics. Part II: Lubricated Trasport, Drops and Miscible Fluids*. Springer, 1993, pp. 324–395. DOI: 10.1007/978-1-4615-7061-5_6.

[111] Domenico Truzzolillo and Luca Cipelletti. *Hydrodynamic instabilities in miscible fluids*. Jan. 2018. DOI: 10.1088/1361-648X/aa9eaa.

[112] Philip Geoffrey Saffman and Geoffrey Ingram Taylor. "The penetration of a fluid into a porous medium or Hele-Shaw cell containing a more viscous liquid". In: *Proceedings of the Royal Society of London. Series A. Mathematical and Physical Sciences* 245.1242 (1958), pp. 312–329. DOI: 10.1098/rspa.1958.0085.

[113] Domenico Truzzolillo et al. "Off-equilibrium surface tension in colloidal suspensions". In: *Physical Review Letters* 112 (12 Dec. 2013). ISSN: 10797114. DOI: 10.1103/PhysRevLett.112.128303.

[114] A. Castellanos and A. González. "Interfacial electrohydrodynamic instability: The Kath and Hoburg model revisited". In: *Physics of Fluids A* 4 (6 1992), pp. 1307–1309. ISSN: 08998213. DOI: 10.1063/1.858249.

[115] Rogerio Manica, Evert Klaseboer, and Derek Y.C. Chan. "The hydrodynamics of bubble rise and impact with solid surfaces". In: *Advances in Colloid and Interface Science* 235 (Sept. 2016), pp. 214–232. ISSN: 00018686. DOI: 10.1016/j.cis.2016.06.010.

[116] Dotchi Exerowa and Pyotr M Kruglyakov. *Foam and foam films: theory, experiment, application*. Elsevier, 1997.

[117] Rogerio Manica et al. "Interpreting the dynamic interaction between a very small rising bubble and a hydrophilic titania surface". In: *The Journal of Physical Chemistry C* 114.4 (2010), pp. 1942–1946. DOI: 10.1021/jp911104b.

[118] Maurice H.W. Hendrix et al. "Spatiotemporal evolution of thin liquid films during impact of water bubbles on glass on a micrometer to nanometer scale". In: *Physical Review Letters* 108 (24 June 2012). ISSN: 00319007. DOI: 10.1103/PhysRevLett.108.247803.

[119] Jan Zawala and Kazimierz Malysa. "Influence of the impact velocity and size of the film formed on bubble coalescence time at water surface". In: *Langmuir* 27 (6 Mar. 2011), pp. 2250–2257. ISSN: 07437463. DOI: 10.1021/la104324u.

[120] D Kosior et al. "Influence of non-ionic and ionic surfactants on kinetics of the bubble attachment to hydrophilic and hydrophobic solids". In: *Colloids and Surfaces A: Physicochemical and Engineering Aspects* 470 (2015), pp. 333–341. DOI: 10.1016/j.colsurfa.2014.11.043.

[121] D Kosior, J Zawala, and K Malysa. "Influence of n-octanol on the bubble impact velocity, bouncing and the three phase contact formation at hydrophobic solid surfaces". In: *Colloids and Surfaces A: Physicochemical and Engineering Aspects* 441 (2014), pp. 788–795. DOI: 10.1016/j.colsurfa.2012.10.025.

[122] Marta Krasowska and K Malysa. "Kinetics of bubble collision and attachment to hydrophobic solids: I. Effect of surface roughness". In: *International Journal of Mineral Processing* 81.4 (2007), pp. 205–216. DOI: 10.1016/j.minpro.2006.05.003.

[123] K. Malysa, M. Krasowska, and M. Krzan. "Influence of surface active substances on bubble motion and collision with various interfaces". In: *Advances in Colloid and Interface Science* 114-115 (June 2005), pp. 205–225. ISSN: 00018686. DOI: 10.1016/j.cis.2004.08.004.

[124] Liguang Wang and Xuan Qu. "Impact of interface approach velocity on bubble coalescence". In: *Minerals Engineering* 26 (2012), pp. 50–56. DOI: 10.1016/j.mineng.2011.10.016.

[125] Toshiyuki Sanada, Masao Watanabe, and Tohru Fukano. "Effects of viscosity on coalescence of a bubble upon impact with a free surface". In: *Chemical Engineering Science* 60 (19 Sept. 2005), pp. 5372–5384. ISSN: 00092509. DOI: 10.1016/j.ces.2005.04.077.

[126] T T Traykov and I B Ivanov. "Hydrodynamics of thin liquid films. Effect of surfactants on the velocity of thinning of emulsion films". In: *International Journal of Multiphase Flow* 3 (5 1977), pp. 471–483. DOI: 10.1016/0301-9322(77)90023-4.

[127] Stoyan I. Karakashev and Emil D. Manev. "Hydrodynamics of thin liquid films: Retrospective and perspectives". In: *Advances in Colloid and Interface Science* 222 (Aug. 2015), pp. 398–412. ISSN: 00018686. DOI: 10.1016/j.cis.2014.07.010.

[128] J. Zawala et al. "Influence of bubble kinetic energy on its bouncing during collisions with various interfaces". In: *Canadian Journal of Chemical Engineering* 85 (5 2007), pp. 669–678. ISSN: 00084034. DOI: 10.1002/cjce.5450850514.

[129] O Reynolds. "On the theory of lubrication and its application to Mr. Beauchamp Tower's experiments, including an experimental determination of the viscosity of olive oil". In: *Phil. Trans. Roy. Soc.* 1 (1885), p. 157.

[130] SS Sadhal and Robert E Johnson. "Stokes flow past bubbles and drops partially coated with thin films. Part 1. Stagnant cap of surfactant film–exact solution". In: *Journal of Fluid Mechanics* 126 (1983), pp. 237–250. DOI: 10.1017/S0022112083000130.

[131] Rogerio Manica, Evert Klaseboer, and Derek YC Chan. "Force balance model for bubble rise, impact, and bounce from solid surfaces". In: *Langmuir* 31.24 (2015), pp. 6763–6772. DOI: 10.1021/acs.langmuir.5b01451.

[132] Evert Klaseboer et al. "A force balance model for the motion, impact, and bounce of bubbles". In: *Physics of Fluids* 26.9 (2014). DOI: 10.1063/1.4894067.

[133] Rogerio Manica et al. "Effects of hydrodynamic film boundary conditions on bubble–wall impact". In: *Soft Matter* 9.41 (2013), pp. 9755–9758. DOI: 10.1039/C3SM51769A.

[134] Suat Canberk Ozan and Hugo Atle Jakobsen. "Effect of surface viscoelasticity on the film drainage and the interfacial mobility". In: *International Journal of Multiphase Flow* 130 (Sept. 2020). ISSN: 03019322. DOI: 10.1016/j.ijmultiphaseflow.2020.103377.

[135] Xurui Zhang et al. "Effect of Approach Velocity on Thin Liquid Film Drainage between an Air Bubble and a Flat Solid Surface". In: *Journal of Physical Chemistry C* 121 (10 Mar. 2017), pp. 5573–5584. ISSN: 19327455. DOI: 10.1021/acs.jpcc.6b11502.

[136] Rogerio Manica and Derek Y.C. Chan. "Drainage of the air-water-quartz film: Experiments and theory". In: *Physical Chemistry Chemical Physics* 13 (4 Jan. 2011), pp. 1434–1439. ISSN: 14639076. DOI: 10.1039/c0cp00677g.

[137] K. Giribabu, M. L.N. Reddy, and P. Ghosh. "Coalescence of air bubbles in surfactant solutions: Role of salts containing mono-, di-, and trivalent ions". In: *Chemical Engineering Communications* 195 (3 Mar. 2008), pp. 336–351. ISSN: 00986445. DOI: 10.1080/00986440701555316.

[138] Klaus Werner Stöckelhuber et al. "Rupture of Wetting Films Caused by Nanobubbles". In: *Langmuir* 20 (1 Jan. 2004), pp. 164–168. ISSN: 07437463. DOI: 10.1021/la0354887.

[139] Xin Cui et al. "Probing Interactions between Air Bubble and Hydrophobic Polymer Surface: Impact of Solution Salinity and Interfacial Nanobubbles". In: *Langmuir* 32 (43 Nov. 2016), pp. 11236–11244. ISSN: 15205827. DOI: 10.1021/acs.langmuir.6b01674.

[140] Derek Y.C. Chan, Evert Klaseboer, and Rogerio Manica. "Film drainage and coalescence between deformable drops and bubbles". In: *Soft Matter* 7 (6 Mar. 2011), pp. 2235–2264. ISSN: 1744683X. DOI: 10.1039/c0sm00812e.

[141] Travis S. Emery and Satish G. Kandlikar. "Film size during bubble collision with a solid surface". In: *Journal of Fluids Engineering, Transactions of the ASME* 141 (7 July 2019). ISSN: 1528901X. DOI: 10.1115/1.4041990.

[142] Leonard R Fisher et al. “The drainage of a thin aqueous film between a solid surface and an approaching gas bubble”. In: *Colloids and Surface* 52 (1991), pp. 163–174. DOI: 10.1016/0166-6622(91)80011-C.

[143] L r Fisher et al. “The Drainage of an Aqueous Film between a Solid Plan and an Air Bubble”. In: *Advances in Colloid and Interface Science* 39 (1992), pp. 397–416. DOI: 10.1016/0001-8686(92)80067-8.

[144] D Hewitt et al. “Aqueous Film Drainage at the Quartz/Water/Air Interface”. In: *Journal of the Chemical Society* 89 (5 1993), pp. 817–822. DOI: 10.1039/FT9938900817.

[145] Bernard P Binks. “Particles as surfactants—similarities and differences”. In: *Current opinion in colloid & interface science* 7.1-2 (2002), pp. 21–41. DOI: 10.1016/S1359-0294(02)00008-0.

[146] Robert Aveyard et al. “Compression and structure of monolayers of charged latex particles at air/water and octane/water interfaces”. In: *Langmuir* 16 (4 Feb. 2000), pp. 1969–1979. ISSN: 07437463. DOI: 10.1021/la990887g.

[147] C. Monteux, E. Jung, and G. G. Fuller. “Mechanical properties and structure of particle coated interfaces: Influence of particle size and bidisperse 2D suspensions”. In: *Langmuir* 23 (7 Mar. 2007), pp. 3975–3980. ISSN: 07437463. DOI: 10.1021/la063380w.

[148] L. J. Bonales et al. “Freezing transition and interaction potential in monolayers of microparticles at fluid interfaces”. In: *Langmuir* 27 (7 Apr. 2011), pp. 3391–3400. ISSN: 07437463. DOI: 10.1021/la104917e.

[149] Laure Bluteau et al. “Water film squeezed between oil and solid: drainage towards stabilization by disjoining pressure”. In: *Soft Matter* 13 (7 2017), pp. 1384–1395. ISSN: 17446848. DOI: 10.1039/c6sm02423h.

[150] Giovanni Cocchi, Maria Grazia De Angelis, and Ferruccio Doghieri. “Solubility and diffusivity of liquids for food and pharmaceutical applications in crosslinked polydimethylsiloxane (PDMS) films: I. Experimental data on pure organic components and vegetable oil”. In: *Journal of Membrane Science* 492 (2015), pp. 600–611. DOI: 10.1016/j.memsci.2015.04.063.

[151] Joseph D. Berry et al. *Measurement of surface and interfacial tension using pendant drop tensiometry*. Sept. 2015. DOI: 10.1016/j.jcis.2015.05.012.

[152] Katsuichi Kitagawa. “Thin-film thickness profile measurement by three-wavelength interference color analysis”. In: *Appl. Opt.* 52.10 (Apr. 2013), pp. 1998–2007. DOI: 10.1364/AO.52.001998.

[153] John M Frostad et al. “Dynamic fluid-film interferometry as a predictor of bulk foam properties”. In: *Soft Matter* 12.46 (2016), pp. 9266–9279. DOI: 10.1039/C6SM01361A.

[154] Jason N. Connor and Roger G. Horn. “The influence of surface forces on thin film drainage between a fluid drop and a flat solid”. In: *Faraday Discussions* 123 (1 2003), pp. 193–206. ISSN: 13645498. DOI: 10.1039/b204500c.

[155] Rogério Manica et al. “Transient responses of a wetting film to mechanical and electrical perturbations”. In: *Langmuir* 24 (4 Feb. 2008), pp. 1381–1390. ISSN: 07437463. DOI: 10.1021/la701562q.

[156] S P Frenkel and K J Myseis. “On the "Dimpling" during the approach of two interfaces”. In: *The Journal of Physical Chemistry* 66 (1 1962), pp. 190–191.

[157] Stanley Hartland A b and John D Robinson. “A Model for an Axisymmetric Dimpled Draining Film”. In: *Journal of Colloid and Interface Science* 60 (1 1977), pp. 72–81. DOI: 10.1016/0021-9797(77)90256-9.

[158] A. G. Bykov et al. “Dilational surface elasticity of spread monolayers of polystyrene microparticles”. In: *Soft Matter* 10 (34 Sept. 2014), pp. 6499–6505. ISSN: 17446848. DOI: 10.1039/c4sm00782d.

Author's Publications

Paper

- Tammaro, Daniele, Suja,Vinny Chandran, Kannan, Aadithya, Gala, Luigi Davide, Di Maio, Ernesto, Fuller, Gerald G., and Maffettone, Pier Luca. "Flowering in bursting bubbles with viscoelastic interfaces." *Proceedings of the National Academy of Sciences* 118, 30 (2021). DOI: https://doi.org/10.1073/pnas.2105058118
- Dhara, Palash, Jung, Buyoung, Gala, Luigi Davide, Borkar, Suraj, and Fuller, Gerald G. "Influence of hydrophobic particles on the film drainage during bubble-solid interaction". *Physics of Fluids* 36 (2024). DOI: https://doi.org/10.1063/5.0196809

Conference Paper

- Gala, Luigi Davide (2022, April 26th-28th). *Fingers formation and oscillatory Kelvin-Helmholtz instability in miscible fluids* [Conference Paper]. AERC 2022, Sevilla, Spain.
- Gala, Luigi Davide (2023, May 8th-9th). *Oscillatory Kelvin-Helmholtz instability and fluid fingers formation in miscible systems* [Conference Paper]. EYRS 2023, Online.

Awards

- Gala, Luigi Davide (2020, December 13th-18th). *"Bubble Flowering in retracting viscoelastic thin films"*. Third Place, Gallery of Rheology Photos Contest. ICR 2020, Online.